

Magnet Technology

- How to provide magnetic field with magnets?
 - Water-cooled pulsed magnet
 - Superconducting magnet

- Magnet consideration
 - ✓ Magnetic field strength
 - ✓ Coil cooling → maximum current (density)
 - ✓ Magnetic stress

Coil Cooling for High Magnetic Field

- ✓ Magnetic field strength requires sufficient current
- ✓ Current density: limited by coil cooling and magnet material

➤ Maximum current density in the coil:
copper, water-cooled JET 1.37-2.5kA/cm² for 30 seconds

The thermal power removed by the coolant is

$$P = C \rho_m \Delta T (dV / dt) \quad Re = Dv\rho_m / \mu$$

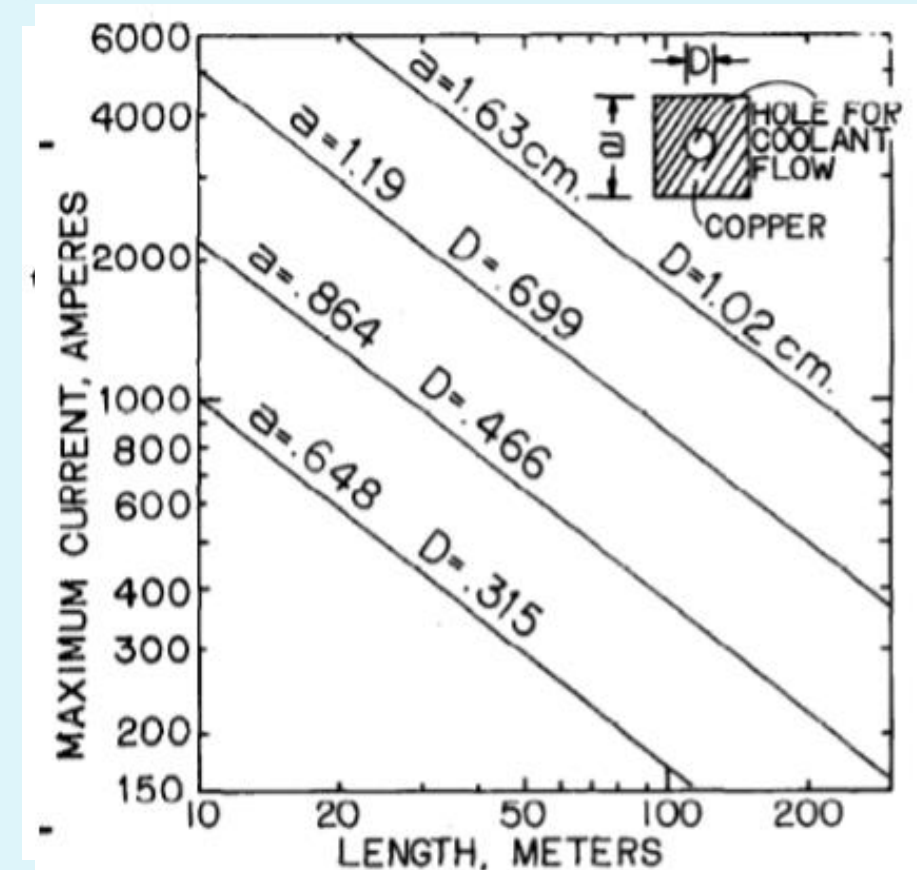
$$(dV / dt)_{channel} = A_w v \quad \Delta p = f L_c C \rho_m v^2 / 2D$$

The pumping power required to produce a pressure rise Δp and flow rate dV/dt is

$$P_c = \Delta p (dV / dt) / \eta_p$$

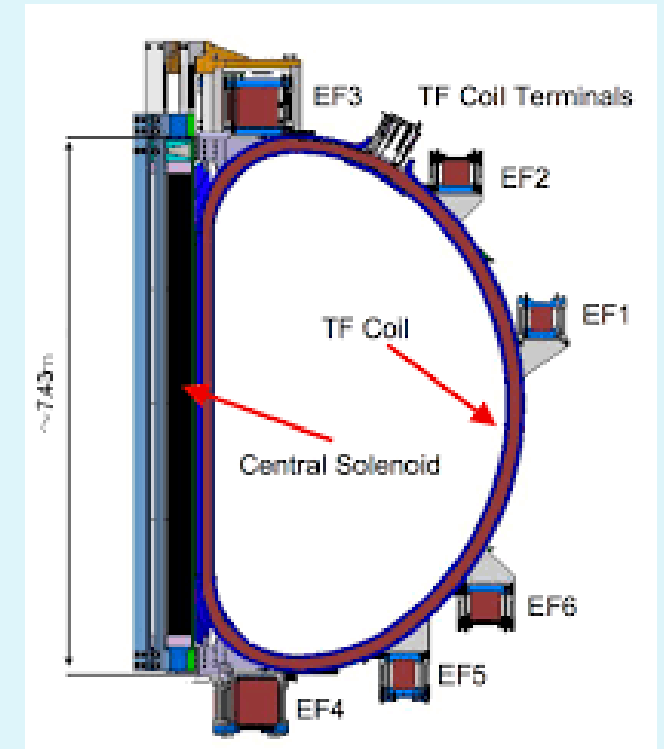
$$C = 4182 \text{ J / kg / K} \quad \rho_m = 998 \text{ kg / m}^3$$

$$\mu = 0.001002 \text{ Pa s} \quad \eta_p \text{ is the pump efficiency, } \sim 0.8$$



Magnetic field strength and stress

- Magnetic field strength requires sufficient current
 - Current density: limited by coil cooling
 - Magnetic stress: limited by yield stress 280 Mpa for copper
- TF coil forces tend to:
 - ✓ increase coil radius a_c
 - ✓ decrease major radius R_c
 - ✓ bend coils (due to interaction with vertical field).
- In design of coils, we need to consider
 - ✓ stress concentrations
 - ✓ fatigue
 - ✓ creep
 - ✓ thermal stress



➤ TF coils shaped like "D"s have lower bending stresses than circular coils.

"Pulsed" Magnet System

- RLC circuit equations

- Pulsed power source: higher currents possible with less cooling
- Fusion requires large-volume pulse magnets with large stored energy

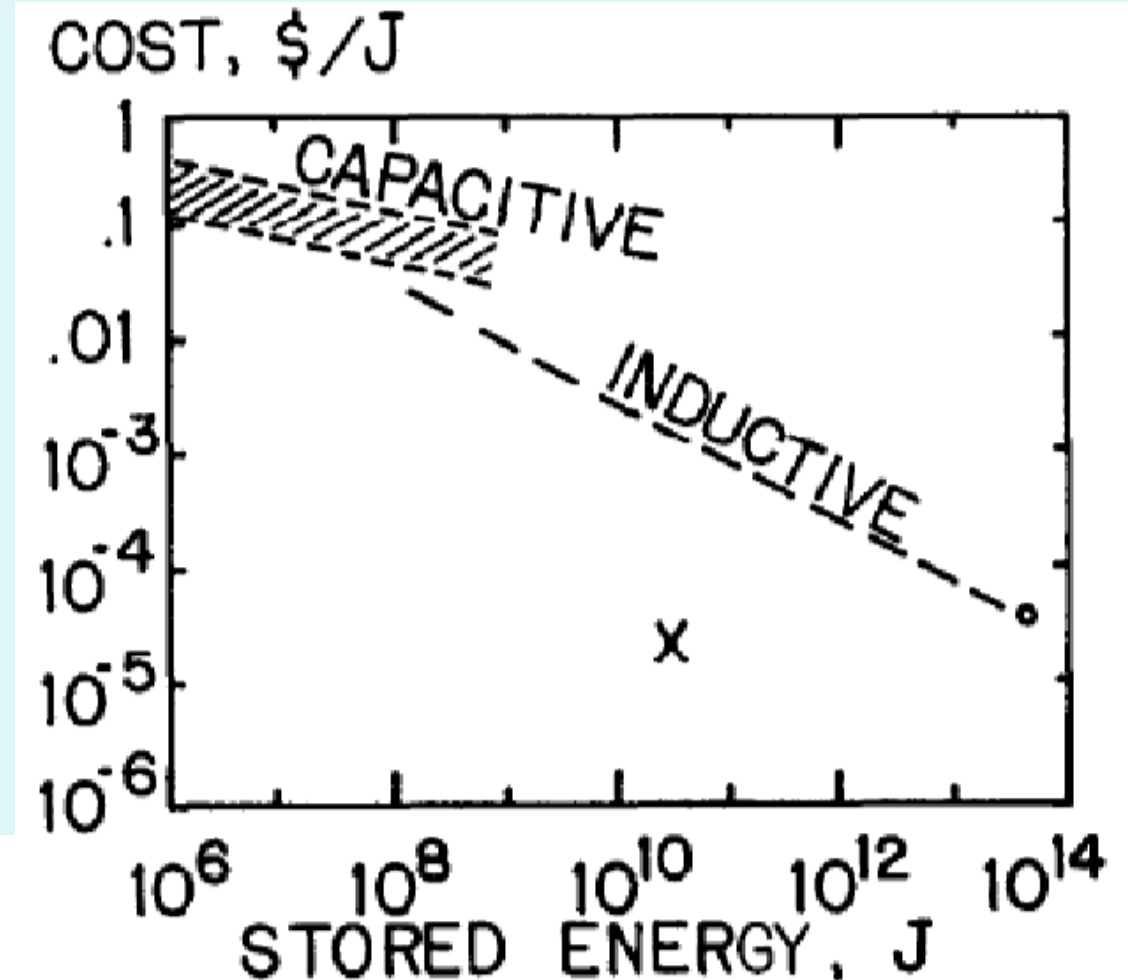
Generate require current waveforms with appropriate circuits.

Resistance: dc and ac → skin current

Inductance: self and mutual → eddy current

Capacitance (energy storage): serial and parallel → voltage and current source

"Pulsed" Magnet System



- Energy storage

- Capacitor vs. inductor
- Capacitor has better efficiency
- Decay time will be different by either RC or L/R

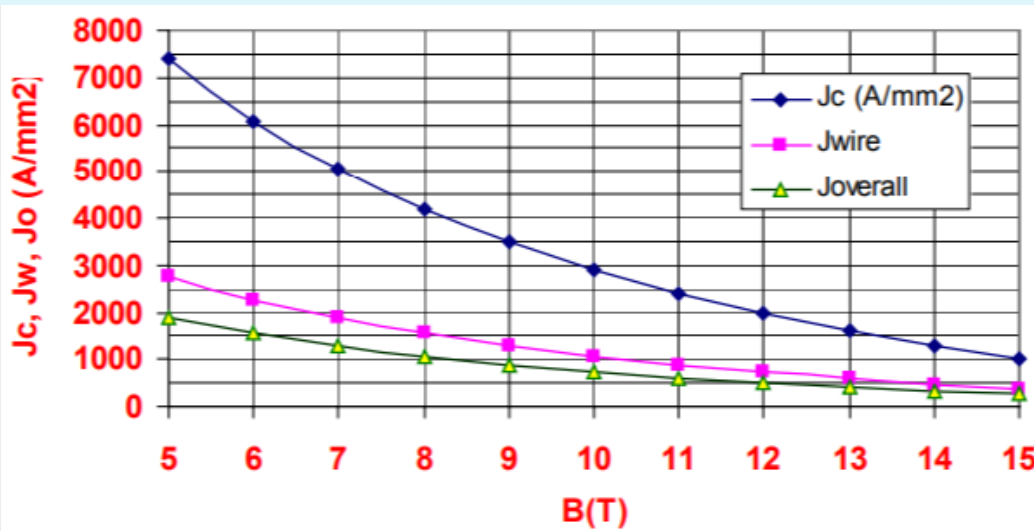
Superconducting Magnet System

➤ Maximum current density of superconducting coils

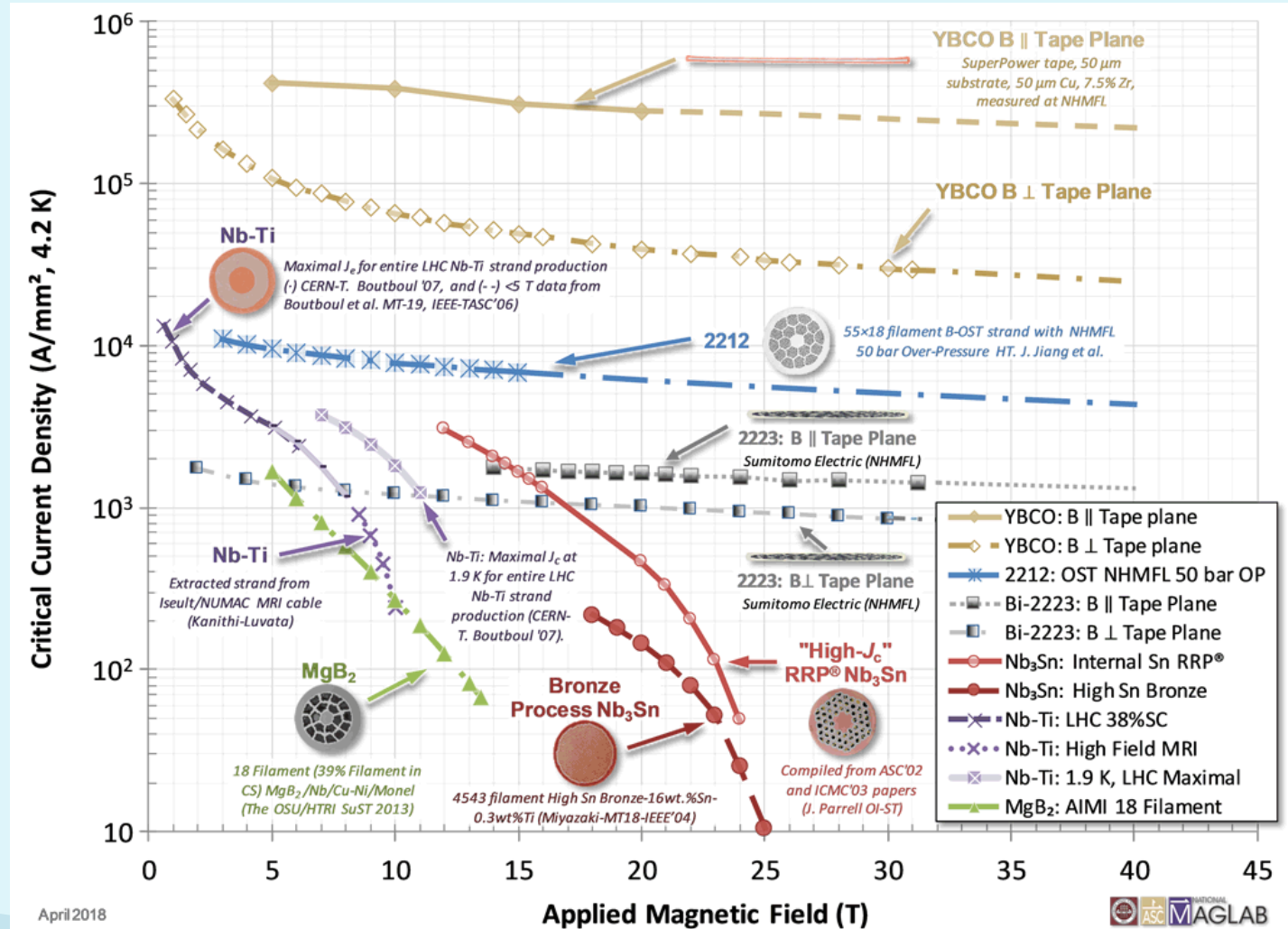
ITER requires 3.7kA/cm^2 with Nb_3Sn superconductor

Nb_3Sn (ITER) : 5kA/cm^2 , $<15\text{T}$

HTS(2212): $>10\text{kA/cm}^2$, $>20\text{T}$

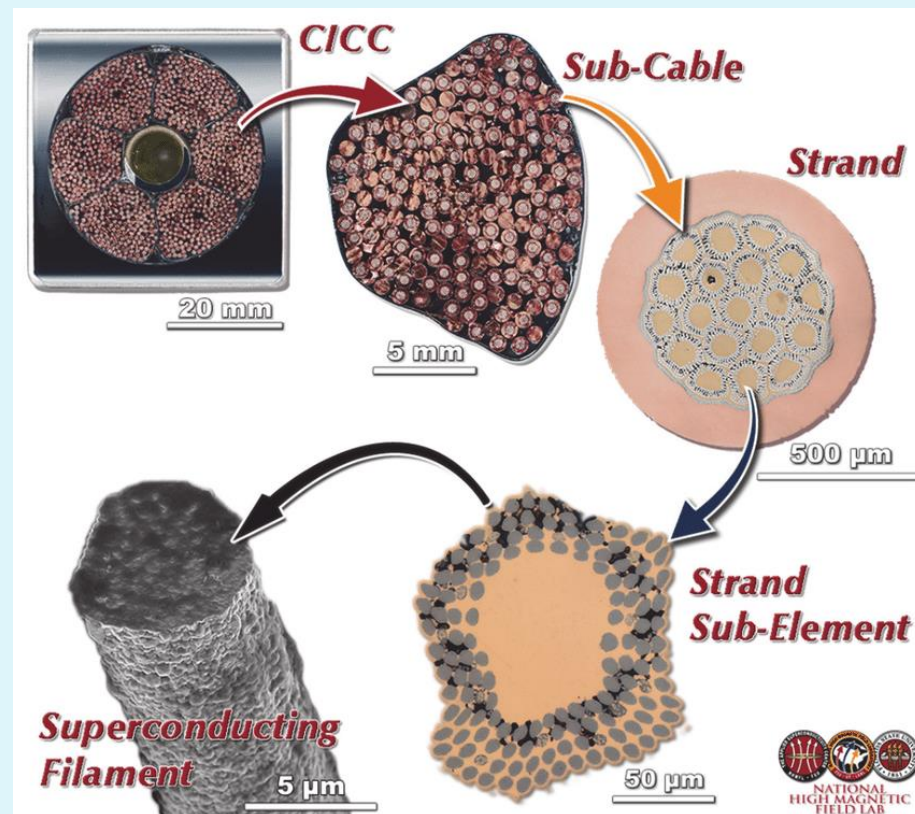
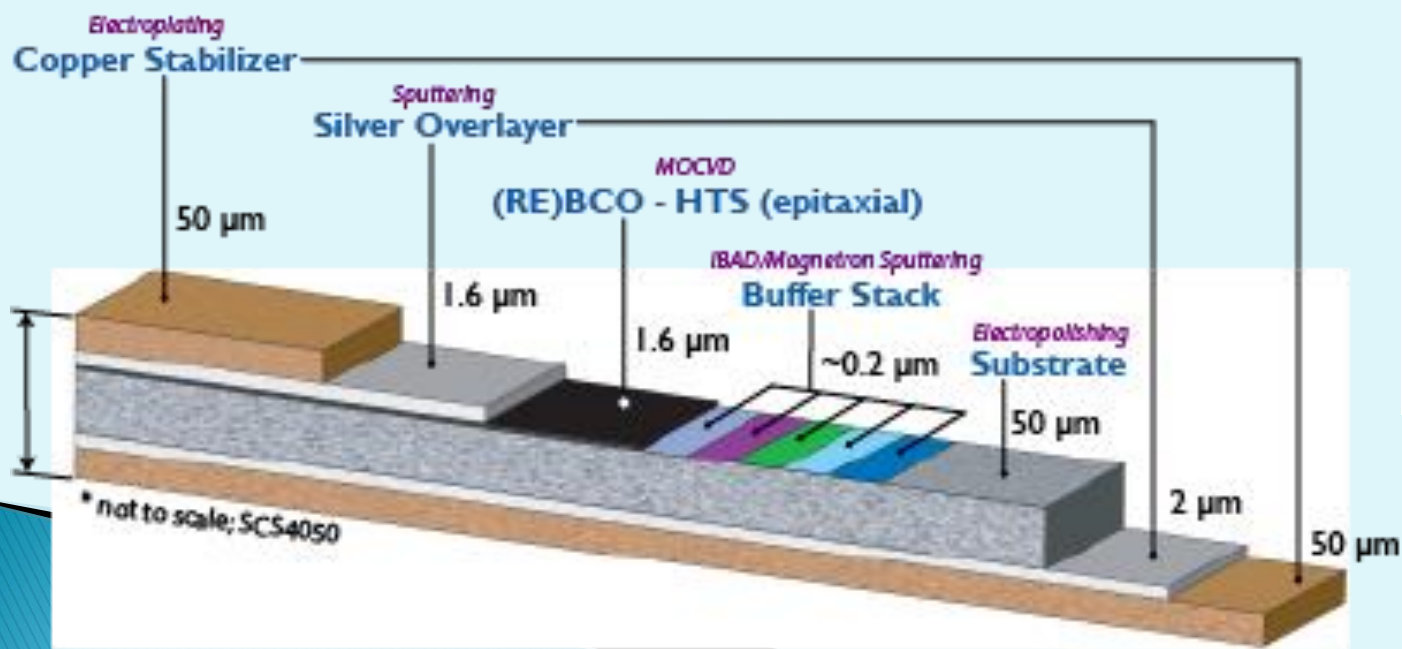


<https://nationalmaglab.org/>



Superconducting Magnet System

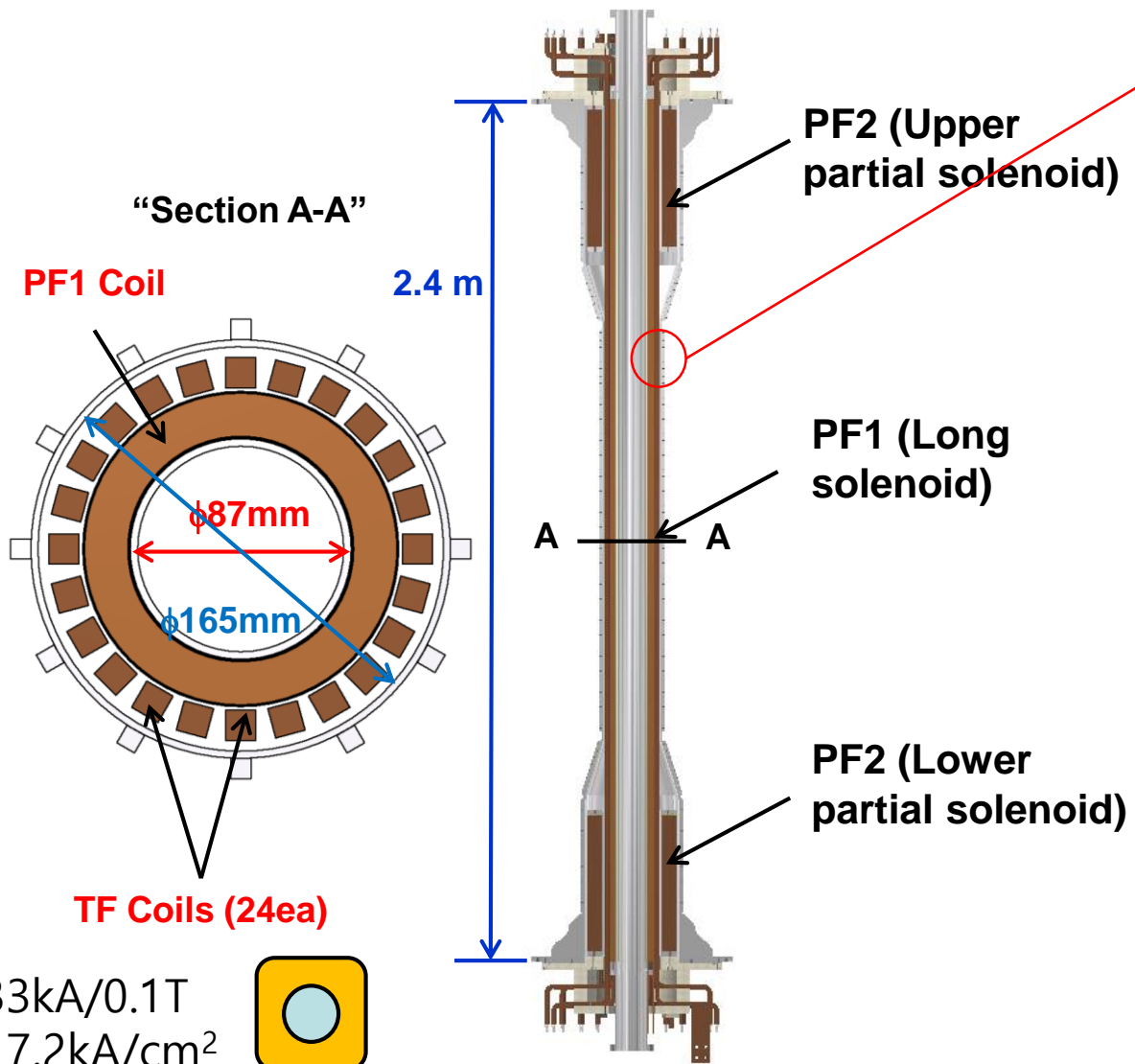
- Superconducting magnet design
 - Cryogenic stabilization
 - Adiabatic stabilization: twisting
 - Dynamic stabilization: Copper stabilization
- CICC
- HTS Tape



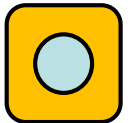
Homework # 2-2

1. Calculate maximum toroidal field achievable with VEST TF and PF coils in view of cooling.
2. Calculate maximum toroidal field achievable with VEST TF and PF coils in view of stress.

Design of VEST TF and PF Magnets



8.33kA/0.1T
 $\rightarrow 7.2\text{kA}/\text{cm}^2$



OFHC Cu
 (12x12, $\phi 6$)

Stress limit:
 Tensile strength of Cu ~ 70 MPa

Parameters	PF1	PF2
Initial Goal	Large plasma of 30 kA	Small plasma of 10 kA
Volt-sec [mV-s]	~ 55	~ 20
Required A-T [MA]	5.2	0.21
R_{in} / R_{out} [m]	0.045 / 0.063	0.08 / 0.125
Coil length [m]	2.8	0.5
Wire size [mm ²]	56.0 (3.5 x 16)	56.0 (3.5 x 16)
N [#]	632 (4 x 158)	250 (10 x 25)
I_{Peak} [kA]	7.3	0.84
Driving Circuit	RLC double swing	RLC double swing
R [m Ω]	68	52 each
L [mH]	1.6	3.7 each
C [mF]	200 / 1 / 500	10 / 0.2 / 50
V_0 [kV]	+1.0 / +1.0 / -2.0	+0.7 / +0.7 / -0.5
Max. achievable V-s [mV-s] @stress limit	130	545
I_{Peak} [kA] @stress limit	27.3	14.0
B_{Peak} [T] @stress limit	7.4	8.0
Max. sustaining time @thermal limit (90°C)	~ 50 ms	~ 180 ms

Chapt. 3* Pulsed and Water-Cooled Magnets

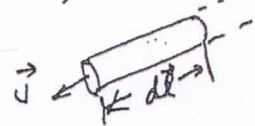
I. Water-Cooled Magnets

Faraday's induction law: $\nabla \times \vec{E} = - \frac{\partial \vec{B}}{\partial t}$ (in MKS unit)

Note: $\vec{B} = \mu \vec{H}$
 magnetic induction \vec{B} , μ permeability, \vec{H} "magnetic field"
 (But \vec{B} is often called as "magnetic field")

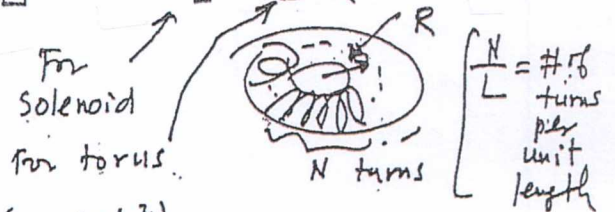
Item	Water-Cooled Magnet	Superconducting magnet
cryogenic insulation & refrigeration	no	yes
Easy disassembly & maintenance	yes	no
Danger from plasma disruption	little	yes
Durability against high neutron fluence	good	vulnerable

1) Thin wire: $\vec{B}(r) = \frac{\mu_0 I}{4\pi} \int_{\text{wire}} \frac{d\vec{l} \times \vec{r}}{r^3}$, ($\vec{r} = \vec{r} - \vec{r}'$) (Tesla)

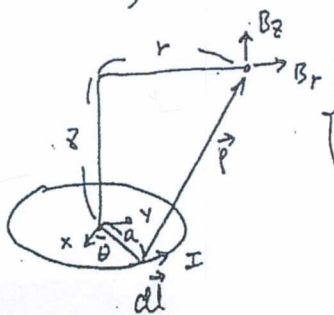


2) Infinitely long wire: $\vec{B}(r) = \frac{\mu_0 I}{2\pi r}$

3) Torus & solenoid: $\vec{B}(R) = \frac{\mu_0 N I}{L}$, $\left\{ \begin{array}{l} N = \# \text{ of turns of wire} \\ L = 2\pi R \end{array} \right.$



4) Circular loops:



$$\left\{ \begin{array}{l} B_r = \frac{\mu_0 I k z}{4\pi \sqrt{a} r^3} \left[-K(k) + \frac{(1 - 0.5k^2)}{(1 - k^2)} E(k) \right], \quad k = \left[\frac{4ra}{z^2 + (r+a)^2} \right]^{1/2} \\ B_z = \frac{\mu_0 I k}{4\pi \sqrt{a} r} \left[K(k) + \frac{(a+r)k^2 - 2r}{2r(1 - k^2)} E(k) \right] \end{array} \right.$$

where $K(k) \equiv \int_0^{\pi/2} \frac{d\theta}{\sqrt{1 - k^2 \sin^2 \theta}}$, $E(k) \equiv \int_0^{\pi/2} d\theta \sqrt{1 - k^2 \sin^2 \theta}$ (Elliptic Integrals)

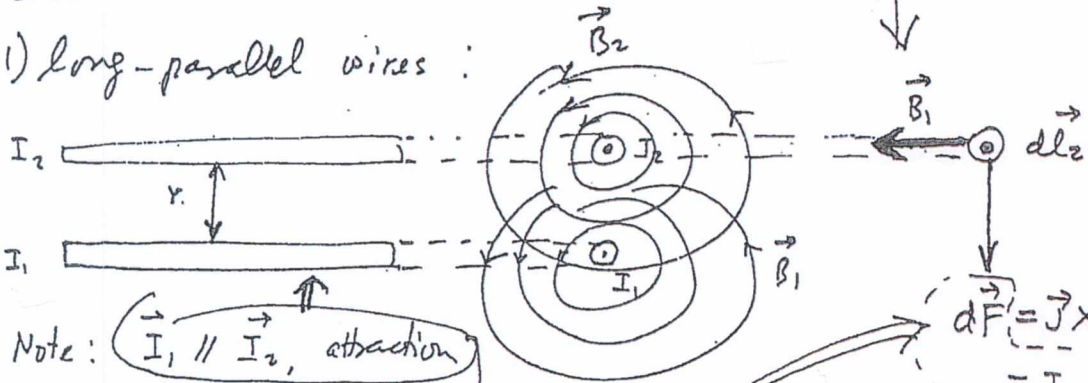
* Dolan, MFT (2013).

§ 3.2. Coil Forces

$$d\vec{F} = \vec{J} \times \vec{B} dV \quad (\text{newton})$$

Force produced by interaction of magnet coil currents with \vec{B}
 vol. of conductor

1) long-parallel wires:



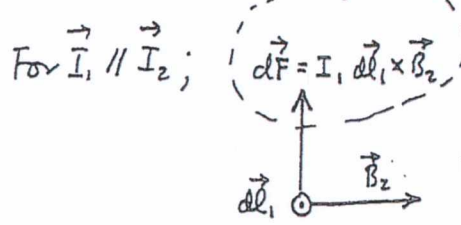
Note: $\vec{I}_1 \parallel \vec{I}_2$, attraction
 $\vec{I}_1 \parallel -\vec{I}_2$, repulsion

$$d\vec{F} = \vec{J} \times \vec{B} dV = I_2 dl_2 \times \vec{B}_1$$

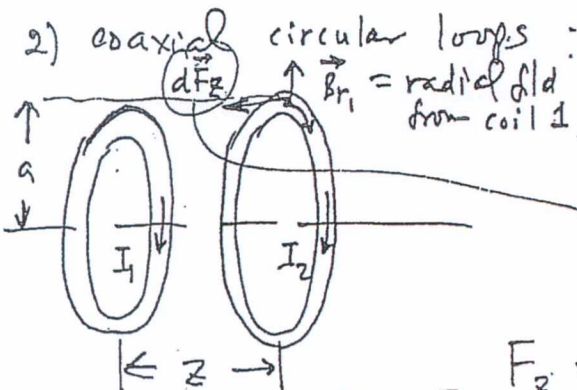
Since $B_1 = \frac{\mu_0 I_1}{2\pi r}$,

$$\left. \frac{dF}{dl} \right|_{\text{on wire 2}} = \frac{\mu_0 I_1 I_2}{2\pi r}$$

Note: Force per unit length on wire 1 has the same magnitude w/ opposite sign \Rightarrow attraction



2) coaxial circular loops:



$$d\vec{F}_z = I_2 dl_2 \times \vec{B}_{r1}$$

$$|d\vec{F}_z| = I_2 dl_2 B_{r1}$$

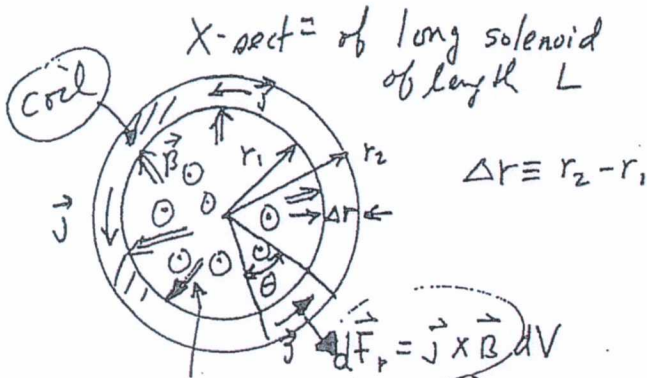
can be calculated from the circular loop

$$F_z = \int dF_z = I_2 B_{r1} \int dl_2 = 2\pi a \cdot I_2 B_{r1} \quad (\text{newton})$$

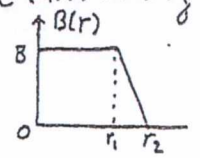
Note: B_z field produces F_r (radial force) but internal stress on the coil that F_r generated as a whole is zero.

Note: Example 20(1) Dopan, FR, Vol. III

3) solenoids :



Assume for "uniform" curr. density
 $B(r) = B \cdot \frac{(r_2 - r)}{\Delta r}$
 with the coil $r_1 < r < r_2$.



Internal magnetic pressure (outward)
 $= B^2 / 2\mu_0$

$$F_r = \int_{r_1}^{r_2} dF_r = \int_{r_1}^{r_2} J B \theta dV$$

$$= J \int_{r_1}^{r_2} B \frac{(r_2 - r)}{\Delta r} \cdot r d\theta \cdot dr \cdot dz$$

$$F_r = \frac{J B r_1 \Delta r d\theta dz}{2} \left(1 + \frac{\Delta r}{3r_1} \right)$$

Note: $(r_2 = r_1 + \Delta r)$ Eq. (20C7) Dolan, Vol. III

Since total current,
 $NI = J \Delta r L$,

$$B = \frac{\mu_0 NI}{L} \Rightarrow \mu_0 J \Delta r$$

$$J = \frac{B}{\mu_0 \Delta r}$$

Substituting J into Eq. (20C7), one obtains

$$F_r = \left(\frac{B^2}{2\mu_0} \right) r_1 d\theta dz \left(1 + \frac{\Delta r}{3r_1} \right) \quad (\text{newton}) \quad \text{Eq. (20C9) Dolan, Vol. III}$$

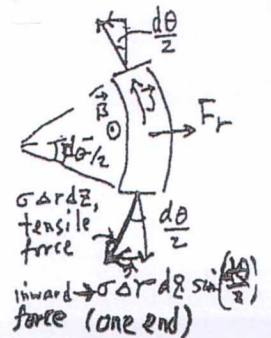
For $\Delta r \rightarrow$ small, $F_r \approx \left(\frac{B^2}{2\mu_0} \right) r_1 d\theta \cdot dz$
 mag. press. \cdot inner surface area

At equil.,

$$\left(\frac{B^2}{2\mu_0} \right) r_1 d\theta dz \left(1 + \frac{\Delta r}{3r_1} \right) = 2 \sigma \Delta r dz \sin\left(\frac{d\theta}{2}\right)$$

"outer" force

"inward" component of the tensile forces in the two ends



Recall

$$\left(\frac{\beta^2}{2\mu_0}\right) \cdot r_1 \cdot d\theta \cdot dz \left(1 + \frac{\Delta r}{3r_1}\right) = 2\sigma \Delta r dz \sin\left(\frac{d\theta}{2}\right)$$

$$\approx \sigma \Delta r dz d\theta$$

$$\therefore \text{Tensile stress, } \sigma = \left(\frac{\beta^2}{2\mu_0}\right) \left(\frac{r_1}{\Delta r} + \frac{1}{3}\right) \quad (\text{Pascal})$$

e.g. if $\frac{r_1}{\Delta r} = 5$, ^{and} $\beta = 10 \text{ T}$,

$$\text{then } \sigma = \frac{10^2}{2 \times 4\pi \times 10^{-7}} \left(5 + \frac{1}{3}\right) = 2.12 \times 10^8 \text{ Pa}$$

$$= \underline{\underline{212 \text{ MPa}}}$$

[Note: Yield stress of copper is $\sim 280 \text{ MPa}$].

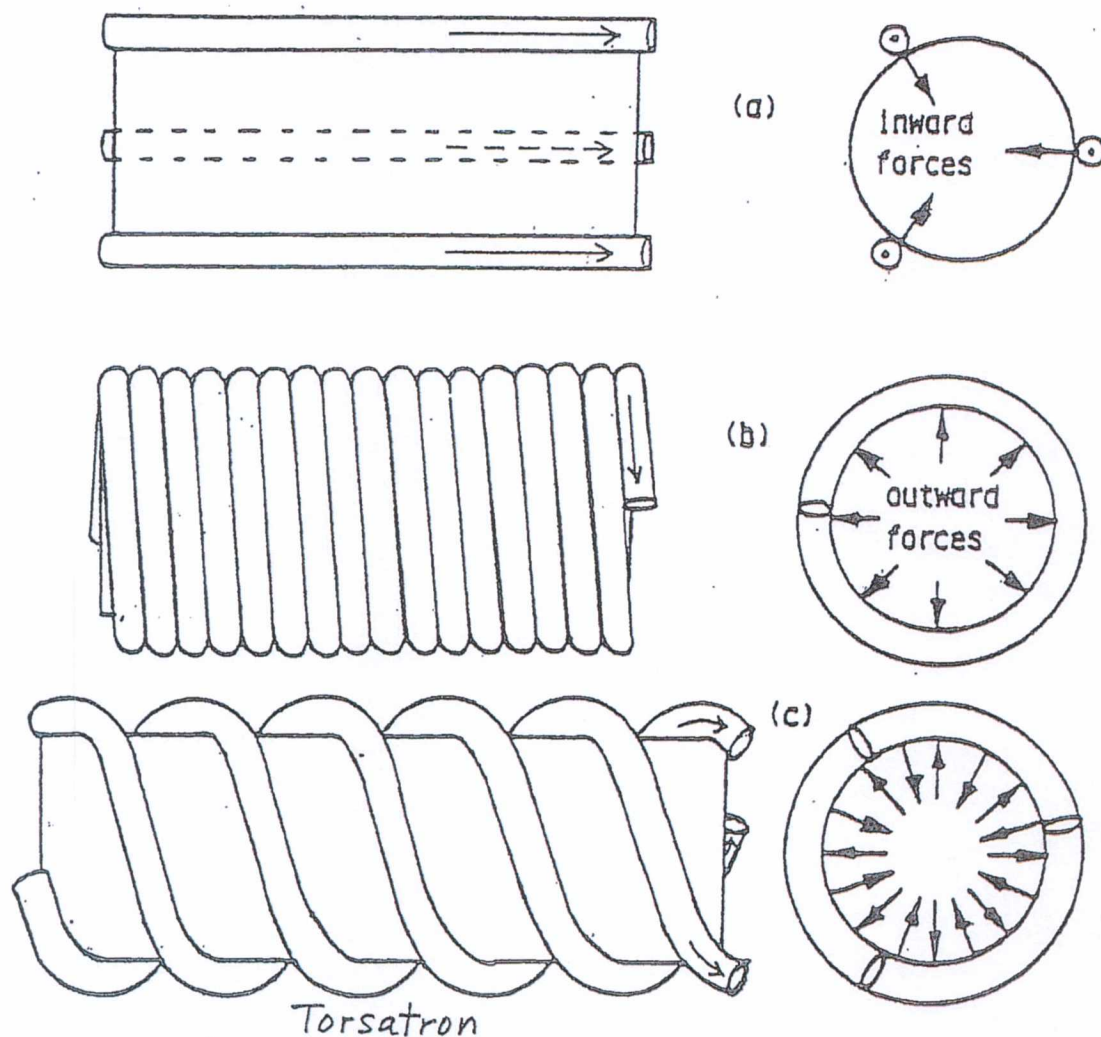
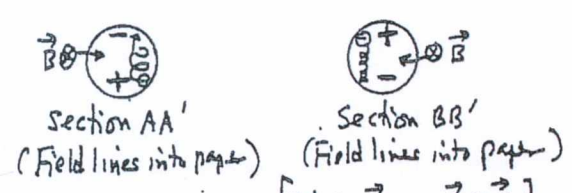
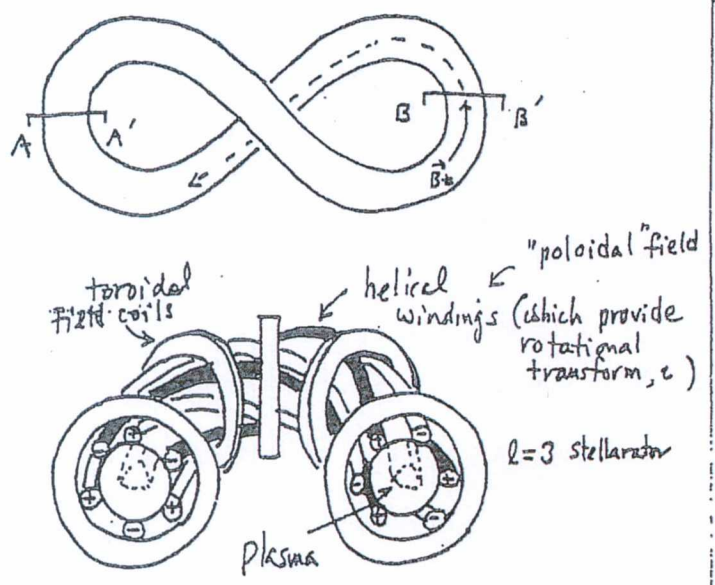


Fig. *20C4. Conductor configurations around a long, straight cylinder. (a) rods with parallel currents, (b) a solenoid, (c) helices. The helix has both the inward forces of the rods and the outward forces of the solenoid. [*=Dolan, Vol. III]

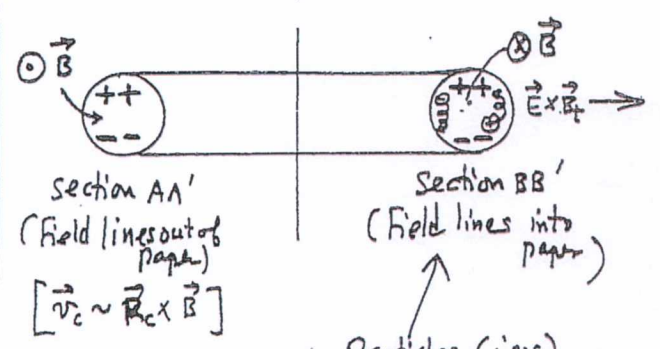
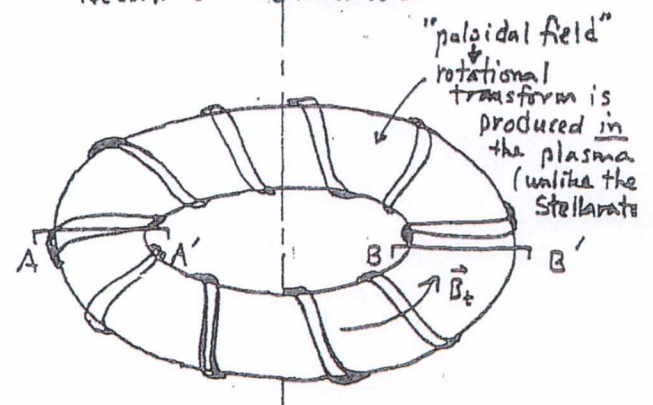
Stellarator



[Note: $\vec{v}_c \sim \vec{R}_c \times \vec{B}$]

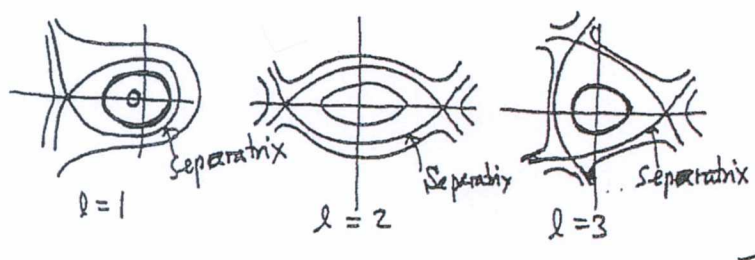
particle (ion) tends to drift upward here while at the other end it tends to drift downward, so that resultant charge separation is greatly reduced!

Recall: Tokamak

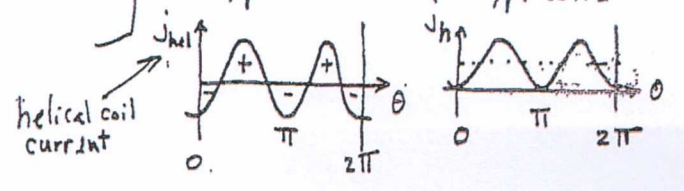
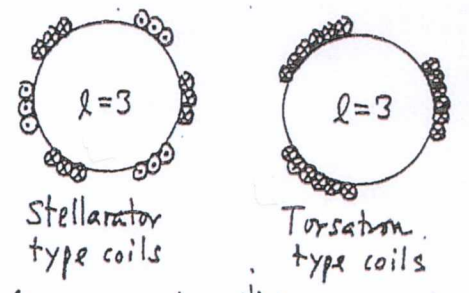


Particles (ions) drift upwards at both ends which result charge separation; hence $\vec{E} \times \vec{B}_t$ drift!

Magnetic surfaces of $l=1, 2,$ and 3 stellarator fields:



Note:



II. "PULSED" MAGNET SYSTEMS

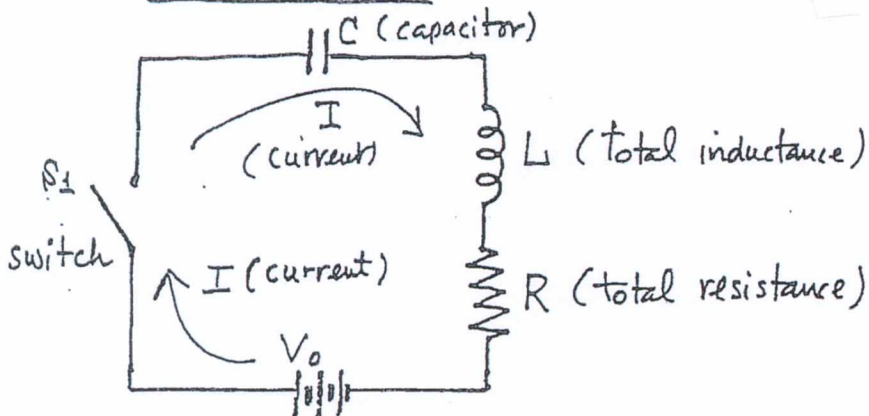
§3.3 RLC Circuit Equations

use "pulsed" power source to supply the current:

- higher coil currents possible (up to 32T in small-vol.) and
- less cooling requirements than "water-cooled" dc magnets;

but Fusion devices require large-volume pulsed magnetic fields
- large energy storage systems needed

RLC Circuits



$$\left[\begin{array}{l} \text{at } t=0, \quad q(\text{charge})=0 \\ \text{and } I(\text{current})=0 \end{array} \right]$$

Want to determine current, $I(t)$, and \vec{B} produced by $I(t)$

Recall Ohm's law: $V = IR$

Now; $V = \frac{q}{C}$ ($q = \text{charge on the capacitor}$),
across capacitor

$$\sqrt{\text{Voltage drop across } R = R \cdot I = R \cdot \frac{dq}{dt} \quad \left(\frac{dq}{dt} = \text{current} \right),}$$

$$\begin{aligned} \sqrt{\text{Voltage drop across } L} &= L \cdot \left(\frac{dI}{dt} \right) && (L = \text{assumed to be constant}) \\ &= L \cdot \left(\frac{d^2q}{dt^2} \right) && \left[\begin{array}{l} \uparrow \\ \text{e.g. plasma diamagnetism} \\ \text{will change } L \text{ in} \\ \text{an actual circuit} \end{array} \right] \end{aligned}$$

Since the sum of the voltages around the circuit is zero (i.e., Kirchoff's Law), one can write

$$L \left(\frac{d^2 q}{dt^2} \right) + R \left(\frac{dq}{dt} \right) + \frac{q}{C} - V_0 = 0 \quad \dots (250)$$

[Note: Initial Conditions; At $t=0$, $q=0$ and $I=0$.]
Set $D \equiv \frac{d}{dt}$;

$$\rightarrow \left[L D^2 + R D + \frac{1}{C} \right] q = V_0 \quad \dots (251)$$

Roots of this quadratic eqn.

$$D = \frac{-R \pm \sqrt{R^2 - 4L \frac{1}{C}}}{2L} = -\frac{R}{2L} \pm \sqrt{\left(\frac{R}{2L} \right)^2 - \frac{1}{LC}} \quad \dots (252)$$

$$= -a \pm \omega$$

Solution of eqn. (251) depends on the roots of (252); [Note this " ω " being different from (21B3); $\omega \leftrightarrow -\omega$ (here) (21B3)]

$$\text{i.e., whether } \left(\frac{R}{2L} \right)^2 - \frac{1}{LC} > 0 \quad \dots (i)$$

$$= 0 \quad \dots (ii)$$

$$< 0 \quad \dots (iii)$$

$$i) \text{ If } \left(\frac{R}{2L} \right)^2 - \frac{1}{LC} > 0 \quad \text{or} \quad R^2 > \frac{4L}{C} : \quad \left\{ \begin{array}{l} \text{Recall} \\ a \equiv \frac{R}{2L}, \omega \equiv \sqrt{\dots} \end{array} \right.$$

Then $a > \omega > 0$ and eqn. (252) has $D_1 = -a + \omega < 0$

and $D_2 = -a - \omega < 0$

\therefore General solution of eqn (250) is

$$q(t) = A_1 e^{-(a-\omega)t} + A_2 e^{-(a+\omega)t} + C V_0 \quad \dots (255)$$

$$\& \quad I(t) \equiv \frac{dq(t)}{dt} = -(a-\omega) A_1 e^{-(a-\omega)t} - (a+\omega) A_2 e^{-(a+\omega)t} \quad \dots (256)$$

At $t=0$, $\phi=0$ and $I=0$;

\therefore Equ. (255) $\rightarrow A_1 + A_2 = -cV_0 \dots \dots (257)$

Δ equ. (256) $\rightarrow (a-\omega)A_1 + (a+\omega)A_2 = 0 \dots (258)$

$\therefore A_1 = -\frac{(a+\omega)}{2\omega} cV_0 ; A_2 = \frac{(a-\omega)}{2\omega} cV_0$

\therefore Equ. (255) becomes

$$\phi(t) = \frac{cV_0}{2\omega} \left[-(a+\omega) e^{-(a-\omega)t} + (a-\omega) e^{-(a+\omega)t} + 2\omega \right] ; \quad (259)$$

& Equ. (256) yields to

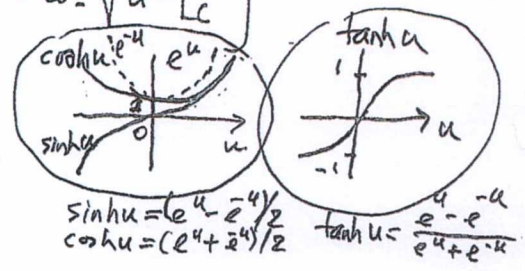
$$I(t) = \frac{cV_0(a^2-\omega^2)}{2\omega} \left[e^{-(a-\omega)t} - e^{-(a+\omega)t} \right] \dots (260)$$

Now, since $a^2 - \omega^2 \equiv \frac{R^2}{4L^2} - \frac{R^2}{4L^2} + \frac{1}{LC} = \frac{1}{LC}$,

equ. (260) is reduced to

$$I(t) = \frac{V_0}{2\omega L} \left[e^{\omega t} - e^{-\omega t} \right] \cdot e^{-at} = \frac{V_0}{2\omega L} e^{-at} \left[e^{\omega t} - e^{-\omega t} \right]$$

or $I(t) = \frac{V_0}{\omega L} e^{-at} \sinh \omega t$, $\left[a \equiv \frac{R}{2L} + \omega \equiv \sqrt{a^2 - \frac{1}{LC}} \right]$ $2 \sinh \omega t$



ii) If $\left(\frac{R}{2L}\right)^2 - \frac{1}{LC} = 0$ or $R^2 = \frac{4L}{C}$:

Recall $a \equiv \frac{R}{2L}$; then equ (252) becomes $\begin{cases} D_1 = -a < 0 \\ D_2 = -a < 0 \end{cases}$

Equ. (250)

$$\phi(t) = A_1 e^{-at} + A_2 t e^{-at} + cV_0 \dots (270)$$

& $I(t) = -aA_1 e^{-at} + A_2 e^{-at} - aA_2 t \cdot e^{-at} \dots (271)$

Initial conditions ($q=0$ and $I=0$ at $t=0$):

$$\text{Egu. (270)} \rightarrow A_1 + CV_0 = 0 \quad \therefore A_1 = -CV_0$$

$$\text{Egu. (271)} \rightarrow -aA_1 + A_2 = 0 \quad \therefore A_2 = -aCV_0 \equiv -\frac{R}{2L} CV_0$$

Hence, equ. (270) becomes

$$q(t) = CV_0 \left[-e^{-at} - at e^{-at} + 1 \right], \quad a \equiv \frac{R}{2L}$$

From Equ. (271), one also obtains

$$I(t) = CV_0 \cdot a \cdot \left[\cancel{+e^{-at}} - \cancel{e^{-at}} + at e^{-at} \right]$$

$$= a^2 CV_0 \cdot t \cdot e^{-at}$$

Since $a^2 \equiv \frac{R^2}{4L^2} = \frac{1}{4L^2} \left(\frac{4L}{C} \right) = \frac{1}{LC}$ ($\because R^2 = \frac{4L}{C}$ for this case ii),

$$\boxed{I(t)} = \frac{1}{L} \cdot CV_0 \cdot t \cdot e^{-at} = \frac{V_0}{L} t e^{-at}, \quad \left[a \equiv \sqrt{\frac{1}{LC}} \right]$$

$$\left[e^{-at} = 1 - at + \frac{(at)^2}{2!} - \dots \right]$$

Condition in the textbook (p. 621):

iii) If $\left(\frac{R}{2L} \right)^2 - \frac{1}{LC} < 0$ or $R^2 < \frac{4L}{C}$: [Condition for low R in the pulsed mag. circuits]

$$\text{Recall: } a \equiv \frac{R}{2L}, \text{ but set } b \equiv \sqrt{\frac{1}{LC} - \left(\frac{R}{2L} \right)^2} \quad [a, b > 0]$$

Then, from equ. (252),

$$D_1 = -a + ib, \text{ and } D_2 = -a - ib \quad \left[\text{This corresponds to eq. (21B3) in the text.} \right]$$

$$\therefore q(t) = A_1 e^{-at+ibt} + A_2 e^{-at-ibt} + CV_0$$

$$\text{or } \boxed{q(t)} = A_3 e^{-at} \cos bt + A_4 e^{-at} \sin bt + CV_0$$

$$= e^{-at} [A_3 \cos bt + A_4 \sin bt] + CV_0 \quad \dots (300)$$

Note:

$$\left[\sin x = \frac{e^{-ix} - e^{ix}}{2i} \right]$$

$$\left[\cos x = \frac{e^{ix} + e^{-ix}}{2} \right]$$

From equ. (300), current becomes

$$I(t) = e^{-at} [(-aA_3 + bA_4) \cos bt - (bA_3 + aA_4) \sin bt] \dots (301)$$

Initial conditions: At $t=0$, $i = I = 0$

\therefore Equ. (300) $\rightarrow A_3 + CV_0 = 0 \rightarrow \therefore A_3 = -CV_0$ Note the sign on the textbook (in errata p. 624)

& Equ. (301) $\rightarrow -aA_3 + bA_4 = 0 \rightarrow \therefore A_4 = \frac{a}{b} CV_0$

Equ. (300) \rightarrow

$$\therefore \boxed{\phi(t) = e^{-at} \cdot CV_0 [\cancel{\cos bt} + \left(\frac{a}{b}\right) \sin bt] + CV_0} \leftarrow \dots \text{cf. (21B6)}$$

$$= \frac{CV_0}{b} \cdot [-e^{-at} (b \cos bt + a \sin bt) + b]$$

&

$$I(t) = \frac{CV_0}{b} [a e^{-at} (b \cos bt + a \sin bt) - e^{-at} (-b^2 \sin bt + ab \cos bt)]$$

Note: $I \neq \frac{d\phi}{dt}$

$$= \frac{CV_0}{b} [(a^2 + b^2) \sin bt \cdot e^{-at}]$$

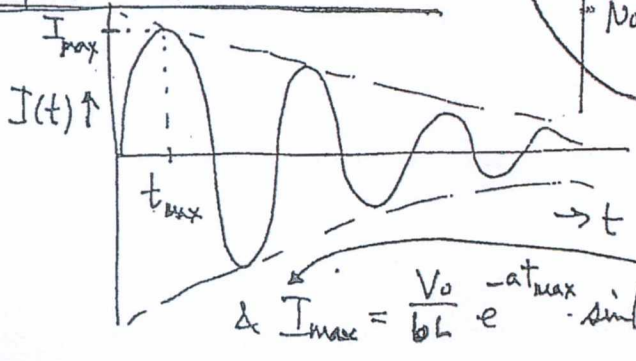
Since $a^2 + b^2 = \frac{R^2}{4L^2} + \left(\frac{1}{LC} - \frac{R^2}{4L^2} \right) = \frac{1}{LC}$,

$$\boxed{I(t) = \frac{V_0}{bL} \left[\frac{1}{LC} \cdot \sin bt \cdot e^{-at} \right]}$$

$$= \frac{V_0}{bL} e^{-at} \sin bt \leftarrow \dots \dots \text{cf. Equ. (21B7) o.k.}$$

$\begin{cases} a = \frac{R}{2L} > 0 \\ b = \sqrt{\frac{1}{LC} - a^2} > 0 \end{cases}$

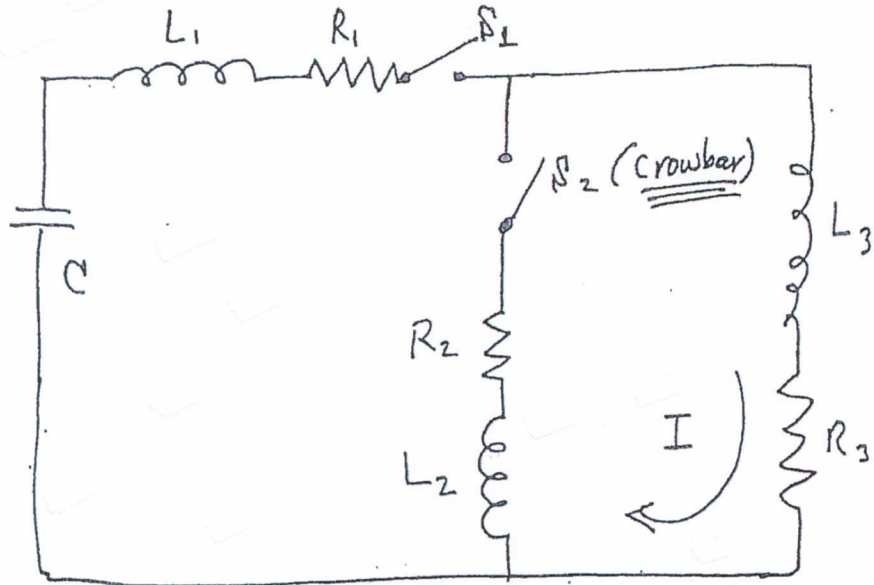
Damped Sinusoidal oscillation:



Note: I_{max} is obtained at $\frac{dI}{dt} = 0$;
 i.e., $\frac{dI}{dt} = \frac{V_0}{bL} e^{-at} [-a \sin bt + b \cos bt]$
 $\Rightarrow a \sin bt = b \cos bt$
 $\tan bt = \frac{b}{a}$
 $\therefore t_{max} = \left(\frac{1}{b} \right) \tan^{-1} \left(\frac{b}{a} \right)$

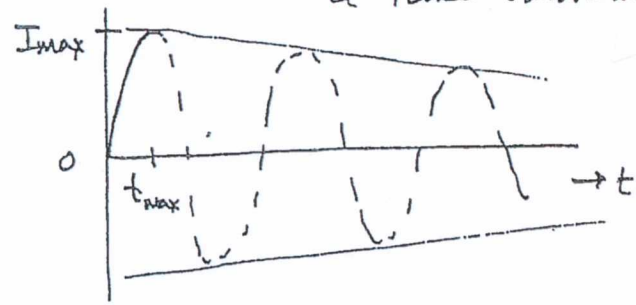
$\therefore I_{max} = \frac{V_0}{bL} e^{-at_{max}} \cdot \sin(bt_{max})$

Want to minimize the damped sinusoidal oscillation; instead, want the coil current rise up to a maximum value and stay there long.



close the second switch, crowbar, when $I = I_{max}$; i.e., short-circuiting coil L_3 at I_{max} .

Then, the coil current gradually decays with a time constant, τ :



$$\tau = \sqrt{\frac{L_2 \times L_3}{R_2 \times R_3}}$$

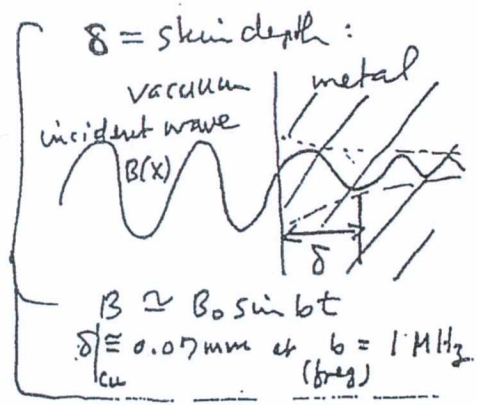
- Pulsed Magnets continued -

A) Typically dc resistance of conductors is estimated via

$$R = \int_0^l dx \frac{\eta}{S}$$

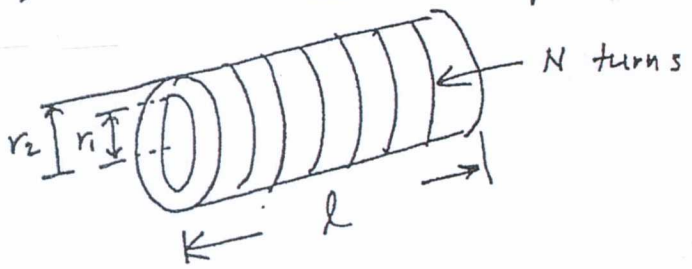
(eg. (21B10))

where R = resistance
 η = resistivity of metal ($\Omega \cdot m$)
 S = conductor X-sectional area (m^2)
 l = length of item (m)



Note: In pulsed device, "skin effect"
 $\delta = \sqrt{\frac{2}{\mu \sigma b}}$, μ = permeability ($\frac{H}{m}$)
 σ = conductivity ($\frac{A}{V \cdot m}$)
 $[b] = [\frac{1}{t}]$
 may cause non-uniform current distribution over the whole X-section of the coil.

B) Inductance of a uniform-current density solenoid:



$$\alpha = \frac{r_2 (m)}{r_1 (m)}$$

$$\beta = \frac{l}{2r_1}$$

$$\frac{L}{N^2 r_1} \propto \alpha, \beta$$

where L is in Henry
 r_1, r_2, l in meters

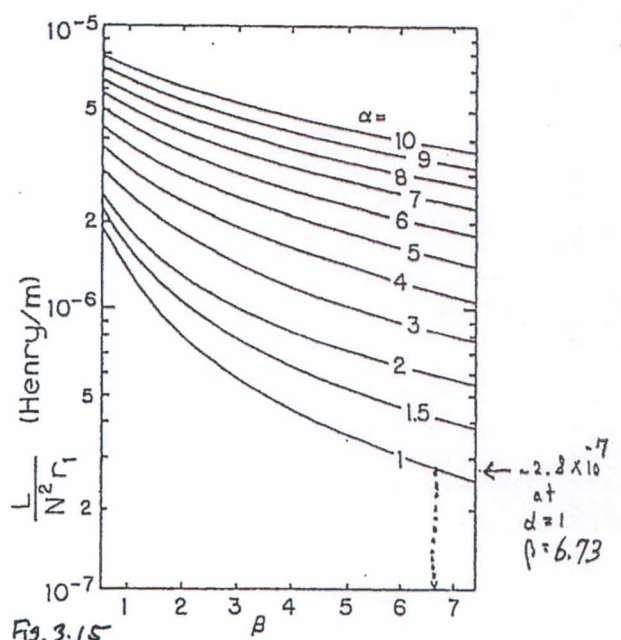
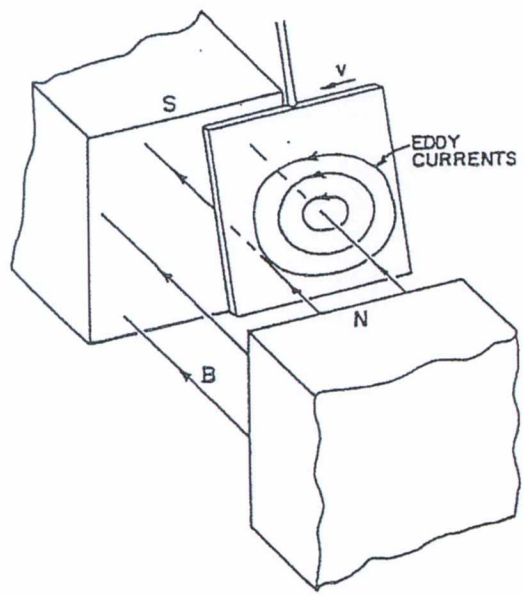


Fig. 3.15
 & Fig. 21B5. Inductance of a uniform-current-density solenoid, as a function of $\beta = l/2r_1$ for various values of $\alpha = r_2/r_1$. The inductance L is in Henry, N is the number of turns, and the solenoid length l and radii r_1 and r_2 are in metres. From D. B. Montgomery, Reports on Progress in Physics 29, 69-104 (1963).
 © 1963 The Institute of Physics. [Dolan, Vol. IV]

Note: Eddy currents in magnet design.



Eddy currents are creating "opposing" fields (like Lenz's rule)

Fig. A The eddy currents in the copper pendulum.

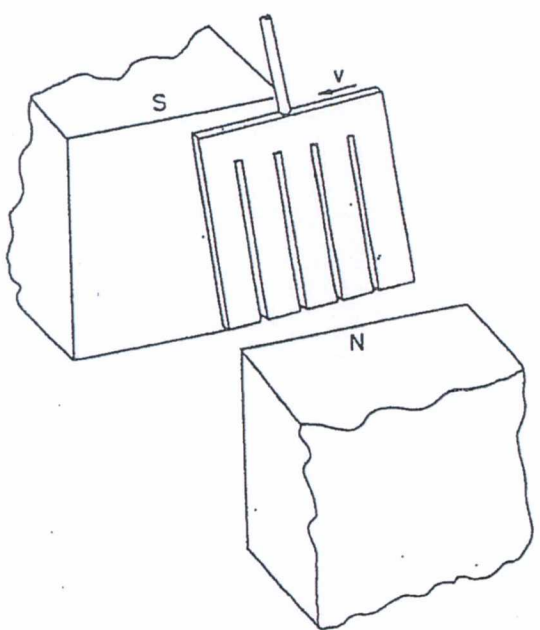


Fig. B Eddy-current effects are drastically reduced by cutting slots in the plate.

Theta Pinch Exp't

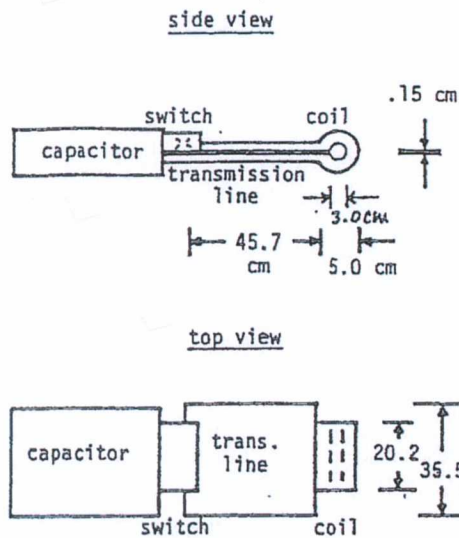


Fig. 21P1. Theta pinch experiment.

- A small theta pinch experiment has the following parameters:
 - one-turn aluminum coil
inside diameter = 3.0 cm
outside diameter = 5.0 cm
length = 20.2 cm
 - parallel plate transmission line (aluminum, $\eta = 2.8 \times 10^{-8} \Omega \cdot m$)
width = 35.5 cm
length = 45.7 cm
thickness = 1.3 cm
insulation gap = 0.15 cm
 - capacitor
capacitance = 15.0 μF
inductance = 5 nH
resistance = negligible
charging voltage = 20 kV
 - switch (rail type spark gap)
inductance = 5 nH
assume resistance = 1 m Ω

(a) Calculate the total circuit resistance and inductance.

a) Resistance, R:

Since the components of the theta pinch exp't are in a series arrangement,

$$R_{Total} = R_{Switch} + R_{trans. line} + R_{coil} + R_{capacitor} \xrightarrow{\text{negligible}}$$

Note: $R_{Switch} = 1 \text{ m}\Omega = 1 \times 10^{-3} \Omega$ (given)

The dc resistance of conductors in general is given by $R = \frac{\rho l}{A}$ (21B10),
i.e., $R = \int_0^l dx \frac{\eta}{A}$ = $\frac{\eta}{A} (l - 0)$, where $\eta = \text{resistivity of "metal"}$
Dolan, Vol. III, 2.6.3.40,

$$\Rightarrow \eta_{Al} = 2.8 \times 10^{-8} (\Omega \cdot m)$$

$$l = \text{length of conductor} = 45.7 \text{ cm} = 0.457 \text{ (m)}$$

For transmission line,

(A) = x-sectional area of conductor (m^2)
 e.g.) $A \Rightarrow \text{width} \times \text{thickness}$
 $= (0.355 \text{ m}) \times (0.013 \text{ m})$
 $= 0.00462 \text{ m}^2$

Then,

$$R_{\text{trans line}} = 2 \int_0^l dx \frac{\eta}{S} = 2l \frac{\eta}{S} = 2 \times (0.457 \text{ m}) \frac{(2.8 \times 10^{-8} \Omega \cdot \text{m})}{0.00462 \text{ m}^2}$$

$$= \underline{5.54 \times 10^{-6} \Omega}$$

$$R_{\text{coil}} = \frac{\eta_{\text{Al}} \cdot l}{S_{\text{coil}}} = \frac{(2.8 \times 10^{-8} \Omega \cdot \text{m}) (0.202 \text{ m})}{1.256 \times 10^{-3} \text{ m}^2} = \underline{4.50 \times 10^{-6} \Omega}$$

Coil cross-section

$$\left[\because S_{\text{coil}} = \pi(r_2^2 - r_1^2) = \pi((0.025 \text{ m})^2 - (0.015 \text{ m})^2) = 1.256 \times 10^{-3} \text{ m}^2 \right]$$

$2r_2$ $2r_1$

$$\therefore R_{\text{Total}} = R_{\text{switch}} + R_{\text{trans. line}} + R_{\text{coil}}$$

$$= (1 \times 10^{-3} \Omega) + (5.54 \times 10^{-6} \Omega) + (4.50 \times 10^{-6} \Omega)$$

$$= 1.010 \times 10^{-3} \Omega$$

$\therefore R_{\text{tot}} \approx 1 \text{ m}\Omega$ (About the same resistance of the switch)

Inductance, L:

The total circuit inductance is given by

$$L_{\text{Tot}} = L_{\text{capacitor}} + L_{\text{switch}} + L_{\text{trans. line}} + L_{\text{coil}}$$

Note: $L_{\text{capacitor}} = 5 \text{ nH} = 5 \times 10^{-9} \text{ H}$ (given)

$L_{\text{switch}} = 5 \text{ nH} = 5 \times 10^{-9} \text{ H}$ (given)

- a) For a uniform current-density solenoid of length, l , inner & outer radii of r_1 and r_2 with N turns, the inductance L can be found by using Fig. 21 B 5 (Dolan, Vol. III) & Fig. 3.15

Inductance L from Fig. 3.15 & Fig. 21B5 can be found in terms of

For the coil,
 $\alpha = \frac{r_2}{r_1}$, $\beta = \frac{l}{2r_1}$; $l = 0.202 \text{ m}$, $r_1 = 0.015 \text{ m}$, $r_2 = 0.025 \text{ m}$

Hence, $\alpha \approx 1$ (accounting for the "skin effects" of "pulsed" exp't)

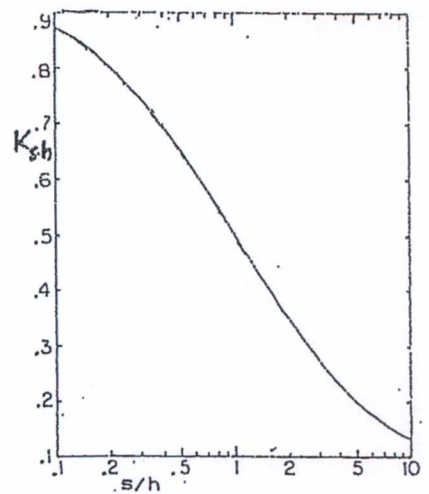
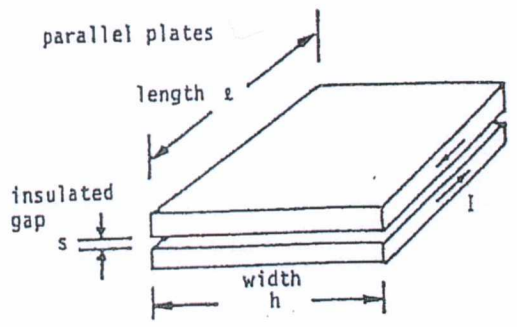
$$\beta = \frac{0.202}{2(0.015)} = 6.73$$

\therefore From Fig. 21B5, $\frac{L}{N^2 r_1} \approx 2.8 \times 10^{-7} \frac{\text{H}}{\text{m}}$ (at $\alpha \approx 1$, $\beta = 6.7$)

$\therefore L_{\text{coil}} = N^2 r_1 (2.8 \times 10^{-7} \frac{\text{H}}{\text{m}})$ [N = 1 turn coil]
 $= (1)^2 (0.015 \text{ m}) (2.8 \times 10^{-7} \frac{\text{H}}{\text{m}}) = 4.2 \times 10^{-9} \text{ H} = \underline{4.2 \text{ nH}}$

b) The inductance of a parallel plate transmission line is given by Eqn. (21B11);

i.e., $L = \mu_0 \frac{s}{h} l \frac{K_{sh}}{h}$ (Henry), where K_{sh} is found from Fig. 21B7 below.



For s (insulated gap) = $0.15 \text{ cm} = 0.0015 \text{ m}$

h (width) = $35.5 \text{ cm} = 0.355 \text{ m}$

l (length) = 0.457 m

$$\frac{s}{h} = \frac{0.0015}{0.355} = 4.22 \times 10^{-3}$$

Hence, $K_{sh} \approx 1$ at $\frac{s}{h} = 4.22 \times 10^{-3}$

Fig. 3.16d
 Fig. 21B7. Values of K_{sh} as a function of (s/h) for the inductance of a parallel plate transmission line. If $s/h \ll 1$, $K_{sh} = 1$. From H. Knoepfel, Pulsed High Magnetic Fields, American Elsevier, New York, 1970, Fig. A1.21, p. 325.

[Note: $K_{sh} \approx 1$ at $\frac{s}{h} \ll 1$]

Then,

$$L_{\text{trans. line}} = \mu_0 s l \frac{K_{sh}}{h} = \left(4\pi \times 10^{-7} \frac{\text{H}}{\text{m}}\right) \frac{(0.0015 \text{ m})(0.457 \text{ m})(1)}{0.355 \text{ m}} = 2.426 \times 10^{-9} \text{ H} = 2.426 \text{ nH}$$

$$\begin{aligned} \therefore L_{\text{Total}} &= L_{\text{capacitor}} + L_{\text{switch}} + L_{\text{trans. line}} + L_{\text{coil}} \\ &= (5 \times 10^{-9} \text{ H}) + (5 \times 10^{-9} \text{ H}) + (2.426 \times 10^{-9} \text{ H}) + (4.2 \times 10^{-9} \text{ H}) \\ &= 16.626 \times 10^{-9} \text{ H} \end{aligned}$$

$$\therefore L_{\text{total}} = 16.63 \text{ nH}$$

§ 3.4 Distribution of \vec{j} and \vec{B}

From Maxwell's eqn, \vec{E} (Ohm's law): $\vec{E} + (\vec{u} \times \vec{B}) = \eta \vec{j}$

$$\begin{aligned} \frac{\partial \vec{B}}{\partial t} &= -\vec{\nabla} \times \vec{E} = -\vec{\nabla} \times (-\vec{u} \times \vec{B} + \eta \vec{j}) \quad [\vec{\nabla} \times \vec{B} = \mu_0 \vec{j}] \\ &= +\vec{\nabla} \times (\vec{u} \times \vec{B}) - \frac{\eta}{\mu_0} \vec{\nabla} \times (\vec{\nabla} \times \vec{B}) \\ &= \underbrace{\vec{\nabla} \times (\vec{u} \times \vec{B})}_{\text{plasma } (\vec{u}) \text{ \& mag. fld. lines } (\vec{B}) \text{ moving together (flux lines "frozen" into the plasma)}} + \underbrace{\left(\frac{\eta}{\mu_0}\right) \nabla^2 \vec{B}}_{\text{diffusion of mag. fld. lines thru the plasma}} \quad (\text{assuming spatial variations of } \eta \text{ are negligible}) \end{aligned}$$

With $\vec{u} = 0$,

$$\frac{\partial \vec{B}}{\partial t} = \frac{\eta}{\mu_0} \nabla^2 \vec{B} = \left(\frac{1}{\sigma \mu_0}\right) \nabla^2 \vec{B} \quad \left[\text{conductivity } \sigma \equiv \frac{1}{\eta} \text{ (resistivity)} \right]$$

Similarly $\frac{\partial \vec{j}}{\partial t} = \nabla^2 \vec{j} \cdot \left(\frac{1}{\sigma \mu_0}\right)$ Eq. 3.43 & (Eq. 2101) [Dolan, Vol. III] [$\mu_0 \leftrightarrow \mu \leftrightarrow \left(\frac{\text{H}}{\text{m}}\right)$]

also, $\frac{\partial T}{\partial t} = \nabla^2 T \cdot \left(\frac{K}{C_v} \right)$,
 note the heat conduction eqn.
 $K =$ thermal conductivity
 $C_v =$ specific heat
 $T =$ temperature

\therefore Diffusion of current density (cf. $\frac{\partial \vec{J}}{\partial t}$) and magnetic field (cf. $\frac{\partial \vec{B}}{\partial t}$) into a conductor is analogous to the diffusion of heat into solid (cf. $\frac{\partial T}{\partial t}$)

From Eqn. (21C1),
 $\frac{\partial B}{\partial t} \sim \frac{B}{\tau}$, $\nabla^2 B \sim \frac{B}{l^2}$; $\tau =$ characteristic diffusion time
 $l =$ " " length

Then Eqn. (21C1) simplifies to

$$\boxed{\frac{1}{\tau} = \frac{1}{\sigma \mu l^2}} \quad \left[\begin{array}{l} \sigma \text{ (conductivity) and } \mu \text{ (permeability) are} \\ \text{readily known for a given conductor} \end{array} \right]$$

§3.5 Energy Storage Systems

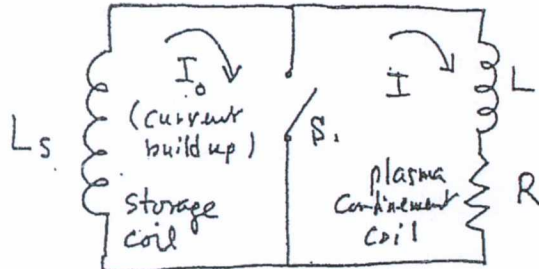
Capacitor bank stores electrical energy!
 need
 long life time ($\sim 10^6$ shot)
 low self-inductance (to make I_{max} very large)
 low resistance $\therefore I_{max} \sim \frac{1}{L}$
 + low cost

[e.g. Scyllac at LANC stores 10 MJ at 60 kV, 1.85 μ F]

Work: $dW = \left(\frac{Q}{C} \right) dq$, $W = \int_0^Q \frac{Q}{C} dq = \frac{Q^2}{2C}$
↑ Voltage, V_0

Work \rightarrow Potential en. $\therefore U = \frac{Q^2}{2C} = \frac{1}{2} C V_0^2 = \frac{1}{2} Q V_0$
(W) (V)

Inductive energy storage system:
(charging supply not shown)



i) I_0 build up w/ S_1 switch closed



$$\text{en. stored} : \frac{1}{2} L_s I_0^2$$

ii) Open switch S_1 , current I flows
through the load coil L



Design of high-current switch S_1 difficult

$$\text{Transfer efficiency (to the load coil)} = \frac{\frac{1}{2} L I_{\text{max}}^2}{\frac{1}{2} L_s I_0^2} \leq \frac{L_s L}{(L_s + L)^2} \quad (21D1)$$

$$\approx 25\% \quad (\text{when } L = L_s)$$

Need higher than 25% ! \rightarrow 90% !

[w/ Capacitor bank
in parallel w/
switch S_1 !]

Chapt. 4 SUPERCONDUCTING MAGNETS

4.1 Superconductivity

What is superconductivity?

- The ability of superconductors to carry current w/o resistance. [cf. BCS theory, 1957]
 - when mutual attraction between e^- s thru "phonon" becomes stronger than the mutual Coulomb repulsion, frictional force (i.e., resistivity) becomes zero.

Why superconducting magnets?

- To generate an intense, large volume magnetic field "economically" ($> 10T$)

e.g. Typical magnetic fields required for

Stellarator	$\sim 8T$	ITER $\sim 12T-13T$
Tokamak	$10 \sim 15T$	{ cf. Large Coil Task, LCT } & Tore Supra in France
mirror	$\sim 20T$	{ cf. MFTF-B magnet system
RFP	$\sim 24T$	

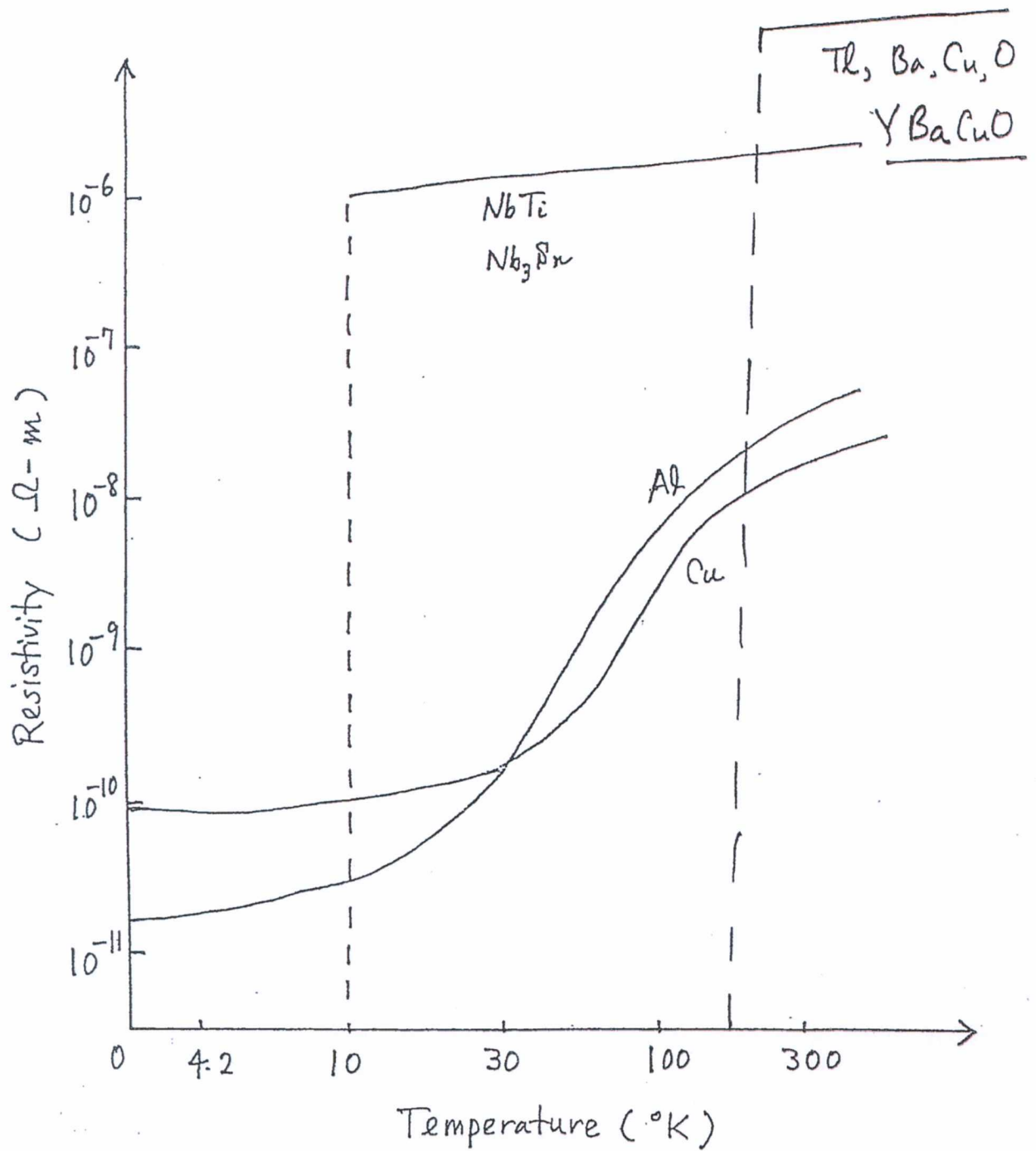
e.g. 1) In JET: 180-280 MW Joule-losses at a current density of 1370-2500 A/cm² in water-cooled copper coils will occur for operation periods of 30 sec.

2) In the INTOR design, the required overall current density is ~ 2000 A/cm². If we assume that this could be taken by copper even for continuous operation, the losses would be about 4 GW!

* ITER now requires 3700 A/cm² in Nb₃Sn superconductor TF coils.

act like "bosons"

+ BCS theory: The conduction electrons condense into a ground state composed of Cooper pairs which consist of electrons in equal and opposite momentum and spin states, i.e. $(k\uparrow, -k\downarrow)$. This condensation occurs when the attractive interaction between electrons due to phonons exceeds the repulsive Coulomb interaction. (The physical idea of the phonon interaction is that electrons polarize the medium by attracting positive ions, which in turn attract other electrons.)



Resistivities of various conductors as function of Temperature. Note that NbTi and Nb_3Sn are the superconducting materials.

1988

H. Maeda, of the National Institute for Metals ("Kinzai-Ken"), Tsukuba, discovered BiSrCaCuO (BSCCO); now in two forms: Bi-2212 ($T_c = 85$ K); and Bi-2223 ($T_c = 110$ K).

Z.Z. Sheng and A.M. Hermann at U. of Arkansas discovered TlBaCaCuO (Tl-2223), $T_c \sim 125$ K.

1993

P. W. Chu discovered HgBaCaCuO (Hg-1223), $T_c \sim 135$ K (164 K under a pressure of 300 atm).

Table 4.12 lists some superconductors of interest.

Table 4.12 Some high temperature superconductors. (Schlachter, 2010.)

Superconductor	Name	T_c , K	Uses
YBa ₂ Cu ₃ O ₇	YBCO	92	Bulk material, tapes, thin films
REBa ₂ Cu ₃ O ₇	REBCO (RE=Y, Yb, Dy, ...)	$\sim 88-96$	Bulk material, tapes, thin films
Bi ₂ Sr ₂ CaCu ₂ O ₈	BiSCCO(2212),	85	Bulk material, wires
Bi ₂ Sr ₂ Ca ₂ Cu ₃ O ₁₀	BiSCCO(2223), Bi-2223	110	Tapes

There are thousands of materials with superconductivity, but only a few with $T_c > 10$ K, $B_c > 10$ T, $J_c > 1$ MA/cm² at 5 T, and metallurgical properties (such as ductility) suitable for winding into magnet coils. The critical fields of a few HTS are compared with those of LTS in Figure 4.48

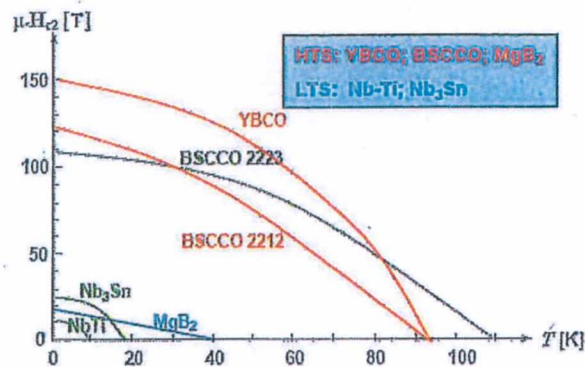


Figure 4.48 Parameters of some high-temperature superconductors. HTS = high temperature superconductors, LTS = low temperature superconductors. (Minervini and Iwasa, 2003).

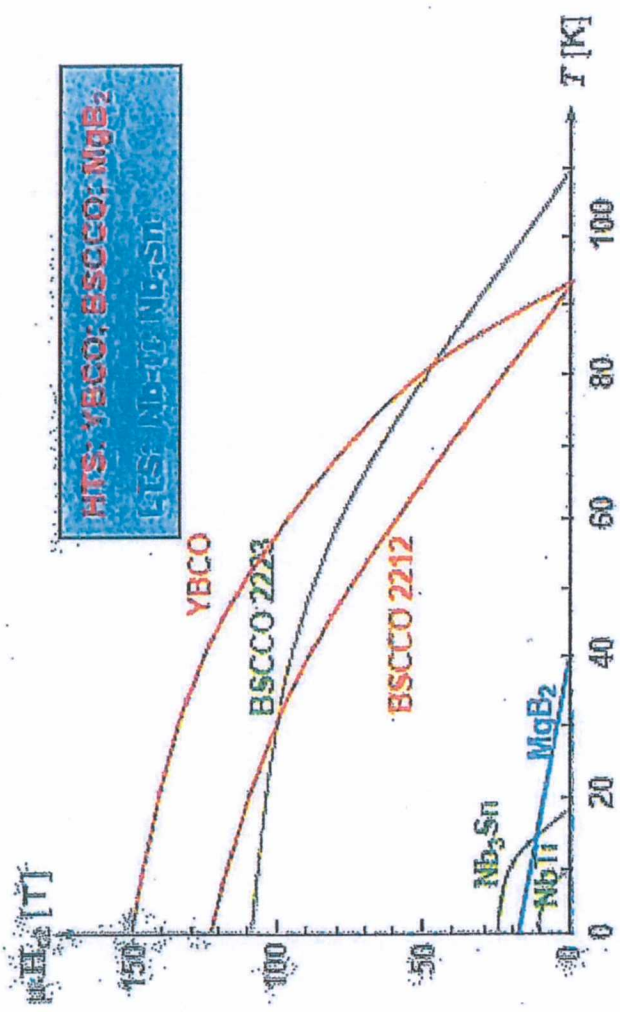
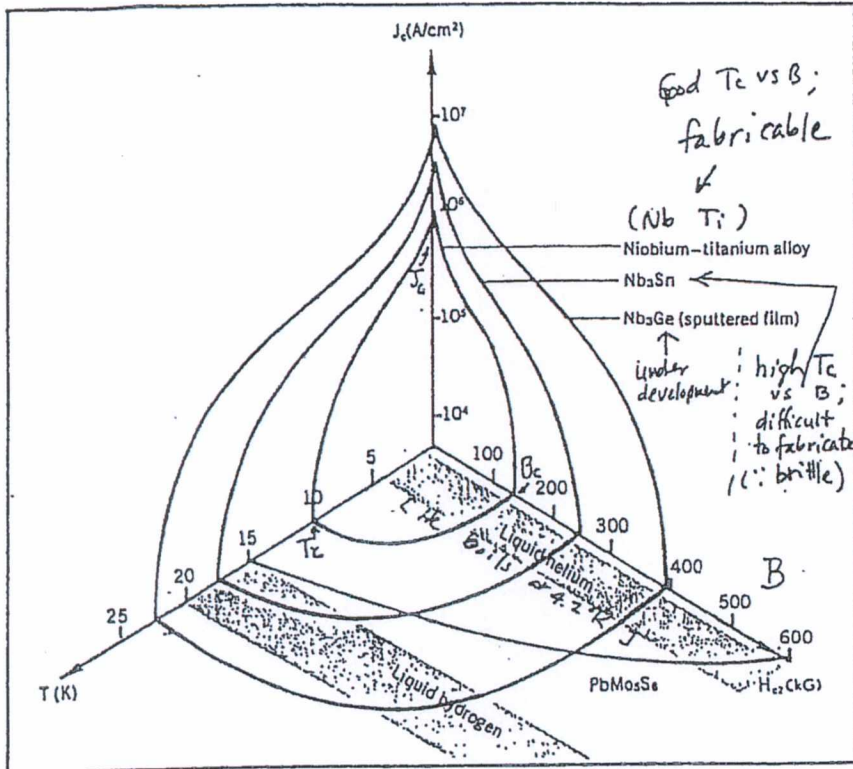


Figure 4.48 Parameters of some high-temperature superconductors. HTS = high temperature superconductors, LTS = low temperature superconductors. (Minervini and Iwasa, 2003).



Critical characteristics of high-field superconductors. The critical current density J_c (on a log scale) is shown as a function of the critical upper magnetic field H_{c2} and the temperature T for three readily available superconductors. A plot of H_{c2} versus T is also shown for the ultrahigh-field compound $PbMoS_6$. (After J. R. Gavaler and S. Foner.)

Note:
 T_c = maximum value of temperature ($^{\circ}K$) within which superconductivity holds (or critical temperature)

B_c = critical magnetic field [$10kG \equiv 1 Tesla$]

J_c = critical current density [$1 \frac{A}{cm^2} = 10^4 \frac{A}{m^2}$]

e.g., Domain within $10^{\circ}K$, $\sim 140 kG$, and $\sim 10^6 A/cm^2$ is superconductivity region for NbTi alloy. The material becomes "normal conductors" outside this domain.

At $T = 0^{\circ}K$ (w/o \vec{B} or \vec{J} applied), all e^- s are Cooper paired; however, as $T \uparrow$, Cooper pairs will be broken:

e.g. at $T = 0^{\circ}K$, the energy gap of the electron system in Cooper pair is $2\Delta|_{T=0^{\circ}K} \approx 3.5 kT_c$;
 ↑ Boltzmann const. critical temp.

As $T \uparrow$, $\Delta \rightarrow 0$ (electron-phonon-electron interactions \downarrow , i.e., attraction bet $^{\circ}$ e^- s) such that the temperature where $\Delta = 0$ (and all e^- s become unpaired) is T_c (critical temperature).

Also, note: $\xi \equiv$ "coherence length" over which the transition bet $^{\circ}$ superconducting region and a normal region occurs. \approx average separation between any two paired electrons ($\sim 1 \mu m$ in pure metals and much shorter for impure metals.)

diamagnetism

Tendency of excluding an applied magnetic field from the interior of a superconductor (self-shielding effect):

Current density (due to n_s superconducting electron density),
 $\vec{J} = -n_s e \vec{v}$

Recall: $\left. \begin{array}{l} \text{De Broglie's} \\ p c l e \leftrightarrow \text{wave relation,} \\ \lambda = \frac{h}{p}, \quad k = \frac{2\pi}{\lambda} = \frac{2\pi p}{h} \end{array} \right\}$
 p c l e momentum

momentum of p c l e in \vec{B} fld,
 $\vec{p} = m\vec{v} + q\vec{A}$

[Note: For Cooper pair, $m = 2m_e$ & $q = -2e$]
 The phase difference betⁿ any two points, a and b, of the Cooper pair along the wave,

$\phi_b - \phi_a = - \int_a^b dl \cdot \vec{k}$
 $= - \left(\frac{2\pi}{h} \right) \int_a^b dl \cdot (2m_e \vec{v} - 2e\vec{A})$
 $\Rightarrow \frac{\phi_b - \phi_a}{(b-a)} = - \left(\frac{4\pi}{h} \right) (m_e \vec{v} - e\vec{A})$
 $\vec{\nabla} \phi$
 $\vec{v} = \left(\vec{\nabla} \phi - \frac{4\pi}{c} e \vec{A} \right) \cdot \left(\frac{-h}{4\pi m_e} \right)$
 $\therefore \vec{v} = - \frac{h \vec{\nabla} \phi}{4\pi m_e} + \frac{e}{m_e c} \vec{A}$

$\vec{J} = n_s e \frac{h \vec{\nabla} \phi}{4\pi m_e} - n_s \frac{e^2}{m_e} \vec{A}$

$\vec{\nabla} \times \vec{J} = -n_s \frac{e^2}{m_e} \vec{B}$

since $[\vec{\nabla} \times \vec{\nabla} \phi \equiv 0] + [\vec{\nabla} \times \vec{A} \equiv \vec{B}]$

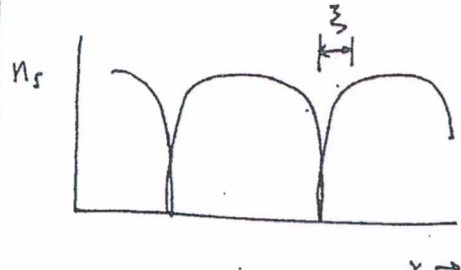
But $\vec{\nabla} \times \vec{B} = \mu_0 \vec{J}$; $\therefore (\vec{\nabla} \times \vec{J}) = \vec{\nabla} \times \left(\frac{\vec{\nabla} \times \vec{B}}{\mu_0} \right) = \frac{1}{\mu_0} [\vec{\nabla} (\vec{\nabla} \cdot \vec{B}) - \nabla^2 \vec{B}] = -n_s \frac{e^2}{m_e} \vec{B}$

$\frac{1}{\mu_0} \nabla^2 \vec{B} = +n_s \frac{e^2}{m_e} \vec{B}$

$\frac{d^2 B}{dx^2} = \frac{B}{\lambda_L^2}$; where $\lambda_L \equiv \sqrt{\frac{m_e}{n_s e^2 \mu_0}} = 5.36 \times 10^{-6} \sqrt{n_s}^{-1}$; = London Penetration length

At $n_s = 10^{28} \text{ m}^{-3}$
 $\lambda_L = 5 \times 10^{-6} \text{ m}$
 $= 0.05 \text{ } \mu\text{m}$
 $\therefore B$ is attenuated towards metal surface.
 $B = B_0 e^{-x/\lambda_L}$
 at $x=0$ (surface)

Types of superconductors

	TYPE I	TYPE II
coherence length, ξ (or av. spacing bet ^m e^- pairs)	$\xi > \sqrt{2} \lambda_L$ ($\lambda_L =$ London Penetration length)	$\xi < \sqrt{2} \lambda_L$
materials	Most pure metal superconductors, (e.g., Al, Pb, Hg, Ta, Sn, Zn)	Nb, V (pure metals) <u>Nb₃Sn</u> (can carry hi-current at 8T; good at 8 < B < 13T) Nb Zr (obsolete; replaced by NbTi) NbTi (not suitable for B > 8.5T) <u>V₃Ga</u> (has high current density when B > 13T)
	unsuitable for winding magnet coils $\therefore B_c = B_{c0} [1 - (\frac{T}{T_c})^2]$ ↑ small [cf. table 22A1]	

Brittle + difficult to fabricate!

To be a satisfactory winding magnet, superconducting materials need:

- high critical temp, T_c
- high critical mag. fld, B_{c2}
- high critical J_c
- commercial availability
- good mechanical properties, e.g. ductility

(For Type II)

$$B_{c2} \approx \frac{\Phi_0}{(2\xi)^2} \text{ (Tesla)}$$

↑ Quantized flux (fluxon); $\frac{h}{2e} = \frac{6.626 \times 10^{-34}}{2 \times 1.6 \times 10^{-19}} = 2.07 \times 10^{-15} \text{ weber}$

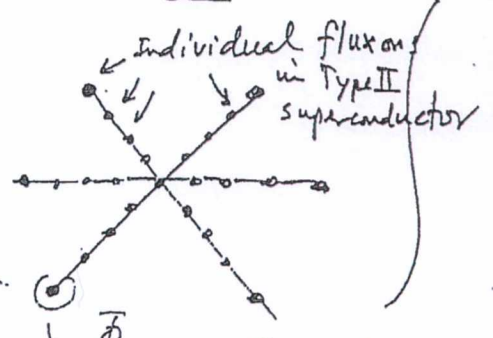


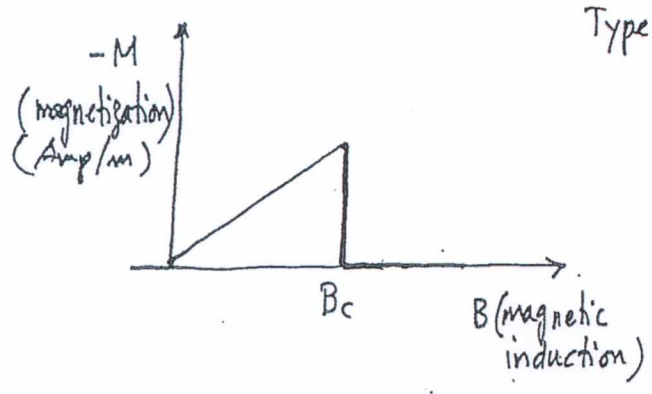
Fig. 22A3 & Fig. 22A4

(*) units:

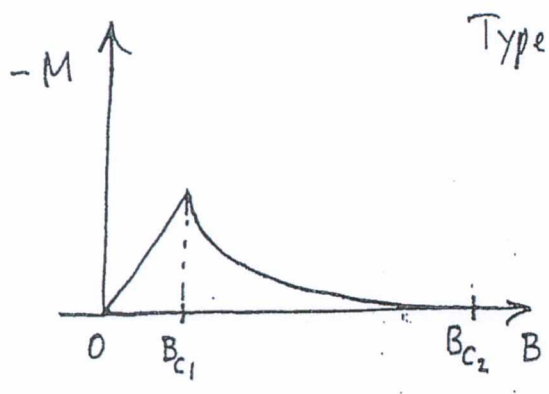
$$\left[\frac{J \cdot sec}{G} = \text{volt} \cdot \text{sec} \right]$$

$$[\nabla \times E] = \left[\frac{\partial B}{\partial t} \right] \rightarrow \text{volt} \cdot \text{sec} = [a] \cdot m^2 = \underline{\underline{\text{weber}}}$$

Types of Superconductors (cont.)



Type I — Below critical ^{field,} B_c , shielding currents at the surface prevent the field from entering the interior — hence, the material is effectively "diamagnetic"; above B_c , the material becomes normal conducting. The process is reversible.



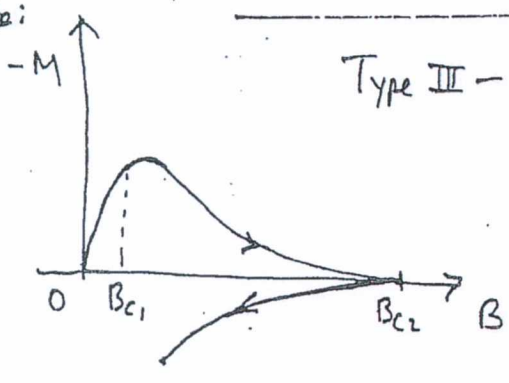
Type II — the 'diamagnetic effect' (or Meissner effect) is only present up to a value B_{c1} , the "lower critical field;" above this, the flux enters the material partially until at B_{c2} , "the upper critical field," and afterwards the material becomes normal conducting.

Table 22B1. Parameters of common superconductors. From J. File, "Superconductivity as applied to fusion reactors", Lecture 11, A Short Course in Fusion Power, Princeton University, 1972, Table 11.1, p. 11.8.

type	T_c (K)	B_{c2} (T)		J_c (GA/m ²)	
		at 4.2K	at 4.2K	at 4.2K	at 4.2K
Nb-33% Zr	10.7	8		.5 at $B = 6$ T	
Nb-48% Ti	9.5	12.2		.8 at $B = 7.5$ T	
Nb ₃ Sn	18.2	24.5		5 at $B = 10$ T	
V ₃ Ga	~15	21		4 at $B = 10$ T	
				.2 at $B = 20$ T	

In the range between B_{c1} and B_{c2} , the so-called "mixed state," the flux penetration occurs in the form of bundles, called "fluxoids," each containing one flux quantum (fluxon) $\Phi_0 = 2.07 \times 10^{-15}$ weber (or Volt.sec), and a surrounding circulating current. The process is also reversible.

Note:



Type III — In the mixed state, between B_{c1} and B_{c2} , the flux enters the material not quasi-homogeneously because the "fluxoids" will be inhibited by "pinning centers." Otherwise, this causes a hysteresis when the field is decreased again — irreversible process.

Table 4.3 Properties of some Type II superconductors

Material (Type)	T_c (K)	$\mu_0 H_{c0}$ (T)
Nb (metal)	9.5	0.2 ^a
Nb-Ti (alloy)	9.8	10.5 ^b
NbN (metalloid)	16.8	15.3 ^b
Nb ₃ Sn (intermetallic compound: A15)	18.3	24.5 ^b
Nb ₃ Al	18.7	31.0 ^b
Nb ₃ Ge	23.2	35.0 ^b
MgB ₂ (compound)	39	~15 ^a
YBa ₂ Cu _{3-x} O _x (oxide:Perovskite) <YBCO>	93	150 ^a
Bi ₂ Sr ₂ Ca _{x-1} Cu _x O _{2x+4} <BSCCO2223 or 2212>	110	108 ^a

(High temperature superconductors like YBCO will be discussed in Sect. 4.9). Courtesy of Minervini and Iwasa (2003), MIT Plasma Science and Fusion Center

^a 0 K

^b 4.2 K

Fig. 4.14 Upper critical magnetic induction versus temperature for Nb₃Sn and NbTi. Courtesy of Noe (2008), Karlsruhe Institute of Technology (KIT), Germany

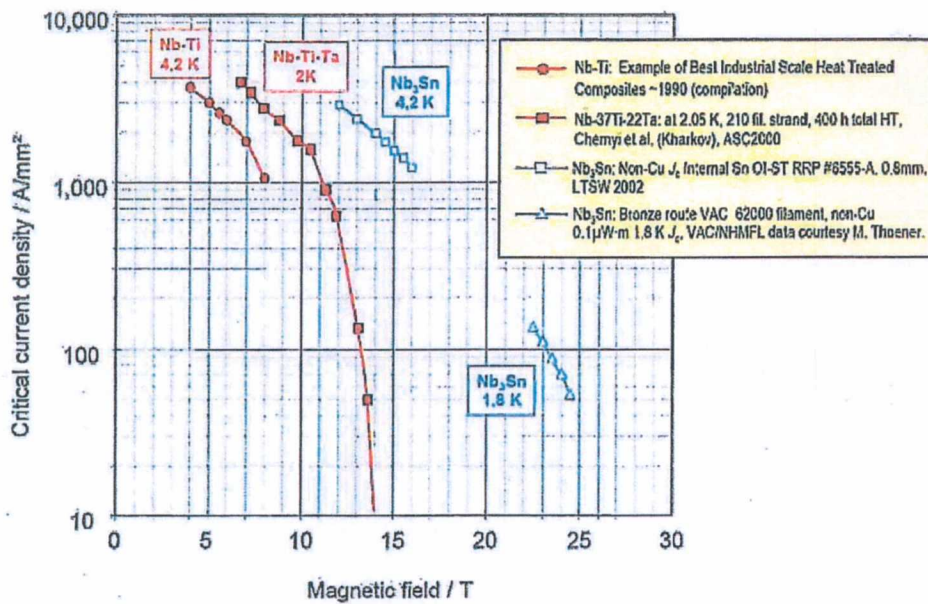
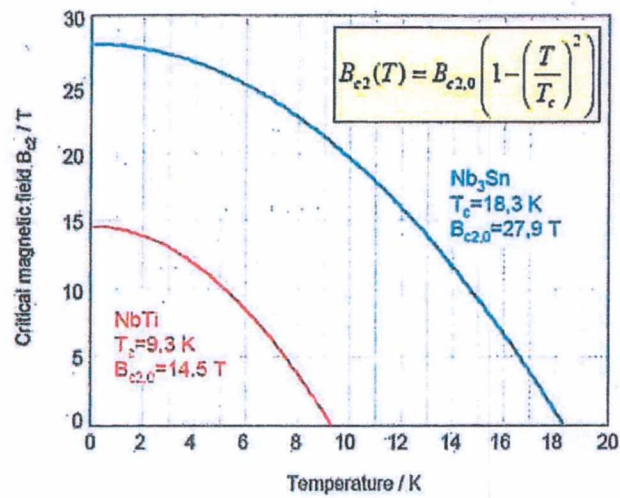
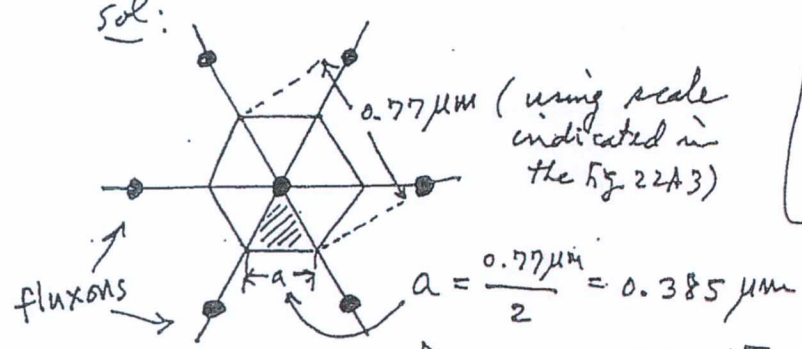


Fig. 4.15 Critical current density versus magnetic induction for Nb₃Sn and NbTi. From Courtesy of Noe (2008), Karlsruhe Institute of Technology (KIT), Germany, based on data from University of Wisconsin-Madison

Example (Prob. 22.1) [Dolan, Fusion Research, Vol. III]

Estimate the magnetic flux density B for the case of Fig. 22A3.

sol:



Note:
For a given hexagonal shape the number of enclosed fluxons is one.

Fig. 22A3 $\left[\text{area } \triangle = \left(\frac{a}{2}\right) \cdot \left(\frac{\sqrt{3}}{2} a\right) = \frac{\sqrt{3}}{4} a^2 \right] \Rightarrow \frac{\sqrt{3}}{4} \times (3.85 \times 10^{-7} \text{ m})^2 = 6.418 \times 10^{-14}$

The magnetic flux density for Fig 22A3 is given by

$$B = \frac{\# \text{ of fluxons enclosed}}{\text{area enclosed}} = \frac{\Phi_0}{A}, \text{ where } \Phi_0 \equiv \frac{h}{2e} = 2.07 \times 10^{-15} \text{ weber}$$

$$= \frac{2.07 \times 10^{-15} \text{ weber}}{6 \times \triangle \text{ m}^2} = \frac{2.07 \times 10^{-15} \text{ weber}}{6 \times 6.418 \times 10^{-14}} = \underline{\underline{5.4 \times 10^{-3} \text{ Tesla}}}$$

Prob. 22.2 [Dolan, Fusion Research, Vol. III]

Estimate the order of magnitude of coherence length, ξ , of NbTi from its B_{c2} .

sol: $B_{c2} \sim \Phi_0 / (2\xi)^2 \dots (22A19)$

[Note: NbTi is a type II superconductor]

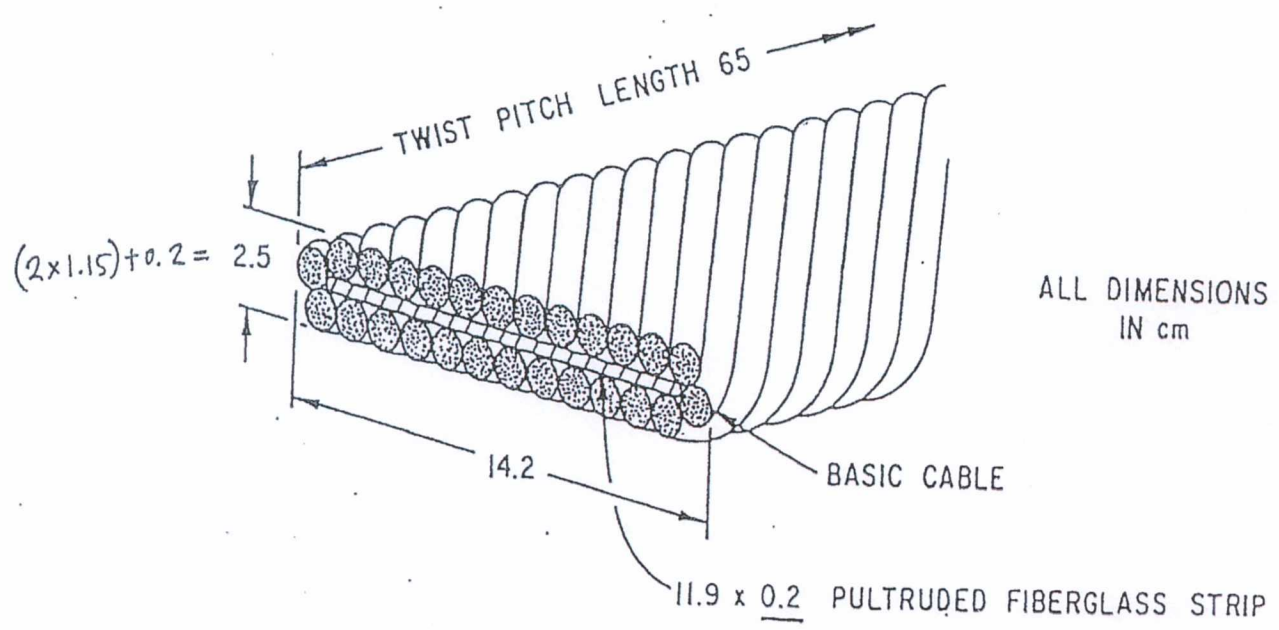
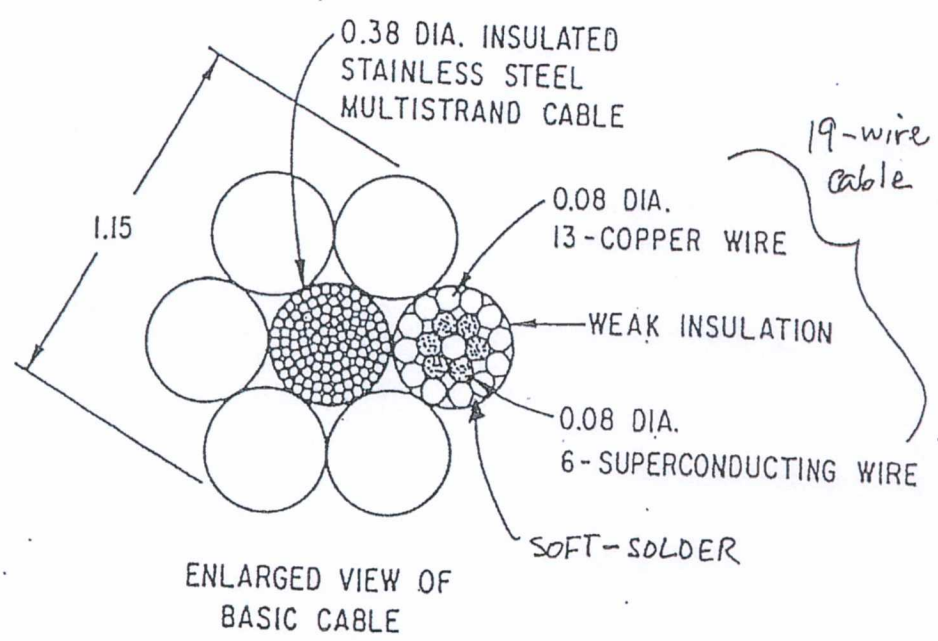
$$\therefore \xi = \frac{1}{2} \sqrt{\frac{\Phi_0}{B_{c2}}}, \text{ where } \Phi_0 \equiv \frac{h}{2e} = 2.07 \times 10^{-15} \text{ Wb.}$$

From Table 22B1, for Nb-48%Ti, $B_{c2}(T) \Big|_{4.2\text{K}} = 12.2 \text{ T}$

$$\therefore \xi = \frac{1}{2} \left[\frac{2.07 \times 10^{-15} \text{ Wb}}{12.2 \text{ T}} \right]^{1/2} = 6.51 \times 10^{-9} \text{ m}$$

$$\therefore \xi = \underline{\underline{6.51 \times 10^{-3} \mu\text{m}}}$$

4.2 Superconductors



Extra Info

Water-Cooled Coils

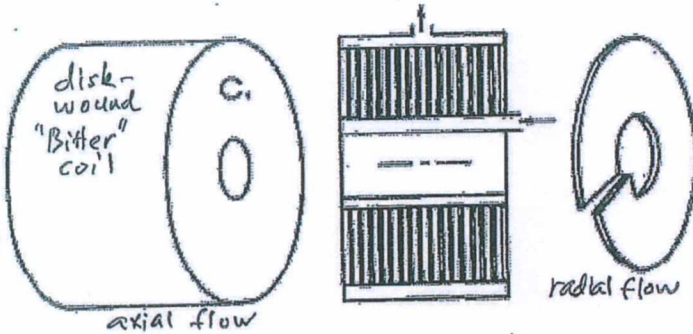
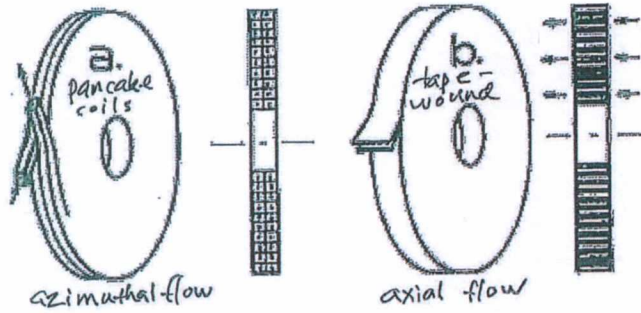


Figure 3.36 Types of coil-windings and coolant flow directions.

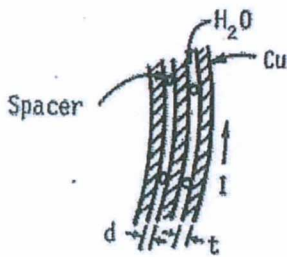


Figure 3P4. Tape-wound coil.

Superconducting Coils

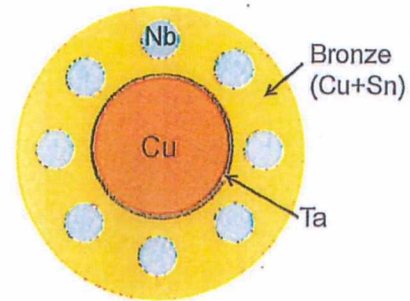


Figure 4.19. The bronze method for production of Nb₃Sn conductors.

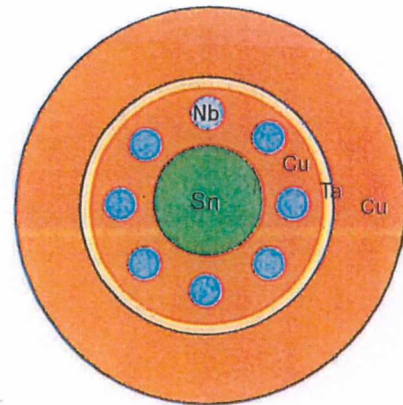


Figure 4.20 Rods of niobium surrounding a core of tin in a copper matrix for the internal tin process.

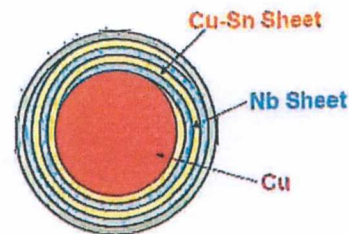
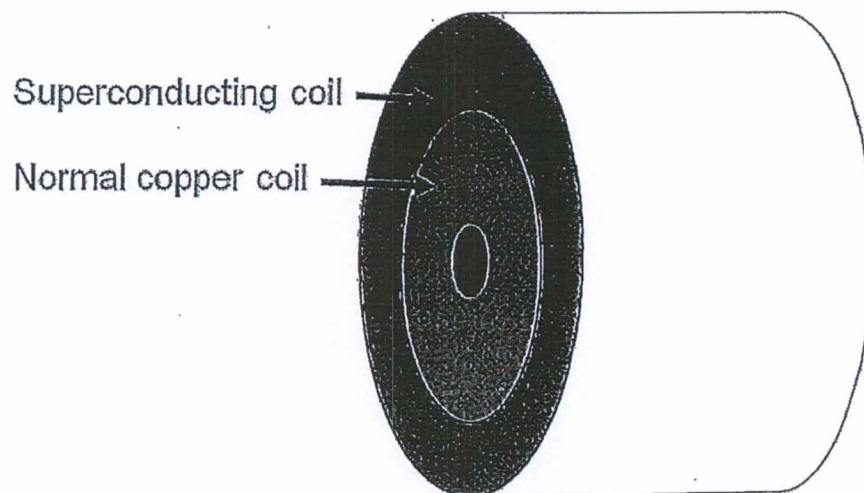
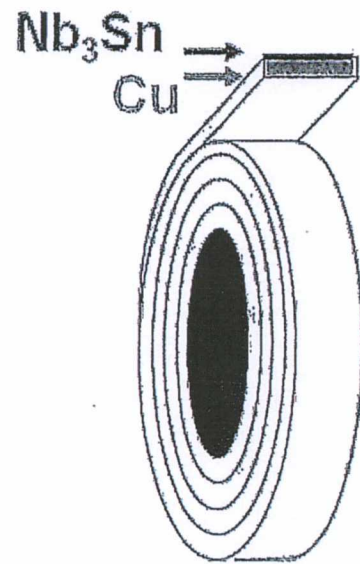


Figure 4.21 Sheets of Nb and bronze wrapped around a Cu core for extrusion in the jelly roll method.

Extra info



NbTi Superconductors

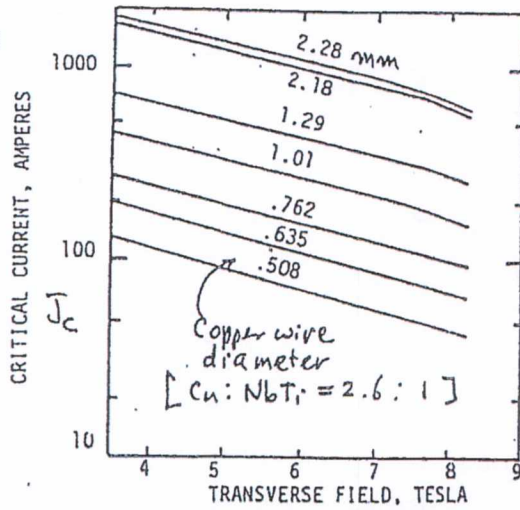
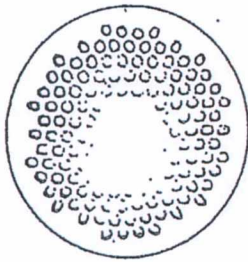


Fig. 22B1. Multifilamentary NbTi superconductors in a copper matrix (left) and critical current vs. magnetic field (right). Each wire contains 132 NbTi filaments and has a ratio of Cu:NbTi of 2.6:1. The numbers on the curves refer to the copper wire diameters (mm). Courtesy of the Magnetic Corporation of America, Haltham, MA. [Dolan, Fusion Research, Vol. III]

4.3 Stabilization

When $T > T_c$, superconductor goes to "normal",
 i.e., local R goes from 0 \rightarrow finite value instantaneously,
 and, since high I flows thru finite resistance (R),
heat is dissipated at a rate $P = I^2 R$ (watt),
 heating up the surrounding conductor, too \Rightarrow quench

\therefore Coils must be stabilized against "Quenching."

methods of stabilization

i) cryogenic stabilization:

Rule: • heat \rightarrow coolant (not to the surrounding areas):

To avoid the quench, one needs $\ll R$ (resistance)

$\alpha_s =$

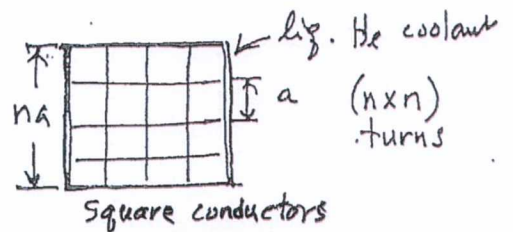
$$\frac{\text{Power dissipated}}{\text{power removed}} = \frac{I^2 \eta l / A}{g S} \leq 1 \quad \dots \begin{matrix} (4.21) \\ (22(1)) \end{matrix}$$

Steady
numbers

where

$\eta =$ resistivity of the conductor ($\Omega \cdot m$)
 $A =$ X-sectional area of conductor (m^2)
 $l =$ length under consideration
 $S =$ conductor surface area in contact with the He-coolant (m^2)
 $g =$ maximum heat flux (which coolant can remove) (W/m^2)
 (e.g. $g|_{\text{liq He}} \approx 4000 \text{ W/m}^2 = 0.4 \text{ W/cm}^2$)

Note: Prob. 22.3 for α_s estimate.
 [Dolan, Fusion Research, Vol. III]



ANS. Prob. 22.3:

$$\alpha_s = \frac{I^2 \eta l / A}{q S} \quad \left| \begin{array}{l} A = a^2 \\ S = 4al \\ \text{(per conductor} \\ \text{channel)} \end{array} \right. \xrightarrow{\substack{\text{for} \\ \text{the bundle} \\ \text{of } n \times n \\ \text{conductors}}} \left(\frac{n I^2 \eta l / a^2}{q \cdot 4n a l} \right) \quad \left| \begin{array}{l} A = a^2 \\ S = 4n a l \end{array} \right.$$

$$= \frac{n I^2 \eta}{4 a^3 q}$$

In order to achieve cryogenic stabilization, $\alpha_s \leq 1$;

$$n = \frac{4 a^3 q \cdot (1)}{I^2 \eta} = \frac{4 (0.1 \text{ cm})^3 \cdot (0.4 \text{ W/cm}^2) \cdot (1)}{(50 \text{ A})^2 \cdot (3 \times 10^{-8} \Omega \cdot \text{cm})} = 21.3$$

$\therefore \underline{\underline{n_{\max} = 21 \text{ turns}}}$ (to maintain cryogenic stabilization)

ii) Adiabatic stabilization: *

Rule: a) Use thin superconductor filament so that the heat dissipated by a flux jump is too small to raise T_c temp. above

Stability criterion (for circular filament) is then

$$d \cdot J_s < \pi \left(\frac{\rho_m C_p T_0}{\mu_0} \right)^{1/2}, \quad \dots \quad \left(\frac{22 \text{ C 2}}{4.22} \right) \quad \left[\vec{V} \times \vec{B} = \mu_0 \vec{J} \right]$$

line current density

where d = filament diameter (m)
 J_s = current density in the filament (A/m^2)
 ρ_m = density (kg/m^3)
 C_p = specific heat ($\text{J/(kg} \cdot \text{K)}$) } of the filament

and $T_0 = \frac{-J_s}{\left(\frac{\partial J_s}{\partial T} \right)_{B=\text{const}}}$

[e.g. $\rho_m C_p \sim 1000 \text{ J/(m}^3 \cdot \text{K)}$ for NbTi and Nb_3Sn
 and $T_0 = 10^4 \text{ K}$,
 if $d = 10 \mu\text{m}$ (typical diameters),
 and $T_0 = 10^4 \text{ K}$,

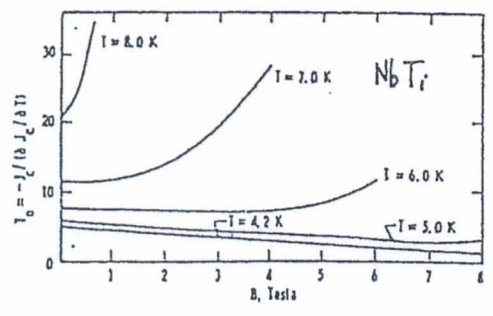
$$J_s \lesssim \frac{\pi}{d} \left(\frac{\rho_m C_p T_0}{\mu_0} \right)^{1/2}$$

$$= \frac{\pi}{10 \times 10^{-6} \text{ m}} \sqrt{\frac{1000 \text{ J/(m}^3 \cdot \text{K}) \times 10^4 \text{ K}}{4\pi \times 10^{-7} \text{ W/Amp} \cdot \text{m}}}$$

$$\approx 2.8 \times 10^{10} \text{ Amp/m}^2$$

$$\lesssim (10^{-6} \text{ m}) \cdot (2.8 \times 10^{10} \text{ Amp/m}^2)$$

$$= 2.8 \times 10^4 \text{ amp/m}$$



< adiabatic stability parameters >

(maximum line density) $\Rightarrow d \cdot J_s$

"Superconductivity in Technology,"
 * P. Komarek, Contemp. Phys., 17, pp. 355-386 (1976).
 P.N. Haubenreich, et al., Cryogenics (1989).

ii) Adiabatic stabilization (cont'd)

Rule: b) Twist the ^{thin} filaments to prevent current loops from being induced between adjacent filaments:

∴ The "critical length" that the filaments must be twisted l_c is;

$$\vec{\nabla} \times \vec{E} = -\frac{\partial \vec{B}}{\partial t}$$

$$E_y(z) = z \dot{B}_x \quad [E = \eta J]$$

line current density

$$J_y(z) = \frac{1}{\eta} \int_0^{l_c} E_y(z) dz$$

$$d \cdot J_s = \frac{1}{\eta} \dot{B}_x \frac{1}{2} l_c^2$$

$$l_c = \left[\frac{2 J_s \cdot d \cdot \eta}{\left(\frac{dB}{dt}\right)} \right]^{1/2} \text{ (m)}$$

where η = resistivity ($\Omega \cdot m$)

$\frac{dB}{dt}$ = time rate of change of \vec{B} (T/sec)

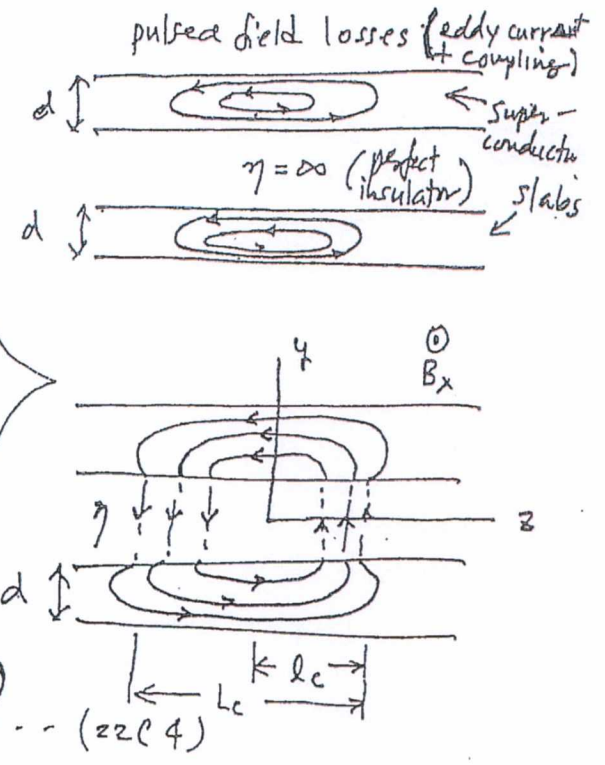
Thus, a pulsed coil must have a short transposition length
 [Note: Epoxy could also be used to prevent conductor motion.]

e.g. $J_s = 9 \times 10^9 \text{ A/m}^2$
 $d = 10 \mu\text{m} = 10 \times 10^{-6} \text{ m}$
 $\eta = 10^{-10} \Omega \cdot m$
 $B = 5 \text{ T/sec}$

$$\frac{l_c}{2} = \left[2 \times (9 \times 10^9 \frac{\text{A}}{\text{m}^2}) \cdot (10 \times 10^{-6} \text{ m}) \times (10^{-10} \Omega \cdot m) / 5 \text{ T/sec} \right]^{1/2}$$

∴ $l_c \approx 4 \text{ mm}$

length to reach critical current is rather short.



iii) Dynamic stabilization

utilize "magnetic damping" of flux jumps to reduce the heat generated, combined w/ heat removal by conduction. [Mostly used for Nb₃Sn or V₃Ga tapes.]

a) Condition I :

$$H_{\perp} \left(\frac{\text{amp}}{\text{m}} \right) < \pi \sqrt{\frac{K_{Cu} T_0}{4\eta}}$$

↑
mag. fld. \perp to
the superconductor ribbon
(in the radial direction)

K_{Cu} : thermal conductivity of copper (W/m²·K)

η : resistivity of element ($\approx 3 \times 10^{-10} \Omega \cdot \text{m}$ for Cu)

b) Condition II :

$$J_s < \left[\pi T_0 \frac{d_n K_s}{\eta d_s^3} \right]^{1/2} \left(\frac{\text{Amp}}{\text{m}^2} \right)$$

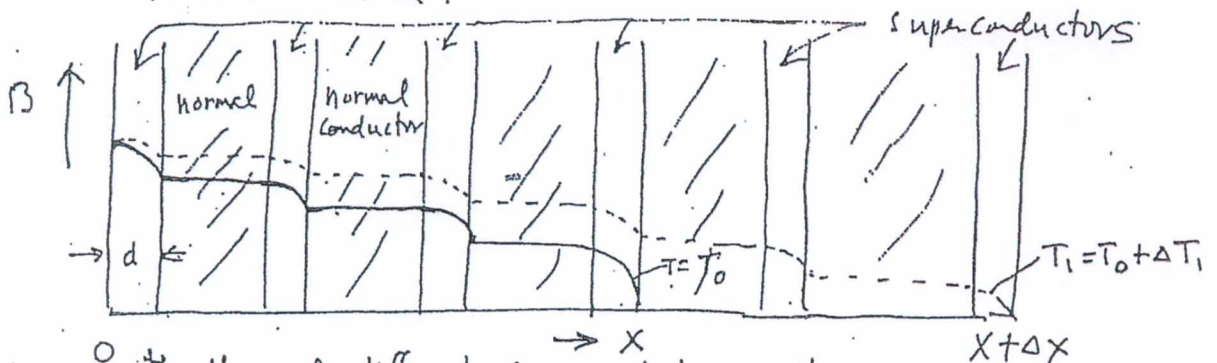
↑
current density in superconductor

K_s : ther. conductivity of superconductor (W/m²·K)

d_n } : thickness of normal conductor & superconductor ribbons

d_s }

∴ Rule : Embed the fine superconducting filaments into a normal conducting matrix and provide good electric and thermal bond.



Note: In the matrix, the thermal diffusivity is much larger than the magnetic one, and the damping of the flux over the whole system provides the transport of heat dissipated along the normal-conducting areas to cooled surfaces.

4.4 Coil Protection

19

Fault Conditions against:

i) quench - Typical fusion reactor coil has energies \sim GJ per coil stored.

When it quench, $\sim 140^\circ\text{K}$ ^{coil} temp. rise results
 don't want to dissipate in a small region of coil

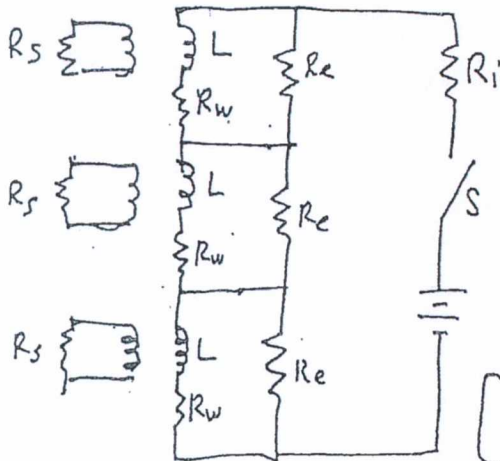
ii) broken circuits - resulting arcs w/ $\sim 100\text{V}$ result

This could puncture a thin steel coil case, destroying vacuum

iii) short circuit to ground - this will limit current to $\sim 10\text{A}$: wouldn't cause too much damage

iv) coolant channel blockage - Under magnet "normal" condition, heat removal is inadequate could prevent recovery of superconductivity.

Note: use protection circuitry:



L = coil inductance

R_s = resistance of coil support structure

R_w = coil winding resistance $\Rightarrow 0$ during normal operation

R_e = external energy dump resistance

R_i = resistance of coil leads & power supply

e.g. If $I_{coil} = 10\text{kA}$ and $R_e = 0.1\ \Omega$, $V = 1000\text{Volts}$ (across insulation)
 If $L = 30\text{H}$, $\tau = \frac{L}{R_e} = \frac{30}{0.1} = 300\text{ sec}$ (for current decay)

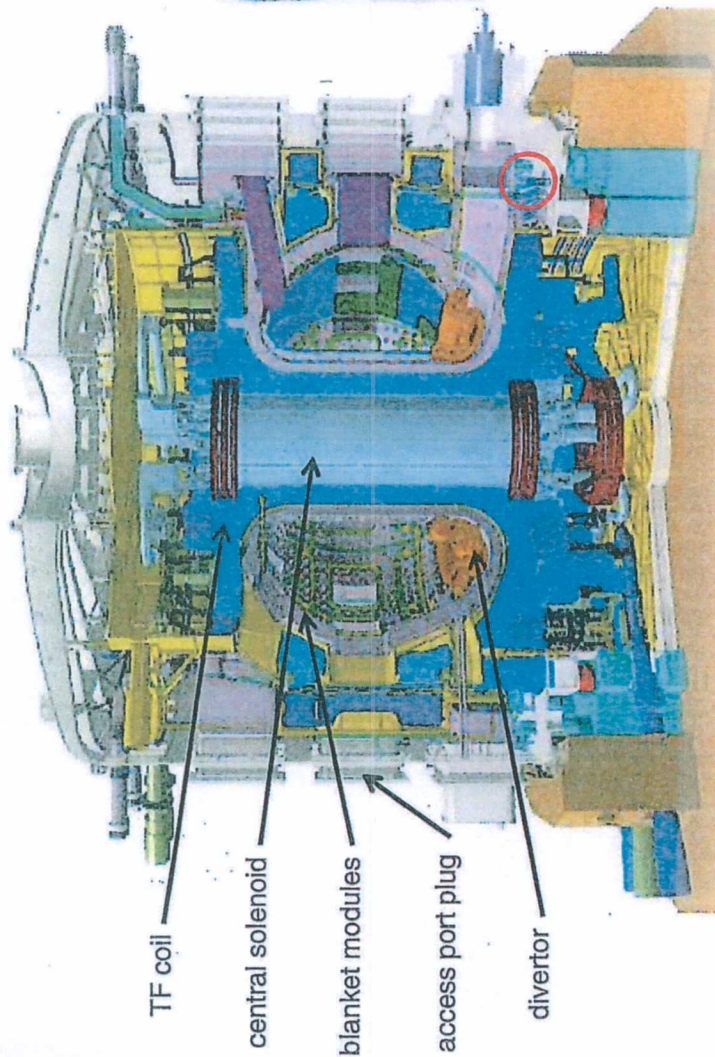


Fig. 1.33 Main components of ITER. A person is shown for scale (in red circle).
Courtesy of ITER Organization

	Ignition 1998	"High-Q" 2005
∞ (Ignition)		10
1,500		400
1,000		400
8.1/2.8		6.2/2.0
21		15
5.7		5.3
20		18 → ripple problem

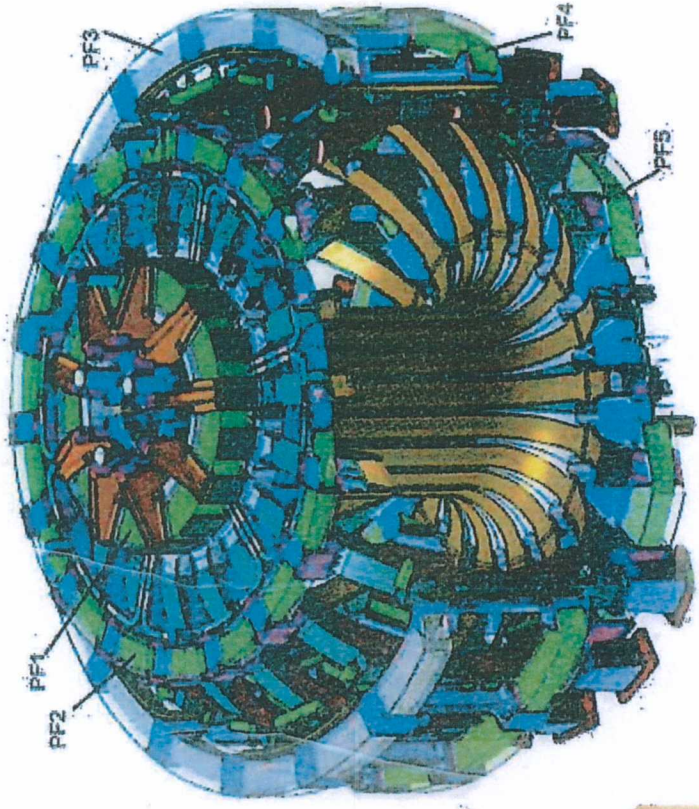


Fig. 4.22 The ITER coil system, showing TF coils (brown), circular PF coils (thick grey and green), and CS coils (blue). The thin green segments represent part of the Correction coils. Courtesy of ITER Organization

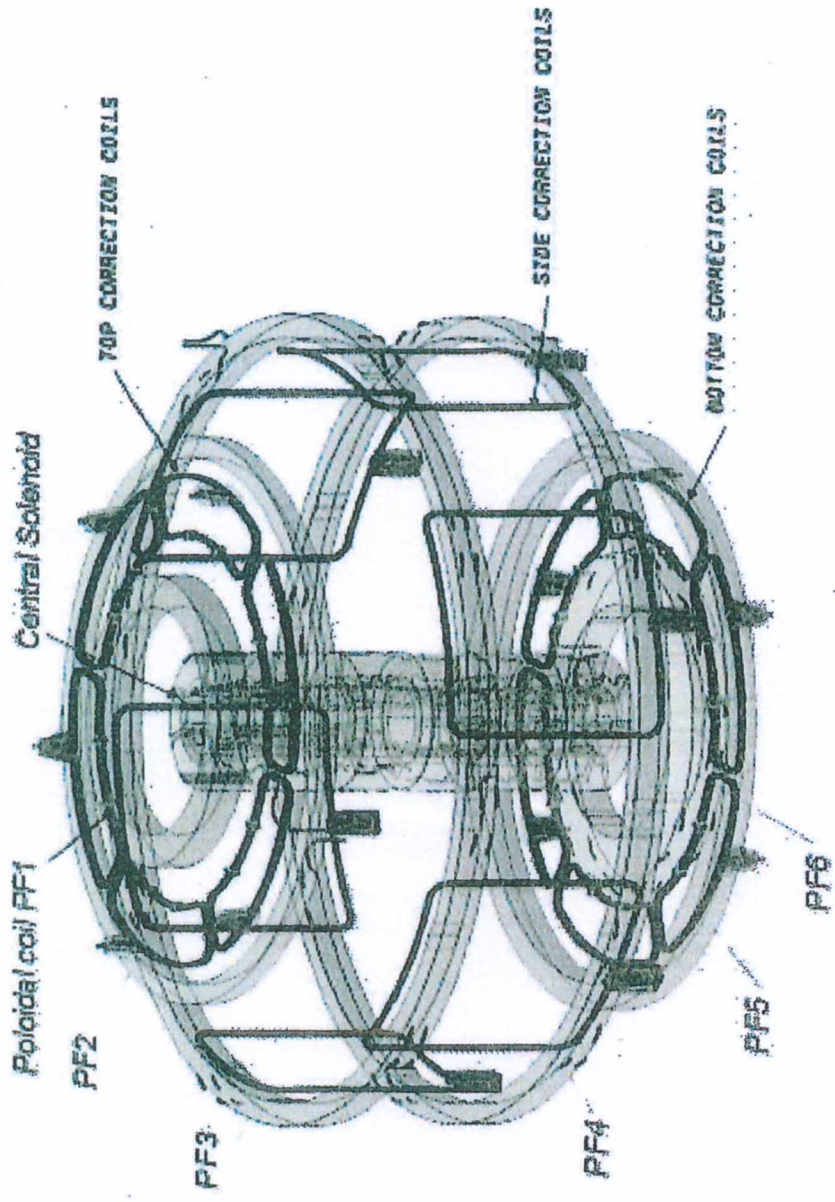


Fig. 1. Layout of correction coils system.

Table 4.8 ITER coil sets

System	Energy (GJ)	Peak field (T)	Cond. length (km)	Total weight (t)
Toroidal field (TE)	41	11.8	82.2	6,540
Central solenoid (CS)	6.4	13.0	35.6	974
Poloidal field (PF)	4	6.0	61.4	2,163
Correction coils(CC)	-	4.2	8.2	85

PAPER

Challenges and status of ITER conductor production

To cite this article: A Devred *et al* 2014 *Supercond. Sci. Technol.* **27** 044001

View the [article online](#) for updates and enhancements.

Related content

- [Performance analysis of the toroidal field ITER production conductors](#)
M Breschi, D Macioce and A Devred
- [Cable-in-conduit conductors: lessons from the recent past for future developments with low and high temperature superconductors](#)
L Muzzi, G De Marzi, A Di Zenobio *et al.*
- [Performance analysis of the NbTi conductor qualification samples for the ITER project](#)
M Breschi, D Carati, D Bessette *et al.*

Recent citations

- [Doping-Induced Isotopic Mg11B2 Bulk Superconductor for Fusion Application](#)
Qi Cai *et al*
- [DTT device: Conceptual design of the superconducting magnet system](#)
A. Di Zenobio *et al*
- [Design, Manufacture, and Test of an 80 kA-Class Nb3Sn Cable-In-Conduit Conductor With Rectangular Geometry and Distributed Pressure Relief Channels](#)
Luigi Muzzi *et al*



 **can**
superconductors

www.can-superconductors.com

HTS PARTS AND MATERIALS

Single and Multi-domain YBCO Bulk
REBCO Sputtering Targets
REBCO Powders and Granulates
BSCCO Current Leads, Magnetic Shields
Superconductivity Demonstration Kits

Challenges and status of ITER conductor production

A Devred, I Backbier, D Bessette, G Bevilard, M Gardner, C Jong, F Lillaz, N Mitchell, G Romano and A Vostner

Magnet Division, ITER International Organization, Route de Vinon-sur-Verdon, F-13067 Saint-Paul-Lez-Durance, France

Received 29 October 2013, revised 2 January 2014

Accepted for publication 9 January 2014

Published 18 March 2014

Abstract

Taking the relay of the large Hadron collider (LHC) at CERN, ITER has become the largest project in applied superconductivity. In addition to its technical complexity, ITER is also a management challenge as it relies on an unprecedented collaboration of seven partners, representing more than half of the world population, who provide 90% of the components as in-kind contributions. The ITER magnet system is one of the most sophisticated superconducting magnet systems ever designed, with an enormous stored energy of 51 GJ. It involves six of the ITER partners. The coils are wound from cable-in-conduit conductors (CICCs) made up of superconducting and copper strands assembled into a multistage cable, inserted into a conduit of butt-welded austenitic steel tubes. The conductors for the toroidal field (TF) and central solenoid (CS) coils require about 600 t of Nb₃Sn strands while the poloidal field (PF) and correction coil (CC) and busbar conductors need around 275 t of Nb–Ti strands. The required amount of Nb₃Sn strands far exceeds pre-existing industrial capacity and has called for a significant worldwide production scale up. The TF conductors are the first ITER components to be mass produced and are more than 50% complete. During its life time, the CS coil will have to sustain several tens of thousands of electromagnetic (EM) cycles to high current and field conditions, way beyond anything a large Nb₃Sn coil has ever experienced. Following a comprehensive R&D program, a technical solution has been found for the CS conductor, which ensures stable performance versus EM and thermal cycling. Productions of PF, CC and busbar conductors are also underway. After an introduction to the ITER project and magnet system, we describe the ITER conductor procurements and the quality assurance/quality control programs that have been implemented to ensure production uniformity across numerous suppliers. Then, we provide examples of technical challenges that have been encountered and we present the status of ITER conductor production worldwide.

Keywords: ITER, cable-in-conduit conductor, Nb₃Sn, Nb–Ti, strain sensitivity

(Some figures may appear in colour only in the online journal)

1. ITER project

The main goal of the ITER project is to demonstrate the scientific and technological feasibility of fusion power [1, 2]. This includes in particular: (1) the achievement of extended burn of deuterium–tritium plasmas, with steady state as the ultimate goal, (2) the integration and test of all critical fusion power reactor technologies and components, including the sophisticated magnet system at the heart of the machine, and (3) the demonstration of the safety and environmental acceptability of nuclear fusion.

ITER is also an unprecedented political and management challenge. It was born in 1985 at a superpower summit meeting in Geneva between R Reagan and M Gorbachev. It is now supported by seven members: China (CN), Europe (EU), India (IN), Korea (KO), Japan (JA), the Russian Federation (RF) and the United States (US), representing more than half of the world's population. The seven ITER members have agreed a procurement allocation, based on an overall agreed procurement value for the project's construction phase, of which EU, who is the host, contributes 5/11th while

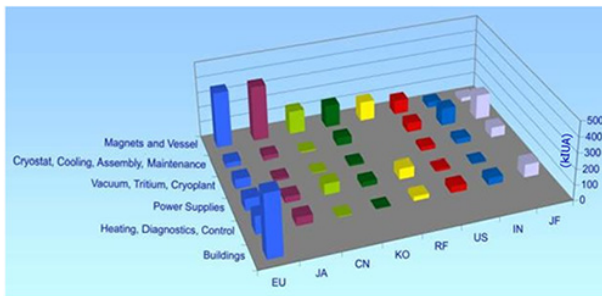


Figure 1. Procurement allocation among ITER partners: EU (Europe), JA (Japan), CN (China), KO (Korea), US (United States), IN (India) and JF (Joint Funds). The contributions are expressed in ITER Units of Account (IUA), a currency devised in 1989 to measure the value of in-kind contributions consistently over time while neutralizing market fluctuations. In 1989, 1 IUA = 1000 US\$; in 2013, 1 IUA = 1660.15€.

each of the other members contributes 1/11th. The bulk of the contributions, in terms of technologies and industrial production, is to be delivered in kind—about 90% of the overall value, while the remaining 10% will be in cash contributions, also referred to as joint funds (JF). The breakdown of who contributes what is at the component level and is cast in the so-called ITER Agreement. Figure 1 illustrates this task sharing. All members except India contribute to the magnet system.

The project is managed by the International Organization (IO) and the seven members have set up Domestic Agencies (DAs) to handle their contributions. The IO is responsible for overall design and integration, defines the technical requirements and issues Procurement Arrangements (PAs) with the DAs. The DAs carry out calls for tender (following domestic rules), procure the components and deliver them to the IO within the PA framework.

The ITER site was selected in 2005 near Saint-Paul-Lez-Durance in the South of France. As part of a special contribution to the project, France has completed massive roadwork for transportation of large components from Marseille harbor about 104 km away. Civil engineering has been underway on the ITER platform since 2010 and the French Government authorized the nuclear installation creation in November 2012. As illustrated in figure 2, which shows recent pictures of the ITER site, two buildings have been completed: the large (252 m × 45 m × 17 m) building to be used for the on-site manufacturing of the poloidal field (PF) coils and the headquarter building. The excavation of the tokamak pit (120 m × 90 m × 17 m) and the foundation of the tokamak building, which include 493 m × 1.8 m high seismic pads covered by a 1.5-m-thick basemat, have also been completed.

2. ITER tokamak and magnet system

ITER relies on the tokamak concept first proposed by I Y Tamm and A Sakharov in the 1950s. The main components of the ITER tokamak are [3]

- the vacuum vessel (which delimits the plasma chamber),
- the magnet system (which controls plasma confinement, shaping and stability),

- the cryostat (which shields the vacuum vessel and the magnet system),
- the blankets and divertor (which absorb neutron flux and eliminate plasma ashes).

As illustrated in figure 3, the tokamak cryostat is 28 m tall and 29 m in diameter, which corresponds more or less to the size of the Jefferson memorial in Washington DC.

The ITER magnet system is fully superconducting and includes four different types of coils (see figure 4) [4]

- 18 toroidal field (TF) coils, located around the plasma chamber, to be manufactured in EU [5] and Japan [6],
- a central solenoid (CS), made up of a stack of six modules and positioned at the machine centre, to be manufactured in the US [7],
- six poloidal field (PF) coils, surrounding the TF coils, whose manufacture is the responsibility of RF (for PF1) and EU (for PF2 to 6) [8],
- nine pairs of correction coils (CC) attached to the PF coils and manufactured in CN [9].

The ITER magnets are supplied with current and cryogenic fluids by means of 31 feeders. The feeders count more than 600 000 parts and are deeply embedded inside the tokamak with many interfaces [10]. They include two types of superconducting busbars: the Main Busbars (MB), supplying the TF, CS and PF coils and the Correction coil Busbars (CB) supplying the CCs. They also include 60 current leads of various types. The initial designs called for copper leads, but following the successful manufacture and test of a 68 kA demonstrator at KIT in 2004 [11, 12], a decision was made to change to high temperature superconductor (HTS) leads. The present ITER HTS lead designs [13] rely on BSCCO 2223/Ag–Au tapes, with a fin-type heat exchanger extrapolated from the HTS lead designs developed by CERN for the large Hadron collider (LHC) [14]. The feeders, busbar conductors and HTS leads are built-to-print packages procured in kind by China.

The ITER magnet system is the largest and most integrated superconducting magnet system ever built. Its stored magnetic energy is 51 GJ. As a comparison, the second largest superconducting magnet system is the Large Hadron Collider machine at CERN, which has a stored magnetic energy of ~11 GJ distributed over a magnet ring of 27 km in circumference [15]. In case of a quench, the ITER magnet system is expected to be discharged in about 10 s. Of course, this raises tremendous challenges for magnet protection and for the quench detection systems which have to be operated in a very noisy electromagnetic environment, with enough sensitivity to discriminate between resistive voltage increases in the coils and false triggers due to plasma disruptions [16].

3. ITER conductors

3.1. Overview

ITER magnets rely on cable-in-conduit conductors (CICCs), a concept developed in the mid 1970s by Hoenig [17]. As illustrated in figure 5, the main features of the ITER CICCs are [18]:



Figure 2. Recent views from the ITER construction site, near Saint-Paul-Lez-Durance, France.

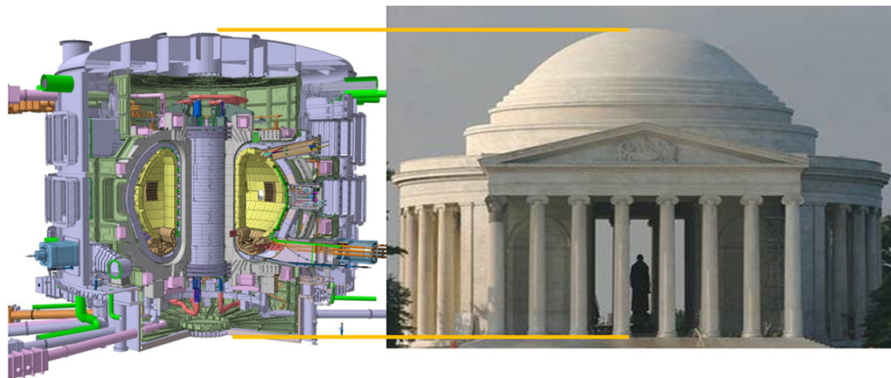


Figure 3. Artist view of the ITER tokamak (~28 m tall x 29 m in diameter) in comparison to the Jefferson Memorial in Washington DC (29 m tall; courtesy of G Johnson).

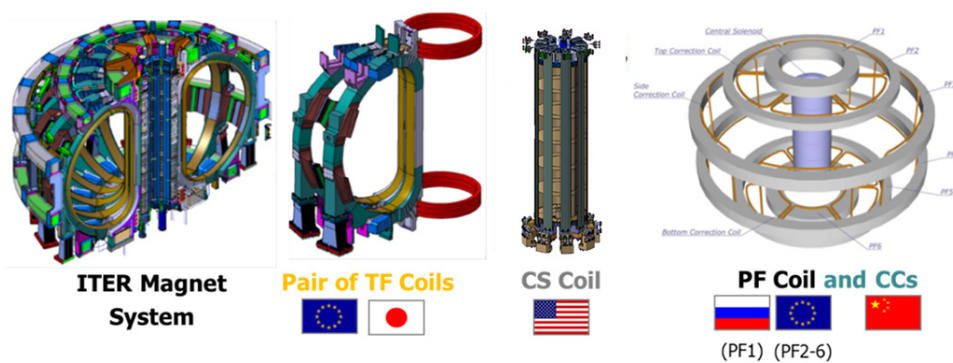


Figure 4. Artist views of the ITER magnet system and of the different coils that make it up: TF (toroidal field), CS (central solenoid), PF (poloidal field) and CC (correction coils).



Figure 5. Views of the ITER TF conductors and of its components (courtesy of P Lee and C Sanabria, Florida State University).

- Cr-plated Nb₃Sn or Ni-plated Nb–Ti superconducting (sc) strands mixed with segregated Cr-plated or Ni-plated Cu strands,
- a multi-stage cable with stainless steel cable/sub-cable wraps and a central cooling spiral (save for CC and MB conductors),
- a circular, square or circle-in-square, austenitic stainless steel conduit made up of butt-welded jacket sections.

The TF and CS conductors both rely on Cr-plated Nb₃Sn strands, while the PF, CC, MB and CB conductors rely on Ni-plated Nb–Ti strands [18]. The TF, MB and CB conductors have a circular jacket, the CS and PF conductors have a circle-in-square jacket, while the CC conductor is square. TF conductors are manufactured by six DAs: CN [19, 20], EU [21], JA [22], KO [23], RF [24] and US. CS conductors are the responsibility of JA but are funded by the EU as part of the Broader Approach agreement negotiated between Japan and Europe at the time of site selection [25]. Conductors for PF1 and PF6 coils are manufactured by RF and EU, which have signed a bilateral agreement upon which RF takes care of strand production and cabling and EU takes care of the rest of conductor production [21, 24]. CC [26], MB and CB [27] conductors are the responsibility of CN. Salient Parameters of ITER conductors are summarized in tables A.1, A.2, A.3 and A.4 in the appendix. A typical TF Conductor Unit Length is ~760 m and requires a minimum of 3.3 t of Nb₃Sn strands and 1.6 t of stainless steel tubes. A typical CS conductor unit length is ~900 m and requires a minimum of 2.6 t of Nb₃Sn strands and 11.3 t of stainless steel tubes. In the case of TF, the cost of the jacket is less than 10% of the cost of the strands, but for CS, it may be 50% or more. Let us note that the TF conductor package is one of a few that involves so many DAs.

3.2. Manufacture

Figure 6 details the main steps of conductor manufacture. It starts with strand production, relying on conventional extrusion and drawing techniques. The rope-type cables are manufactured in five stages (save for CC which has only

four) on dedicated machines designed to apply full back twist. The first cable stage is a triplet, usually made up of two superconducting strands and one copper strand, while the last stage is cabled on a planetary machine. The base material for the jacket is high purity austenitic steel and the jacket sections are produced by hot extrusion followed by cold drawing and/or pilgering steps and are carefully inspected by non-destructive examination (NDE) techniques. The jacket sections are butt-welded together to form a jacket assembly with a length corresponding to the final length of the conductor (up to 760 m for the TF conductors and 920 m for the CS conductors). Each orbital weld is inspected by x-rays and is subjected to a local helium leak check and a dye penetrant test. The inner diameter of the jacket assembly is a few millimetres larger than the cable outer diameter to enable its insertion by means of a pulling rope. Once the cable is inserted, the jacket is compacted to achieve final dimension and the compacted conductor is spooled over a diameter of ~4 m to facilitate transportation. The spooled conductor is subjected to a number of final acceptance tests, including a global helium leak test and another set of dye penetrant tests of every butt-weld.

For TF, which calls for an estimated amount of 480 t of Nb₃Sn strands, eight strand suppliers are involved: four rely on the bronze process and four rely on the internal tin (IT) process. For CS, so far, contracts have only been awarded for four modules: three will rely on bronze process strands and one will rely on IT strands. Regarding Nb–Ti strands, two strand types are needed, one with a copper-to-non-copper ratio of 1.6–1 for the PF1&6 conductors (referred to as strand type 1) and one with a copper-to-non-copper ratio of 2.3–2 for all the other Nb–Ti conductors (PF2–5, CC, MB and CB; referred to as strand type 2). ChMP in RF has been selected for the production of strand type 1, while WST in China has been selected for the production of strand type 2. Figure 7 shows the distribution of strand suppliers, thereby confirming the international nature of the project. It should be noted that three of these suppliers (ChMP in RF [28], KAT in KO [29] and WST [30, 31] in CN) are new to the business and have been set up by their government to fulfil the ITER needs, while the six others (BEAS in EU [32], Furukawa, Hitachi [33, 35]

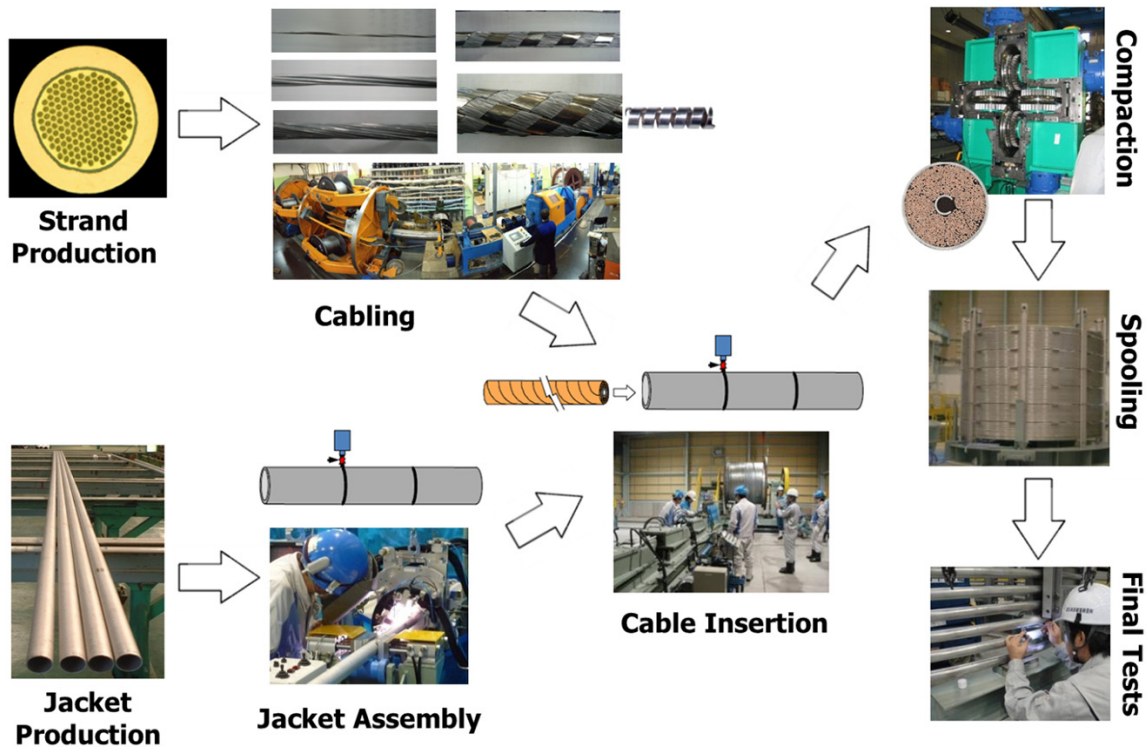


Figure 6. Main steps of ITER CICC manufacture (photos courtesy of D Kaverin, VNIKP and Y Nunoya, JAEA).

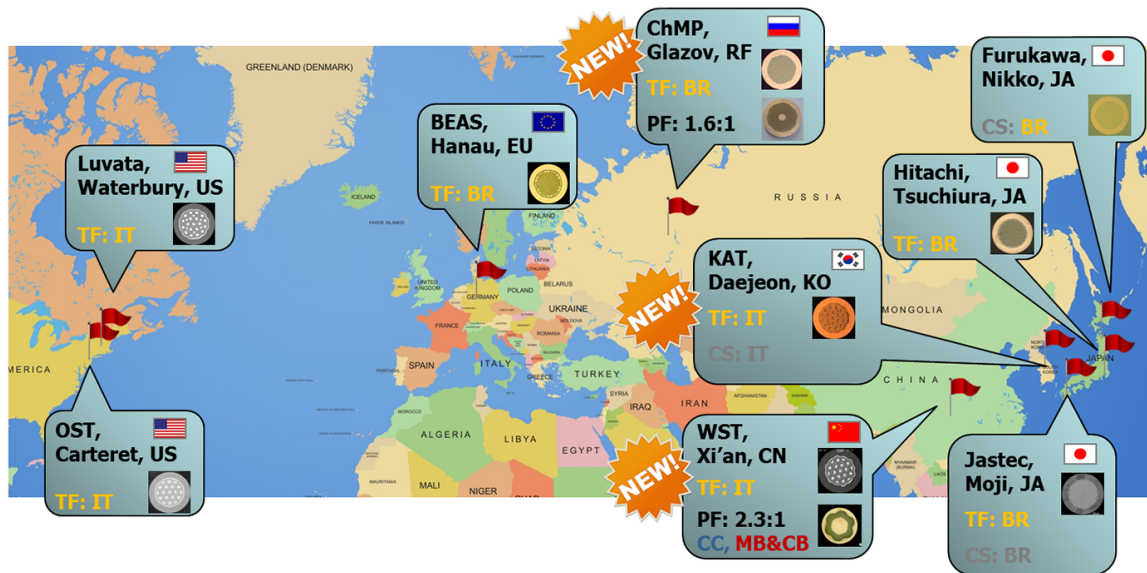


Figure 7. ITER strand suppliers around the world: a truly international collaboration. TF Nb₃Sn strands involve four bronze (BR) suppliers (BEAS, ChMP, Hitachi and Jastec) and four IT suppliers (KAT, Luvata, OST and WST). Nb–Ti strand type 1 is produced by ChMP, while Nb–Ti strand type 2 is produced by WST. Contacts for four CS modules have been awarded: two for Jastec (BR), one for Furukawa (BR) and one for KAT (IT).

and Jastec [34, 35] in Japan, and Luvata [36] and OST [37, 38] in the USA) are well established superconducting strand suppliers.

One particularity of ITER conductor manufacture is that it requires dedicated 800–1000 m long jacketing lines to store the welded jacket assemblies and to carry out cable insertion prior to compaction and spooling. The feasibility of the jacketing

concept for long length CICC was first demonstrated in the mid 1990s in RF [39].

Five out of the six DAs involved in ITER conductor production have decided to set up their own jacketing line (namely: CN, EU, JA, RF and US), whereas KO has decided to subcontract its jacketing work to the EU supplier. Figure 8 shows pictures of the five jacketing lines. The one in Japan

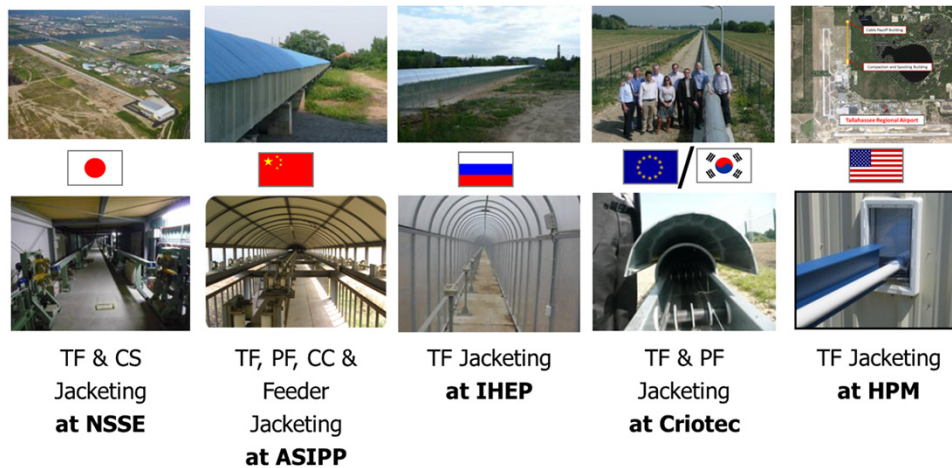


Figure 8. ITER jacketing lines around the world.

(located at NSSE in Kita-Kyushu) is rather spacious and one can cycle along it [40]. The one in China (located at ASIPP in Hefei), is more shallow and would require crawling. The one in Russia (located at IHEP in Protvino) is of the greenhouse type [24]. The one in Europe (used for both EU and KO productions and located at Criotec near Chivasso, Italy) is quite compact [41]. The one in the US (located at HPM in Tallahassee, Florida) is the most particular as it runs parallel to the Tallahassee airport runway. All the lines except the European one were set up and operated for ITER. The European line was initially used for jacketing of the conductors of the series-connected hybrid magnets being built by the National High Magnetic Field Laboratory in Tallahassee [42] and has subsequently been used for ITER and for JT60 super upgrade conductor productions [41].

3.3. Quality assurance/quality control and ITER conductor database

Given the large number of partners involved, it is critical to ensure standardization and uniformity of conductor production around the world. To do so, the 11 conductor PAs define detailed quality assurance (QA) and quality control (QC) requirements to be implemented by the DAs and their suppliers. Among others, these QA/QC requirements call for

- qualification and certification of manufacturing and test procedures (e.g., orbital welding of jacket sections, local and global He leak tests),
- statistical process control (SPC) on critical parameters,
- benchmarking of cryogenic test facilities,
- systematic low-temperature measurements on strands (critical current, hysteresis loss, residual resistivity ratio): head/tail of every billet + statistical sampling of breakages,
- regular low-temperature measurements on full-size conductors: 25% of TF conductor unit lengths (ULs), 10% of PF conductor ULs, 25% of CS conductor ULs.

To ensure consistency of strand measurements and of the corresponding acceptance criteria, ITER-IO organized several rounds of benchmarking of Nb₃Sn and Nb–Ti strand test facilities of all interested parties (suppliers, DA and ITER-IO reference laboratories) [32, 43]. For strand benchmarking, ITER-IO selected CERN as its reference laboratory [44, 45]. As part of its scope of work, CERN was asked to derive a $J_C(B, T, \varepsilon)$ parameterization for ITER Nb₃Sn strands that is now used by all ITER partners [44].

In addition, as illustrated in figure 9, the PAs define a number of control points where the suppliers and the DAs must seek clearance before proceeding to the next step. In total there are seven control points: five authorizations to proceed (strand lot, cable map, cable, jacket section lot, and jacket assembly), one notification point (jacketing) and one hold point (final conductor). A strand lot is defined as all the strand unit lengths issued from the same multifilament billet, while a jacket section lot is defined as all the jacket sections issued from a same mother heat and ESR that have been processed at the same time down to the last solution annealing treatment.

The monitoring of the PA execution is ensured by means of a web-based conductor database, developed by the IO and used by the DAs and their suppliers worldwide [46]. The implementation of the conductor dataset, which ensures strict confidentiality of the DAs and individual supplier data has been quite successful. Presently, there are ~20 suppliers/DAs and ~150 users registered to input and verify data. Over the course of the last four years, the IO has cleared ~6900 control points, which, for the strand lots, rely on ~27 000 critical current measurements.

3.4. Full-size conductor tests at SULTAN

The most difficult and critical acceptance tests are the full-size conductor tests which are carried out at the SULTAN facility, located at CRPP in Villigen, Switzerland [47]. As illustrated in figure 10, SULTAN samples are 3.6 m long, with a high field zone (HFZ) of ~400 mm (of the order of the last-stage cable twist pitch). Samples are tested in pairs with joints at the

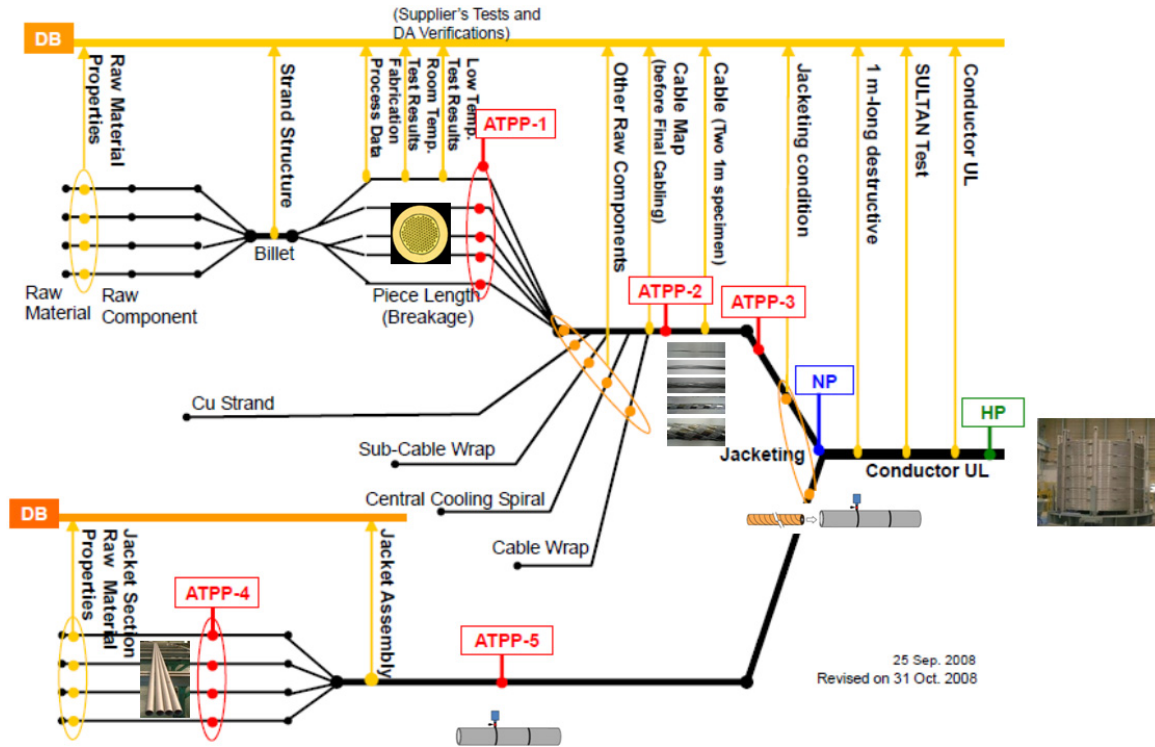


Figure 9. Control points of ITER conductor PAs and business flow of ITER conductor database (courtesy of K Seo, ITER-IO).

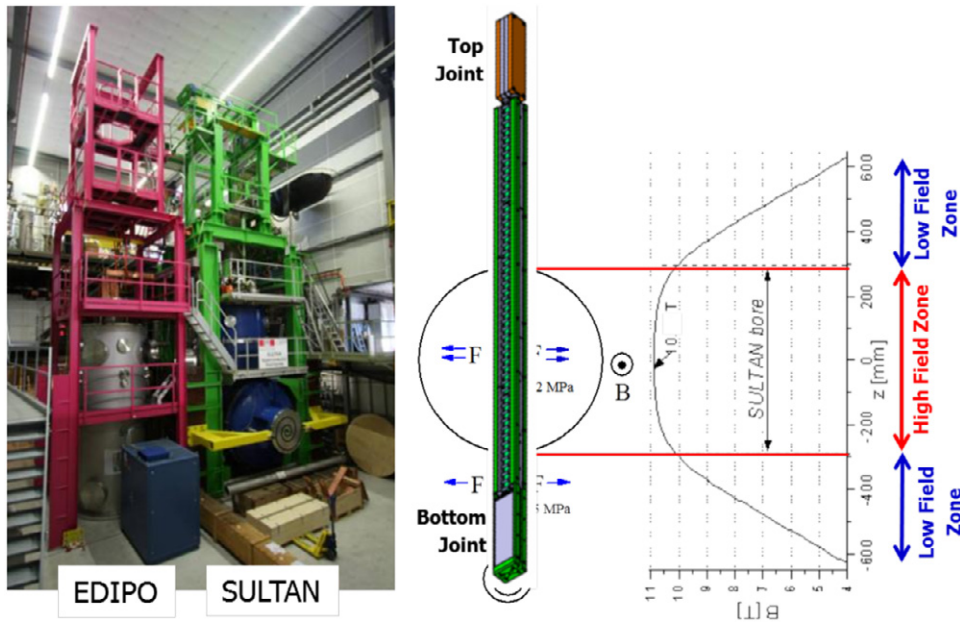


Figure 10. View of EDIPO and SULTAN sample test facilities at CRPP (left) and SULTAN sample configuration (left; courtesy of P Bruzzone, CRPP).

top and bottom (save for the Nb–Ti samples, which do not rely on a bottom joint but are tested in a hairpin configuration) and are instrumented with voltage taps and temperature sensors. Measurements are carried out either at fixed temperature and field, by increasing the transport current (I_C run) or at fixed current and field, by increasing the temperature (T_{CS} run). The T_{CS} runs are the ones used to assess the conductor performance.

The level of full size conductor testing was negotiated with the DAs at the time of PA preparation when it appeared that 100% testing was neither feasible nor acceptable. The present levels of 25% for Nb₃Sn conductors and 10% for Nb–Ti conductors were chosen as a compromise on cost and schedule. To ensure proper management and prioritization of ITER samples, the IO has placed in 2012 a contract with CRPP,

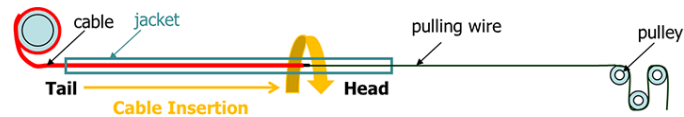


Figure 11. Principle of cable insertion into jacket assembly.

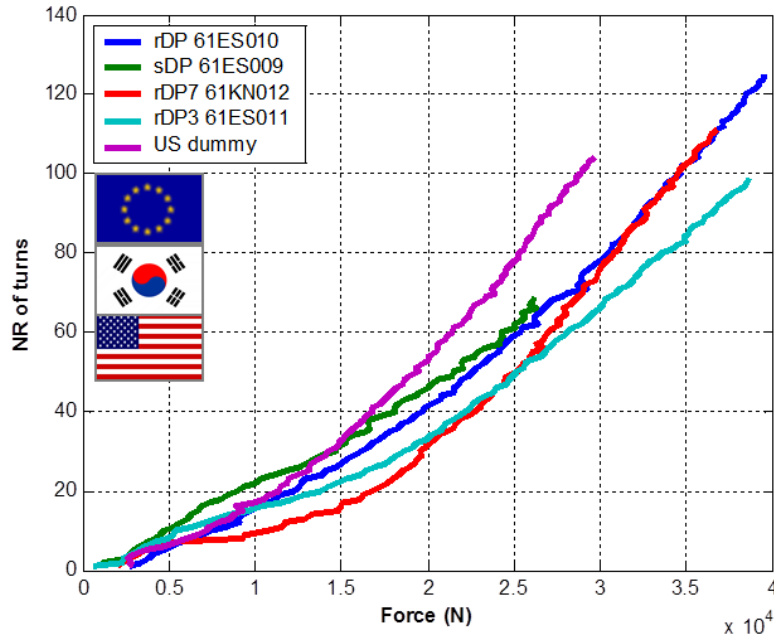


Figure 12. Accumulated number of cable head rotations versus pulling force, as recorded during insertion of TF RF cables at Criotec and HPM.

which reserves 100% of the SULTAN usage for three years. Although SULTAN is very busy, its throughput in terms of sample testing fulfils the needs of the 11 conductor PAs.

Let us note that CRPP has recently commissioned the EDIPO magnet [48]. EDIPO offers some potential advantages over SULTAN (e.g., longer high field zone, more efficient cryogenics. . .). However, it comes too late to be used for ITER since all conductor types and suppliers have been qualified on the basis of SULTAN samples which are used as references for assessing the results of QC samples which are now being tested as part of production monitoring. Switching to EDIPO would require a systematic benchmarking for every type of conductors and a renegotiation with all six conductor DAs of procedures and, possibly, acceptance criteria, resulting in unacceptable risks and delays.

4. Technical challenges

Let us now illustrate some of the technical challenges encountered in the development and the production of ITER conductors.

4.1. Twist pitch elongation

As illustrated in figure 11, during insertion into the jacket assembly, the cable head exhibits a tendency to rotate under the action of the pulling force. The number of rotations can be

measured using a dedicated device, mounted between the cable head and the pulling wire, like the one developed by HPM in the USA, that relies on an accelerometer chip measuring gravity in the directions perpendicular and parallel to the chip face [49]. Figure 12 presents plots of accumulated number of rotations versus pulling force as recorded during the insertion of 415 and 760 m TF cables at Criotec and HPM. It shows that the number of rotations can be up to 130.

The cable rotation results in an elongation of the last stage twist pitch of the cable. The last stage twist pitch elongation was confirmed by careful analyses carried out at the Japan Atomic Energy Agency (JAEA, the Japanese Domestic Agency) of laser diameter measurements performed on conductor jacket after compaction [50]. The measurements reveal a weak periodic pattern that is an imprint of the last stage cable twist. Figure 13 shows a plot of last stage cable twist pitch versus distance from cable head as estimated from laser diameter measurements recorded during the jacketing of a 760 m TF conductor unit length at NSSE. At the tail of the conductor, the twist pitch is 420 mm and it appears to increase gradually along the unit length to reach 470 mm at the conductor head. This high twist pitch value was confirmed by a direct measurement on a destructive examination sample that was cut at the conductor head and for which the last stage cable twist pitch was found to be 475 mm. In comparison, the last stage twist pitch requirement is: 420 ± 20 mm.

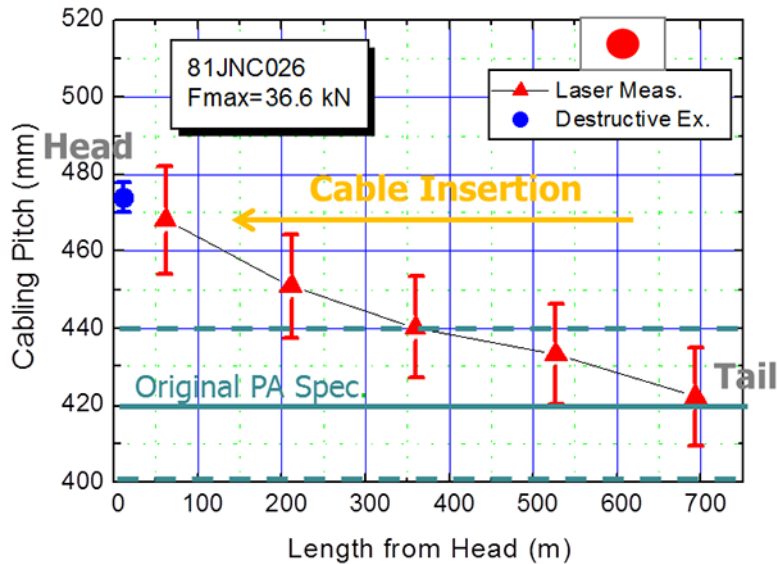


Figure 13. Distribution of last cable stage twist pitch along a 760 m TF conductor unit length manufactured at NSSE estimated from laser diameter measurements (red triangles) and from a destructive examination sample (blue circle; courtesy of Y Takahashi, JAEA).

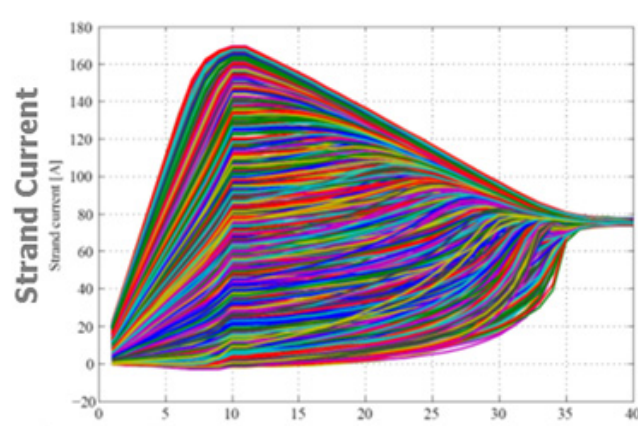


Figure 14. Numerical simulation (using the Jackpot code) of current distribution evolution during a current ramp to nominal current followed by a temperature ramp as in a T_{CS} run on a TF conductor sample at SULTAN. The x -axis count corresponds to successive loading steps; current ramp takes place between 1 and 10; temperature ramp takes place above 10. (Courtesy of E V van Lanen, Twente University.)

Such twist pitch elongation, well known to sailors using rope-type cables, is unavoidable. It can be up to 15%. As long as it is gradual along the cable unit length and only affects the last stage, it is not expected to significantly affect conductor performance and AC losses, in particular for the TF coils which are operated in a steady state. The main issue will be in the joints which should be designed to enable good current transfer out of the six fourth stage petals. The present plan is that the coil manufacturer will re-twist the cable as part of the joint manufacturing procedure. Let us note that the issue described here concerns the last stage twist pitch of the cable while the discussion in section 4.3 concerns the twist pitches of the first stages.

4.2. SULTAN samples

4.2.1. SULTAN sample issues. SULTAN is the only facility in the world where full size, ITER-type CICC can be tested. The

preparation, instrumentation and representativity of SULTAN samples have been the object of many debates within the community. The main issues that have been singled out over the years are:

- For Nb_3Sn samples, how to control and even prevent cable/jacket slippage at the sample extremities that may arise as a result of thermal shrinkage differential between $650\text{ }^\circ\text{C}$ and 4.2 K [51] (the integrated thermal shrinkage of Nb_3Sn is estimated to be -0.9% while that of stainless steel is estimated to be -1.5% [52]) and how to ensure that the sample is in a reproducible and representative strain state (compressive for the cable and tensile for the jacket)?
- For all samples and given the large number of strands in the cable (900 superconducting strands in the case of TF), how to ensure good current distribution among cable strands and prevent large current imbalances like the ones depicted in figure 14 [53]?

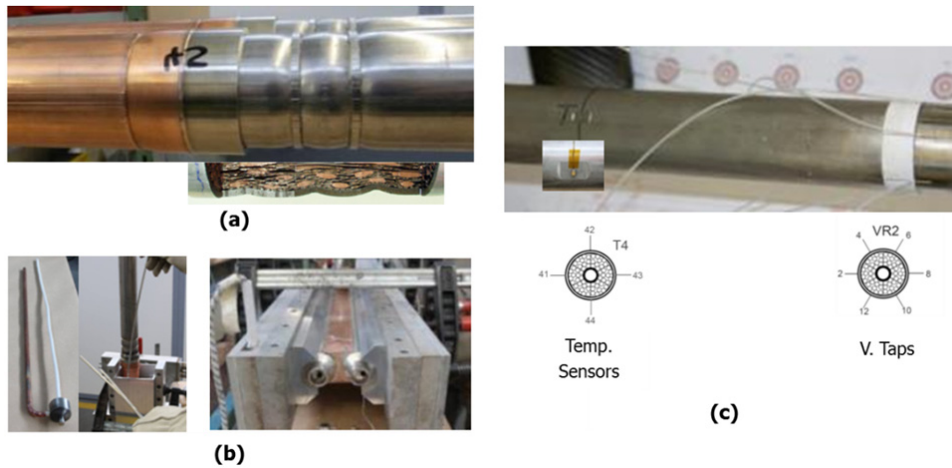


Figure 15. Improvements implemented in the preparation/instrumentation of SULTAN samples at CRPP (courtesy of P Bruzzone, CRPP).

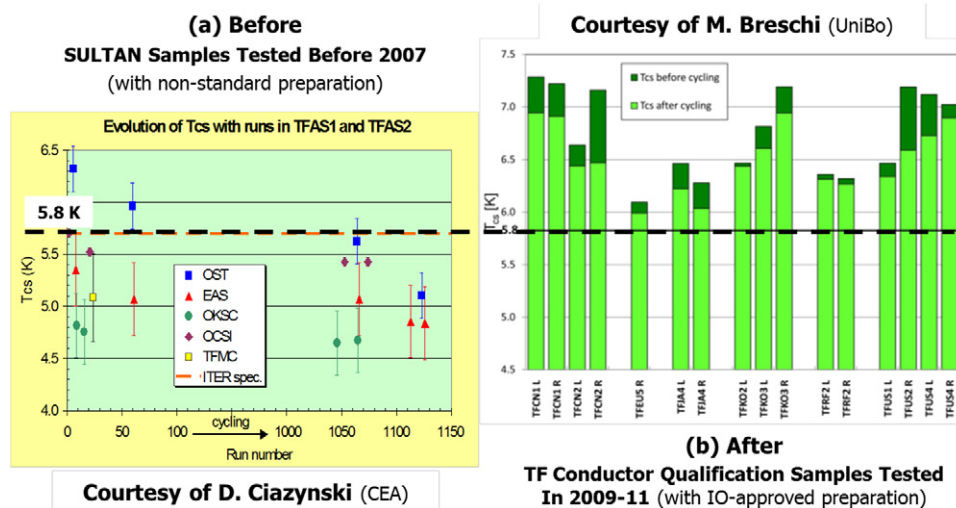


Figure 16. Results of T_{CS} measurements on ITER conductor samples at SULTAN before (a) and after (b) implementation of improvements in sample preparation and instrumentation.

- How to best assess average sample voltages and temperatures?
- Are the results of SULTAN samples (where a short high field zone is in close proximity to joints) representative of in-coil performance?
- How to extrapolate the effects of hoop strains that develop in a real coil (in particular for the CS)?

In 2007 and 2008, ITER IO funded several contracts at CRPP to improve SULTAN sample preparation and address the above issues. The final procedure, agreed with all six domestic agencies involved in conductor production, and which is used for qualification and production samples, includes [54]

- two sets of crimping rings at both ends of the sample (to prevent cable/jacket slippage; see figure 15(a)) [55],
- solder-filled joints for both the bottom joint and the upper terminations (to ensure good current uniformity among cable strands; see figure 15(b)) [56, 57], a process

promoted by the US ITER Project Office (US-IPO) and first implemented on a SULTAN sample prepared by MIT [58],

- crown arrays of six voltage taps and four temperature sensors mounted on the conductor jacket and on both sides of the high field zone (which have been shown by analyses to best approximate average cable properties; see figure 15(c)) [59].

The results of these improvements are clearly illustrated in figures 16(a) and (b) which display the results of T_{CS} runs carried out on two sets of full-size, Nb₃Sn conductor samples for ITER: one set tested before (16(a)) [60] and one set tested after (16(b)) the final preparation procedure was implemented. The samples presented in figure 16(b) correspond to the TF conductor performance qualification samples (CPQS) that each DA was required to manufacture and test to qualify potential suppliers prior to contract award and launch of production [54]. All CPQSs met the acceptance criterion for

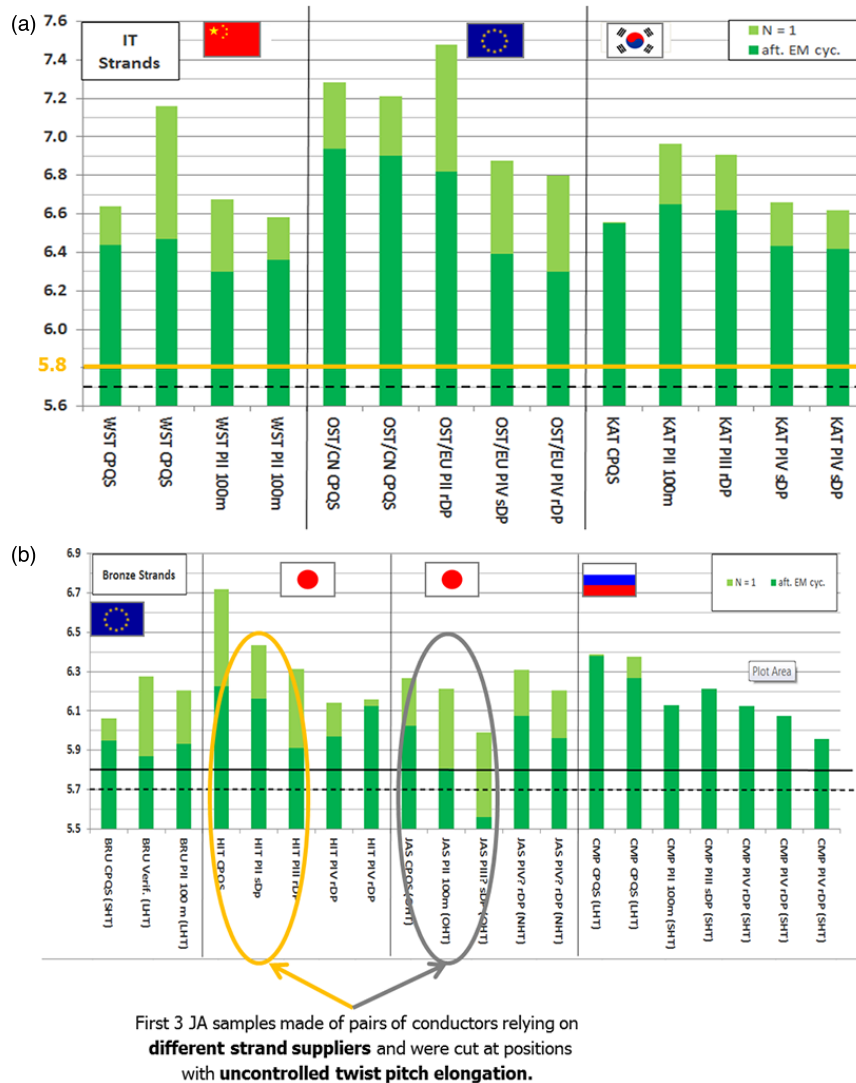


Figure 17. Results of T_{CS} measurements on ITER TF conductor production samples: (a) conductor relying on IT strands (top) and (b) conductor relying on bronze strands (bottom).

TF conductors defined as: T_{CS} (at $10 \mu V m^{-1}$) greater than 5.8 K after 1000 electromagnetic (EM) cycles to 68 kA in a SULTAN background field of 10.78 T (corresponding to a conductor peak field of 11.8 T and an effective uniform field over the high field zone of 11.3 T). Note that the acceptance criterion only includes EM cycling and no thermal cycling, and that 1000 cycles corresponds to the maximum number of EM cycles to be experienced by the TF coils over the life time of the machine.

4.2.2. SULTAN sample summary. Since 2009, a number of TF conductor production samples have been tested, making it possible to gather statistics for both internal tin (IT) and bronze conductors and to look for trends. Figure 17(a) presents a summary of T_{CS} data obtained for the three conductor productions relying on IT strands in CN [19], EU [61, 62] and KO [63, 64]. All IT TF conductor samples show good performance, with a significant margin above 5.8 K after 1000 EM cycles.

Figure 17(b) presents a similar plot for the conductor productions relying on bronze strands. In this case, all samples

but one (corresponding to JA UL 81JNC005) met the 5.8 K after 1000 EM cycles, however the margin is much smaller than for IT samples. Looking at the details of the results, it appears that all RF samples show good performance with no cycling degradation (there is even usually a small increase of T_{CS} over the first 50 to 100 EM cycles, the origin of which is not understood but may be similar to that observed on the CS conductor samples discussed in 4.3) [65, 66]. The bronze EU samples are reproducible, but appear very close to the limit after EM cycling (this particular conductor design was optimized to perform in such fashion) [62]. The first three sets of data from the two JA suppliers show irregular performance (there even appears to be a degradation from sample to sample) [67, 68]. There are two peculiar facts regarding these samples:

- unlike all the other samples presented in figure 17, the first three JA samples were made of pairs of conductors relying on strands from different suppliers (one leg from strand supplier 1, the other leg from strand supplier 2),

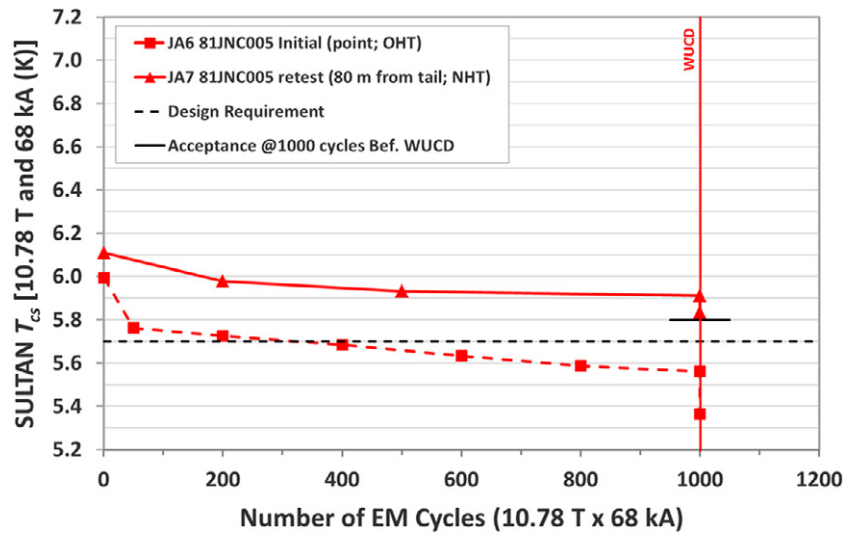


Figure 18. Summary plot of T_{CS} versus EM and thermal cycling measured on two samples cut from TF conductor UL 81JNC005.

- the samples were cut at the head of the conductors after compaction at a time when the issue of twist pitch elongation described in section 4.1 had not yet been identified; therefore, they were likely cut in a region of uncontrolled variations of last stage twist pitch.

After these three initial samples, JA tested two more samples which were made of conductor pairs relying on the same strand supplier (two legs from either strand supplier 1 or strand supplier 2) and which were cut in a region where the last stage twist pitch is under control. As seen in figure 17(b), both samples were successful and met the 5.8 K criterion after 1000 EM cycles with some margin.

The above results seem to indicate that the erratic behaviour of the earlier JA samples was due to a sample problem rather than a conductor problem. To confirm this hypothesis, IO and JA agreed to retest a conductor sample cut from UL 81JNC005, but this time, about 80 m from the tail end, where last stage twist pitches are known to be under control and close to the nominal value and to pair it with a leg from another UL made from strands from the same supplier. Figure 18 presents a comparison of the test results between the initial sample (cut at the head and paired with a conductor relying on strands from a different supplier) and the second sample (cut towards the tail and paired with a conductor relying on strands from the same supplier). The second sample performs much better and meets the T_{CS} criterion of 5.8 K after 1000 cycles (it also stays above 5.8 K after warm up cool down). In addition to the location of the cut and the pairing of the SULTAN legs, the retest sample relies on a slightly different heat treatment that is expected to increase strand critical current by up to 4%. It is not possible at this stage to conclude which of these factors had a preponderant effect, but they appear to have eliminated the problem that caused the initial sample to fall below the acceptance criterion.

Let us note that JA has decided to set UL 81JNC005 aside (it will be used for winding trials by one of the JA coil manufacturers) and that the new heat treatment applied on the retest sample will be used for all the conductor ULs made from strands of this supplier.

4.2.3. Correlation with Nb_3Sn strand performance. A long-standing question has been whether or not the performance of a Nb_3Sn CICC sample tested in SULTAN could be related to the performance of its strands. In the past, all attempts at finding such correlation failed, leading to a flurry of papers and interpretations. The ITER TF conductor production offers the unique opportunity of looking at a data set on a series of samples prepared in the same manner and cut from conductors manufactured in a reproducible way. Figure 19 shows a plot of T_{CS} measured during the first energization after cooldown at 68 kA and 10.78 T (background field) for selected ITER TF conductor samples versus the average critical current, I_C , of their strands measured at 4.22 K and 12 T (on so called 'ITER barrel') as part of QC tests during production (the ITER barrel was introduced in the mid-1990s in an effort to standardize strand critical current measurements). The data are not randomly distributed and there appears to be a correlation.

The correlation can be further improved by applying a correction to the I_C data. Indeed, when measured on ITER barrel, the strands are more or less unconstrained, and the Nb_3Sn filaments only experience the intrinsic compressive strain arising from the thermal shrinkage differentials between the filaments and the other materials constitutive of the strands. This intrinsic strain is usually estimated in the range of -0.15 to -0.25% [52, 69]. In a CICC, this intrinsic strain is augmented by the strain applied by the stainless steel jacket, whose integrated thermal shrinkage between 650°C and 4.2 K is larger than that of Nb_3Sn , to reach a value of the order of -0.5% (see section 4.3.7).

ITER IO has placed a contract with Twente University to fully characterize the I_C versus strain dependency of all ITER strand types [70]. The Twente measurements are carried out on a dedicated test set up, based on a circular bending beam (referred to as Pacman), and enable an assessment of the slope of the I_C versus strain degradation on the compressive side which is usually linear. The slope appears to vary by a factor of 2 depending on the strand type. Figure 20 shows the same data as in figure 19, but they have been averaged over each

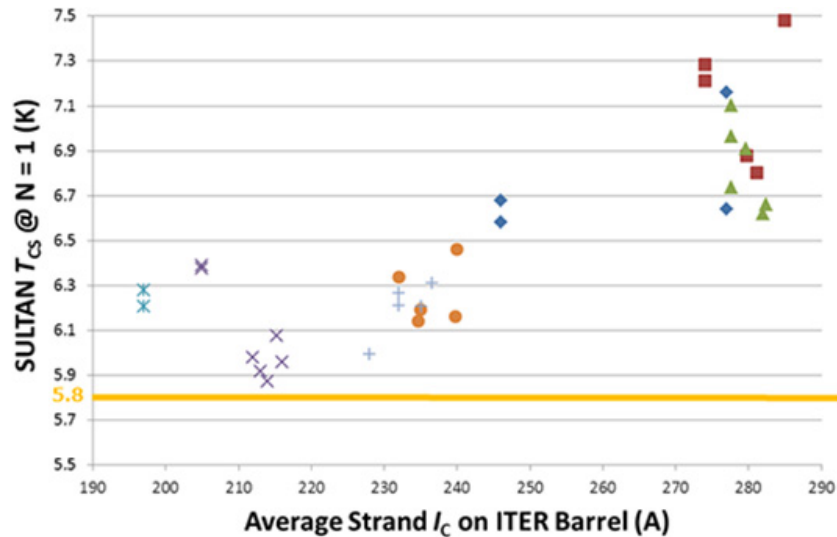


Figure 19. Correlation plot of T_{CS} (at 68 kA and 10.78 T background field) assessed during first energization cycle versus average strand I_C (at 4.2 K and 12 T) on ITER barrel for ITER TF conductor production SULTAN samples.

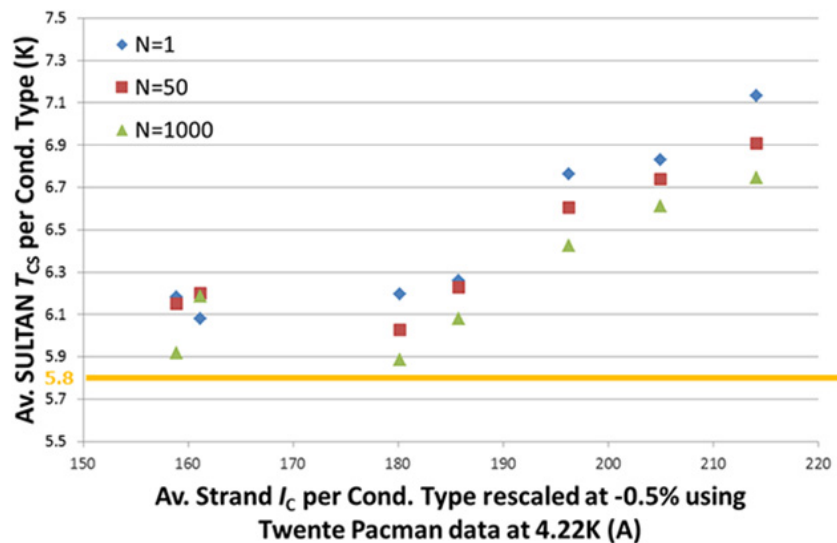


Figure 20. Correlation plot of average T_{CS} (at 68 kA and 10.78 T background field) per ITER TF conductor/strand type assessed for first, 50th and 1000th energization cycle versus rescaled average strand I_C (at 4.2 K, 12 T and about -0.5% strain) using slope of I_C versus strain curve measured for each strand type on pacman set up at Twente University.

conductor/strand type and the I_C data have been rescaled to a strain of -0.5% using the slope assessed by Twente University for each strand type. In addition, figure 20 shows the T_{CS} results for cycle 1, cycle 50 and for the last cycle (usually 1000). This time and in spite of the crude correction that is applied, there appears a clear correlation between the average T_{CS} of the SULTAN samples and the re-scaled average I_C of their strands in the 180 to 220 A range.

4.2.4. Correlation with in-coil performance. The consistency of the results presented above provides strong evidence that SULTAN can be used for QC testing of CICC as foreseen in the procurement arrangements for the ITER conductors. A final question is whether or not SULTAN test results are representative of in-coil performance. In particular, there are

some concerns that the sample configuration and the short high field zone result in strain distributions and/or strain relaxations along the conductor sample leg that affect the T_{CS} and that would not occur in a real coil configuration and may result in an enhancement of the T_{CS} degradation [71]. Some other authors are also concerned with the proximity of the joints that may facilitate current redistribution among cable strands, resulting in an overestimate of the T_{CS} [72].

These issues will be assessed by the manufacture of a new central solenoid Insert (CSI) coil to be tested at the central solenoid Model Coil (CSMC) facility in Naka [73], Japan and by the manufacture and test of a matching SULTAN sample, cut from the same conductor unit length. The new CSI has been designed by the US-ITER Project Office (US-IPO) [74] and is being manufactured in Japan under the supervision of

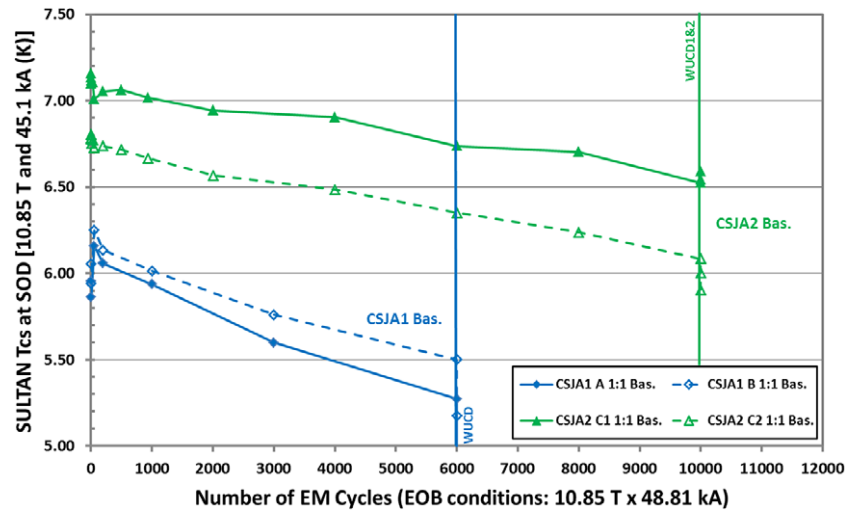


Figure 21. Summary plot of T_{CS} versus EM and thermal cycling measured on first set of CS conductor qualification samples prepared under the supervision of JAEA (CSJA1 and CSJA2).

JAEA. A cold test is foreseen in 2014/15. The motivation for this new CSI test is twofold:

- (1) to determine the ultimate performance of the CS conductor in a real coil configuration, taking into consideration the effects of the hoop strain (up to +0.17% in the second coil module from the top of the stack, referred to as CS2U),
- (2) to compare the results of the CSI test with those of the matching SULTAN sample (where the hoop strain effects cannot be simulated). Note that this is the first time that an ITER model coil test will be accompanied by a matching SULTAN sample test.

There is also a plan to compare the results of samples cut from adjacent locations in the same conductor unit length and tested in SULTAN and in EDIPO, to see if the longer high field zone of EDIPO leads to different performances. However, the work load of CRPP has not yet enabled to carry out such a comparison.

4.3. CS conductor degradation

4.3.1. CS coil requirements. As already explained, the CS coil is made up of six modules which are independently powered. Unlike the TF coils, which are operated in a steady state, the CS and PF coils must be capable of driving inductively 30 000 15 MA plasma pulses with a burn duration of 400 s [4, 25]. This implies that during their lifetime, the CS coil modules will have to sustain severe and repeated electromagnetic (EM) cycles to high current and field conditions, which are way beyond anything large Nb₃Sn coils have ever experienced.

The CS conductor qualification program calls for the manufacture and test of SULTAN samples to be subjected to a large number of EM cycles (e.g., 10 000). The expectation from the ITER model coil test program, in particular, the first CS Insert coil tested in the CSMC in Naka in 2000, is that the conductor performance should achieve stabilization after a few thousand EM cycles [75, 76].

4.3.2. Early JA samples. In 2010 and 2011, JAEA tested two CS conductor qualification samples referred to as CSJA1 and CSJA2. CSJA1 relies on second generation bronze strands from two suppliers similar to those used for the TF production [35], whereas CSJA2 relies on a new (third) generation of bronze strands from a third supplier, with non-copper critical current densities in excess of 1000 A mm⁻² at 4.2 K and 12 T (on ITER barrel) [77].

As illustrated in figure 21, which shows plots of T_{CS} versus number of cycles for the four legs of CSJA1 and CSJA2, the performance of CSJA1 was unacceptable, whereas that of CSJA2, although much better, did not exhibit any tendency to saturate [61, 78].

An autopsy of CSJA1 carried out by JAEA enabled two critical observations [78]:

- (1) in the high field zone of the sample, which was subjected to high Lorentz forces, the cable appears to have been permanently displaced inside the conduit (see figure 22(a)).
- (2) The non-compressive side of the high field zone cable shows evidences of strand buckling and even cracking (see figure 22(b)).

These observations provided clear indications that the conductor design used for these samples was not appropriate for this application.

4.3.3. IO crash program. Although the issue of Nb₃Sn CICC conductor degradation has been identified since the time of the ITER model coil program [75, 76, 79, 80], very few systematic studies have been carried out to identify the parameters that influence it. Some attempts were made on sub-size cables, but the results were rather inconclusive [81, 82]. The most comprehensive R&D program was carried out within the framework of the conductor development for EDIPO [83, 84]. This program confirmed the importance of the twist pitch sequence, but the optimization dealt with rectangular

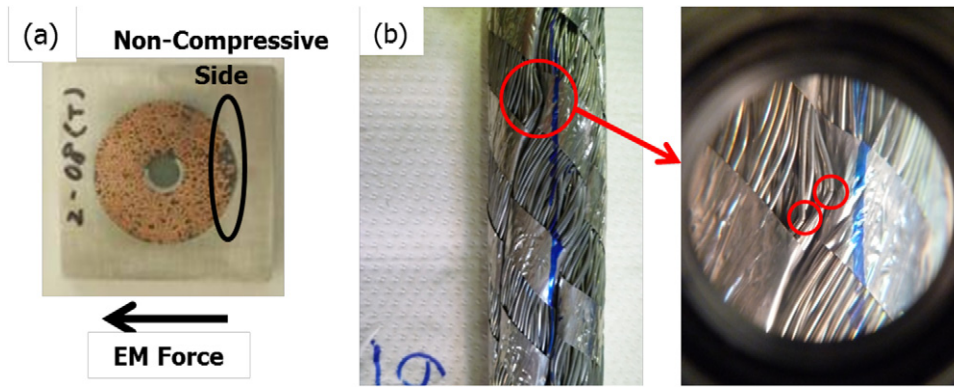


Figure 22. Pictures from the autopsy of CSJA1 at JAEA showing: (a) evidence of global displacement of cable inside conduit under the effect of the Lorenz force (left) and (b) evidence of strand buckling/cracking on the non-compressive side of the high field zone section (right; courtesy of Y Takahashi, JAEA).

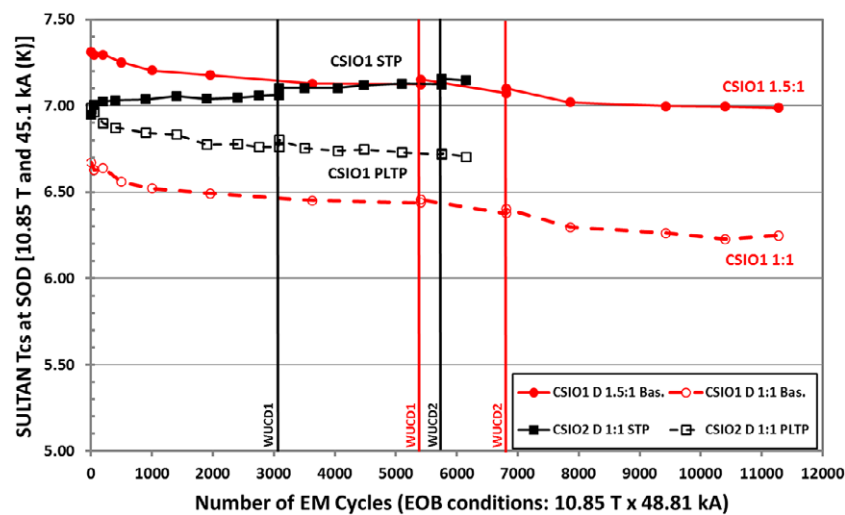


Figure 23. Summary plot of T_{CS} versus EM and thermal cycling measured on CS conductor qualification samples prepared as part of the IO crash program (CSIO1 and CSIO2).

conductors having 108 strands, while the CS conductors are round-in-square, with six petals made up of 146 strands each. The different shape and the much larger size called for another optimization program.

In the spring of 2010, ITER-IO launched, with support from the US ITER Project Office (US-IPO) and the strand supplier OST, a detailed crash program to investigate different CS strand/cable configurations so as to achieve more robust performance as a function of electromagnetic and thermal cycling [25]. The program was aimed at assessing

- internal tin versus bronze strand designs [25],
- the effect of copper segregation, by comparing baseline cable inner triplet design with $(2 \times 1:1 \text{ sc} + 1 \times \text{Cu})$ strands [18] versus ITER model coil triplet design with $(3 \times 1.5:1 \text{ sc})$ strands [85, 86],
- the effect of cable twist pitch sequence, by comparing short [87, 88], versus baseline [18], versus pseudo long twist pitches [89].

This led to the manufacture of four types of conductors and two SULTAN samples, referred to as CSIO1 and

CSIO2 [25]. Table 1 summarizes the salient parameters of these conductors/samples. It should be noted that it is the first time in the ITER history that such a systematic R&D program, where only one parameter is changed at a time, was carried out.

Figure 23 shows plots of T_{CS} versus number of cycles for the four legs of the CSIO samples. Three of the legs (CSIO1 1.5:1, CSIO1 1:1 and CSIO2 PLTP) exhibit a more or less similar degradation as a function of EM and thermal cycling, while the remaining leg, CSIO2 STP, exhibits a fundamentally different behavior: its T_{CS} does not degrade, on the contrary, it keeps increasing slightly as a function of both EM and thermal cycling. The CSIO2 STP conductor relies on IT strands, a baseline $(2 \times 1:1 \text{ sc} + 1 \times \text{Cu})$ inner triplet, short twist pitches and tight compaction and was the first conductor sample to pass the SULTAN test qualification for CS conductors. The use of short twist pitches has been advocated by CEA since the early 1990s [87] and the twist pitch sequence used in CSIO2 STP is similar to the sequence used in the inner layer (1.1) of the CS Model Coil manufactured and tested in the late 1990s [86].

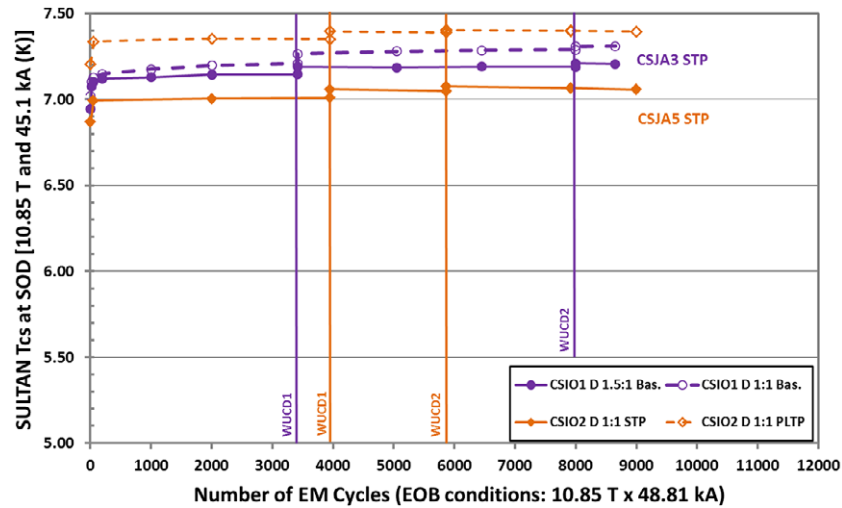


Figure 24. Summary plot of T_{CS} versus EM and thermal cycling measured on the second set of two CS conductor qualification samples prepared under the supervision of JAEA (CSJA3 and CSJA5).

Table 1. Salient parameters of CSIO conductors.

	Baseline PA requirements	CSIO1 left leg (1.5:1)	CSIO1 right leg (1:1, ~baseline)	CSIO2 left leg (STP)	CSIO2 right leg (PLTP)
Strand					
Type	CS	IT	ITER TF/IT	ITER TF/IT	ITER TF/IT
Diameter (mm)	0.830 ± 0.005	0.82	0.82	0.822–0.823	0.822–0.823
Cu:non-Cu ratio	1.0:1	1.5:1	1.0:1	0.94–0.95	0.94–0.95
I_c at 12 T, 4.2 K on ITER barrel (A)	≥ 220	223–226	263–274	266–274	266–274
Cable					
Layout	(2 sc + 1 Cu)	(3 sc)	(2 sc + 1 Cu)	(2 sc + 1 Cu)	(2 sc + 1 Cu)
	$3 \times 4 \times 4 \times 6$	$3 \times 4 \times 4 \times 6$	$3 \times 4 \times 4 \times 6$	$3 \times 4 \times 4 \times 6$	$3 \times 4 \times 4 \times 6$
Stage 1 twist pitch (mm)	45 ± 5	45	45	22 ^a	110 ^a
Stage 2 twist pitch (mm)	85 ± 10	83	83	45 ^a	115 ^a
Stage 3 twist pitch (mm)	145 ± 10	141	141	81 ^a	127 ^a
Stage 4 twist pitch (mm)	250 ± 15	252	242	159 ^a	140 ^a
Stage 5 twist pitch (mm)	450 ± 20	423	423	443 ^a	385 ^a
Compacted conductor					
Outer dimensions (mm)	49.0×49.0	49.0×49.0	49.0×49.0	49.0×49.0^a	48.3×48.3^a
Jacket inner \varnothing (mm)	32.6	32.6	32.6	32.9 ^a	31.8 ^a
Void fraction (%)		33.4	33.4	32.4 ^a	29.1 ^a

^a Measured by destructive inspection of the compacted conductor sample.

4.3.4. New JA samples. Following up the success of the ITER-IO crash program, JAEA manufactured a new set of two SULTAN samples (four legs), referred to as CSJA3 and CSJA5, relying on third generation bronze strands from three different Japanese suppliers and short cable twist pitches/tight compaction similar to the successful leg of CSIO2 [90]. Figure 24 shows plots of T_{CS} versus number of cycles for the four legs of CSJA3 and CSJA5. The four legs appear to exhibit a behavior similar to that of CSIO2 STP.

4.3.5. KO sample. In parallel to the preparation of the new CSJA samples, JA initiated a collaboration with KO to manufacture an additional CS conductor sample, referred to as CSKO1, relying on IT strands and STP cables produced in

Korea. The strands were manufactured by KAT and cabled by Nexans Korea, while the conductors were jacketed by NSSE in Japan. The two legs rely on slightly different strand designs that were iterated from the KAT TF strand design [29] so as to reduce the hysteresis losses. The results of this sample are shown in figure 25. The behaviour is similar to the other short twist pitch samples.

4.3.6. Summary of CS conductor qualification program. Figure 26 shows a summary plot for all CS qualification samples tested up to date of ΔT_{CS} versus number of cycles, where ΔT_{CS} is the difference between the T_{CS} at a given cycle number, N , and the T_{CS} at $N = 1$. Figure 25 clearly shows that all STP conductor samples exhibit a similar behavior and

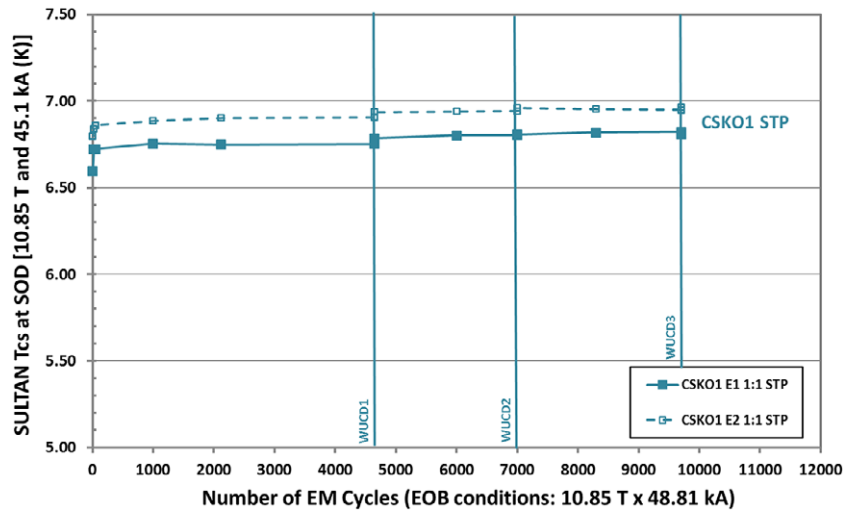


Figure 25. Summary plot of T_{CS} versus EM and thermal cycling measured on a CS conductor qualification sample prepared as part of a collaboration between JA and KO (CSKO1).

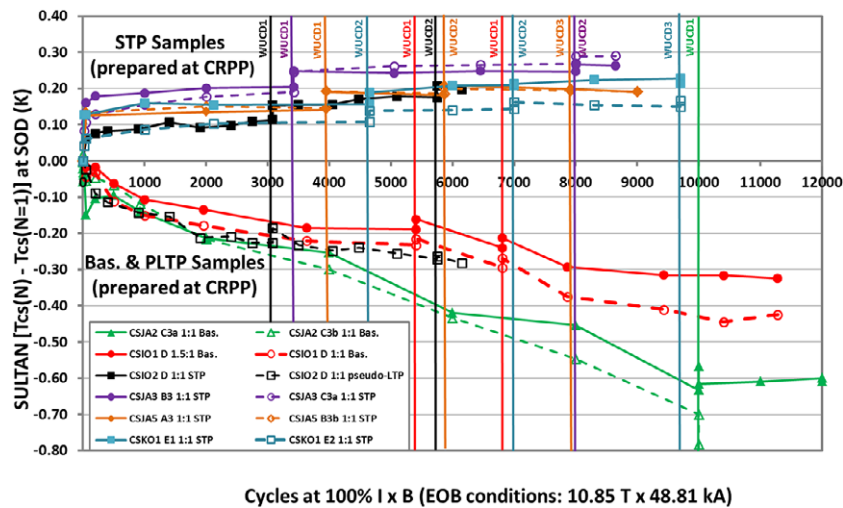


Figure 26. Summary plot of ΔT_{CS} versus number of cycles, where ΔT_{CS} is the difference between the T_{CS} at a given cycle number, N , and the T_{CS} at $N = 1$, for all ITER CS qualification samples tested up to date.

pass the SULTAN test qualification with no degradation versus EM and thermal cycling. In fact, they all exhibit a slight T_{CS} increase that shall be commented upon in section 4.3.8. These successful tests enabled the qualification of five potential strand suppliers (two internal tin and three bronze) and the launch by JAEA of its calls for tender for the manufacture of the CS conductors. At present, contracts have been placed for four modules of the CS coil stack and production is well underway for the conductors of the bottom module (referred to as CS3L).

4.3.7. Thermal strain assessment. The good performances of the short twist pitch samples are confirmed by assessments of thermal strain distributions over the cross-sections of the high field zones of SULTAN samples. The thermal strain is derived from magnetic susceptibility measurements carried out, *in situ*, as a function of temperature, at zero current and background field [91]. As illustrated in figures 27(a) and (b), the strain

distribution assumes a bell-type shape which evolves with cycling. For most samples, such as the baseline leg of CSIO1 (see figure 27(a)), the strain distribution flattens, which is a sign of degradation, and moves towards more compressive strains, which is consistent with the observed decrease in T_{CS} during EM cycling [92]. Such broadening of internal strain distribution was also observed by neutron diffraction technique when comparing data accumulated over a conductor volume corresponding to the non-compressive side of the high field zone of CSJA1 with those accumulated over a conductor volume in the low field zone, that has not experienced the effect of the Lorentz forces [93]. However, in the case of the STP conductor samples, such as CSJA5 (see figure 27(b)), the strain distribution does not deform, confirming the absence of degradation, and moves towards less compressive strains, which is consistent with the observed increase in T_{CS} during EM cycling [94].

Let us note that the bell shape distributions after cooldown presented in figure 27 are centered around -0.5% . This is the

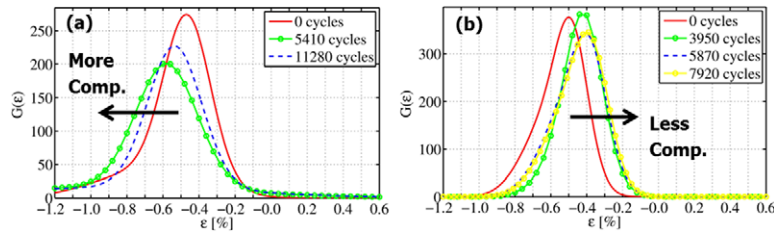


Figure 27. Evolution of the thermal strain distribution over the cross-section of the high field zones of ITER CS conductor SULTAN samples as a function of EM cycling: (a) baseline leg of CSIO1 (left) and (b) CSJA5 STP (right; courtesy of C Calzolaio, CRPP).

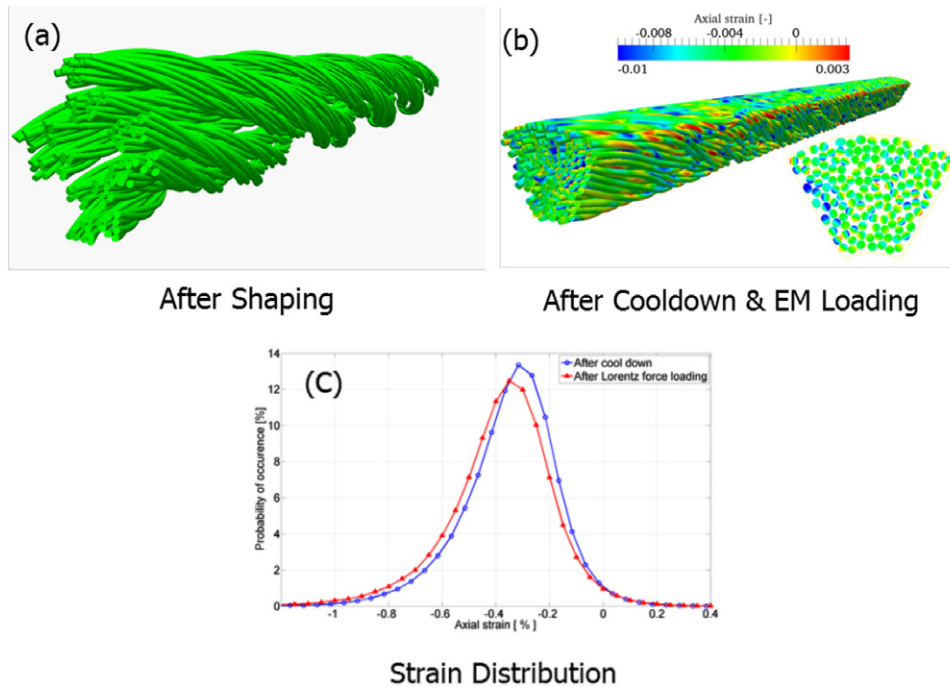


Figure 28. ITER CICC petal as modeled by the Multifil code (TF conductor): (a) after shaping, (b) after cooldown and electromagnetic loading and (c) strain distribution after cooldown and after cooldown and energization (courtesy of D Durville, ECP and H Bajas, CERN).

justification for the value assumed in the rescaling of the I_C data in section 4.2.3 and figure 20.

4.3.8. Multifil analyses. Many analyses have been carried out to predict the performance of ITER TF & CS conductors [95–99]. Among them are numerical simulations with the multifil code developed by Ecole Centrale Paris for ITER-IO and CEA [100–102]. As illustrated in figures 28(a)–(c), multifil enables one to compute strain distributions in a petal of an ITER-type CICC as a function of shaping, cooldown and energization. The computed strain distributions assume bell-type shape with very long tails, both in tension and compression, similar to the ones described in section 4.3.7 (compare figures 27 and 28(c)). These long tails are believed to play a dominant role in determining the conductor performance.

Figure 29(a) displays pure bending strain distributions as computed by multifil for the various twist pitch sequences considered in the CSIO samples. It clearly appears that the STP option exhibits less propensity to bending than the Baseline and pseudo-long twist pitch (PLTP) options. This confirms

that the short twist pitches and tight compaction are likely to provide better strand support, and, thereby, to prevent the deleterious bending and displacements believed to be at the origin of T_{CS} degradation.

In addition, the multifil simulations also show that the STP option exhibits the longest tail on the pure compressive side (see figure 29(b)). Since, in the range of interest, the effects of compressive strain are reversible on the strand performance, one can speculate that compressive strain relaxation during EM/thermal cycling is the likely reason for the slight T_{CS} increase observed during testing in SULTAN. At this stage, it is not possible to conclude whether such compressive strain relaxation will also take place in a real coil configuration or if it is an artifact of SULTAN sample tests [71].

4.3.9. FSU metallography. Over the last few years, Florida State University (FSU) has developed some amazing polishing, etching and imaging techniques that can be used to investigate strand deformation and filament fracture in ITER-type CICC [103–105]. Figure 30 shows examples of such images, starting from a full CS conductor cross-section

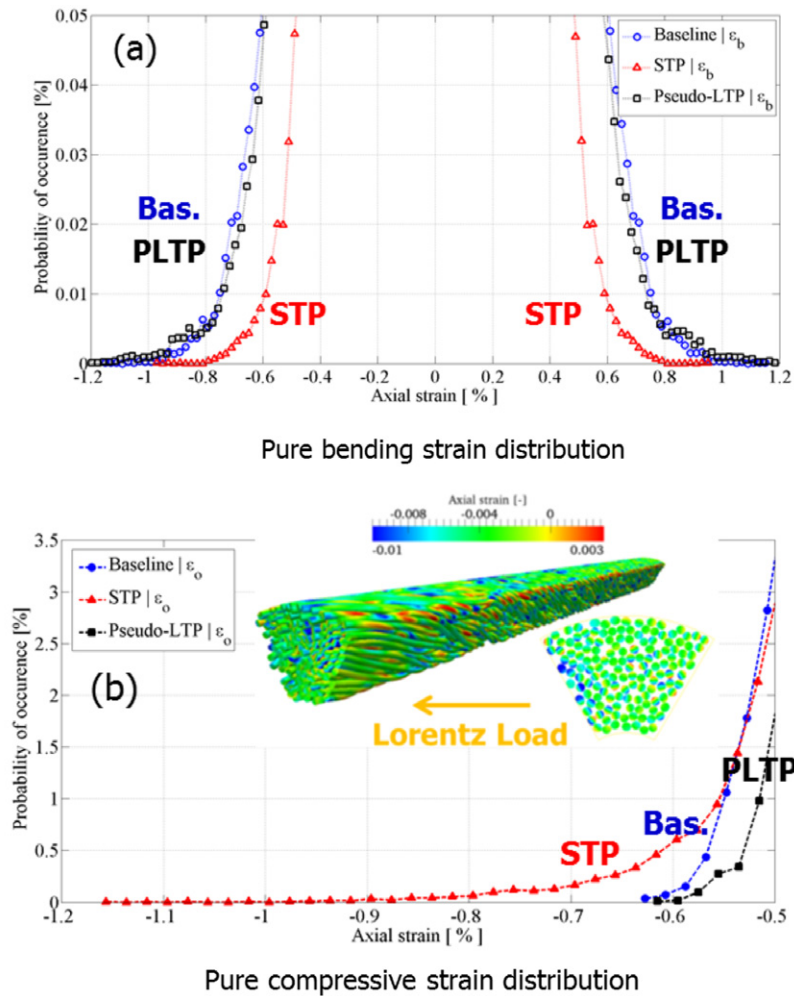


Figure 29. Results of multifil simulations for the three twist pitch sequences used in the CSIO samples (STP: short twist pitch, Bas.: baseline, and PLTP: pseudo long twist pitches): (a) pure bending strain distribution (left) and (b) pure compressive strain distribution (right); courtesy of H Bajas, CERN).

cut from the high field zone of a SULTAN sample after test completion (5 mm scale), followed by images of etched strands showing evidences of broken filaments (200 μm scale), and close up views of the broken filaments' facies showing the details of their grain structure (5 μm scale).

ITER-IO contracted FSU to carry out autopsies of the CSIO SULTAN samples. One of the goals of these autopsies was to look for cracks in strands extracted from both the high field and low field sections, and, in the case of the high field zone, to compare compressive and non-compressive sides of the cable and see if strand buckling/cracking was observed as for the CSJA1 sample. Of course, strand extraction and polishing require a great care to prevent unwanted handling degradations [105].

Cracks are observed using either a laser scanning confocal microscope (LSCM) or a Scanning Electron Microscope (SEM). In the course of these autopsies, FSU identified different crack categories corresponding to different initiation mechanisms [105]. The first type is tensile strain cracks, which are mainly observed on the tensile side of bent strands extracted from petals on the non-compressive side of the cable

(see figure 31(a)). Filament fractures run perpendicular to the strand axis and extend over several filaments. The second type is contact stress cracks, which are mainly observed close to copper areas with a finer grain structure than in the rest of the copper in strands extracted from petals on the compressive side of the cable (see figure 31(b)). Filament fractures run more or less parallel to the strand axis and the finer grain structure is an evidence of cold work. As the copper is expected to be fully annealed during the Nb_3Sn heat treatment (which includes a high temperature plateau at 650 $^\circ\text{C}$ for 100–200 h), the cold work can only originate from the compressive strain applied to the strands as a result of the Lorentz forces. The third type is a mixture of the first two types, where filament fractures assume different orientations and/or follow zig-zag paths (see figure 31(c)).

In order to gather statistics and to be able to compare the four legs of the CSIO samples a number of strands were randomly extracted from specific areas of selected petals in the cable after jacket removal [105, 106]. This comprehensive selection, meant to cover a wide array of strand configurations, includes straight and bent strands located at the corners,

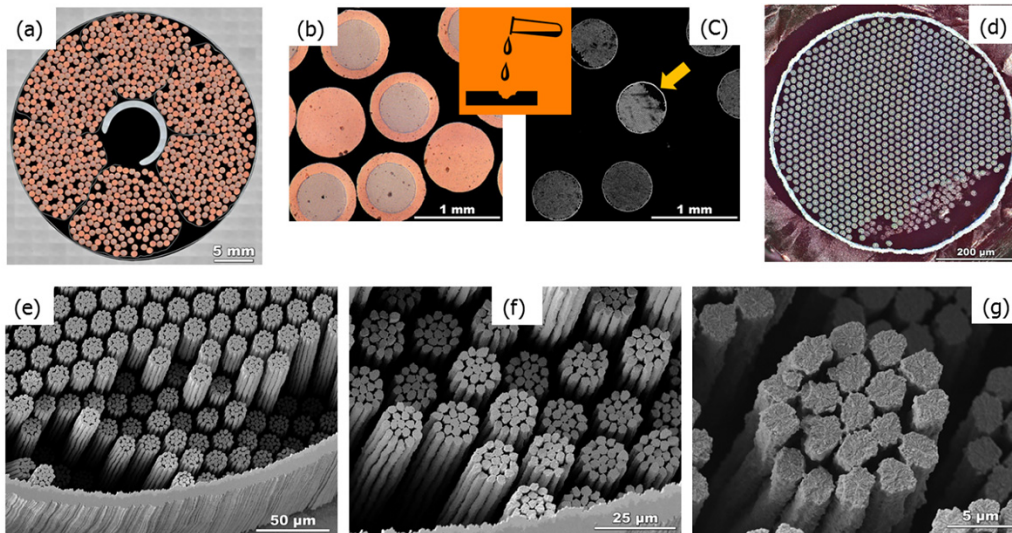


Figure 30. Examples of high resolution images obtained by Florida State University on ITER CICC: (a) cross section of the high field zone of CSJA2, (b) zoom over selected copper and sc strands in cross-section (a), (c) view of sc strands from (b) after copper etching, (e) to (f) FESEM views of broken filaments in multifilament area of etched strand (d) (courtesy of P Lee and C Sanabria, Florida State University).

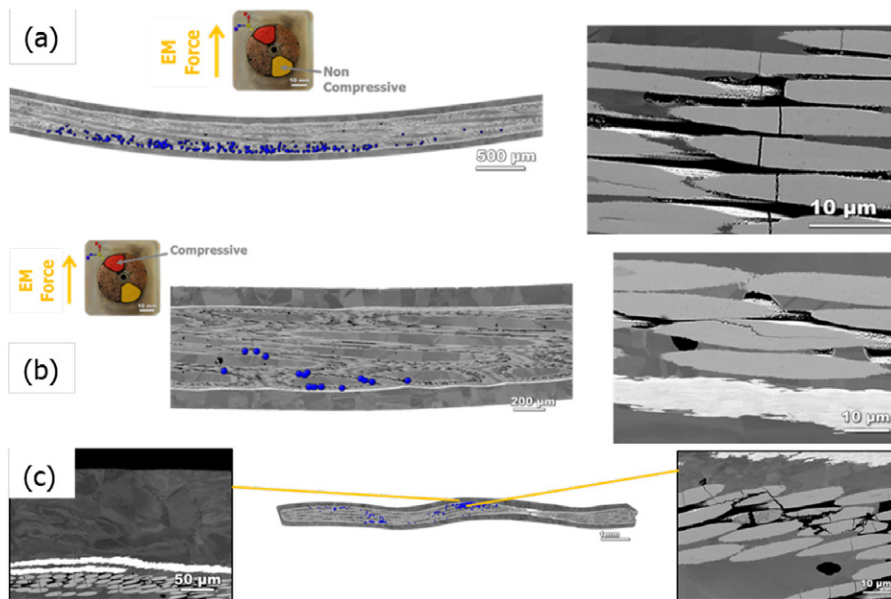


Figure 31. Different crack types observed by LSCM or SEM on ITER-type CICC: (a) tensile strain cracks (top), (b) contract stress cracks (middle) and (c) mixture of tensile strain and contract stress cracks (bottom; courtesy of C Sanabria, Florida State University).

medium part and narrow edge of petals coming from the compressive and non-compressive sides of the cable high field and low field zones. A color coding was applied to retain the strand original location. The main results of these crack counts are:

- no crack was ever observed in strands extracted from the Low Field zones, thereby confirming that thermal strains alone are not enough to induce filament fracture,
- ample evidence of filament fracture was observed in strands extracted from the high field zones of all CSIO sample legs, except for the short twist pitch one where, as illustrated in see figure 32, none of the inspected strands exhibited any crack.

This clear cut result is quite remarkable and confirms that, in the case of IT strands, the short twist pitch sequence is devoid of filament fracture.

To complement the above observations, FSU was also provided cable sections extracted from the high field zones of one leg of CSJA2 and one leg of CSJA3 which are both made up of third generation bronze strands. The results are presented in figure 33. The strands extracted from CSJA2, which relies on baseline twist pitches, exhibit filament fractures similar to those observed on strands extracted the baseline leg of CSIO1 (see figure 33(a)). However, as for the STP leg of CSIO2, no cracks could be found in strands extracted from CSJA3, which relies on short twist pitches (see figure 33(b)). Hence, the short

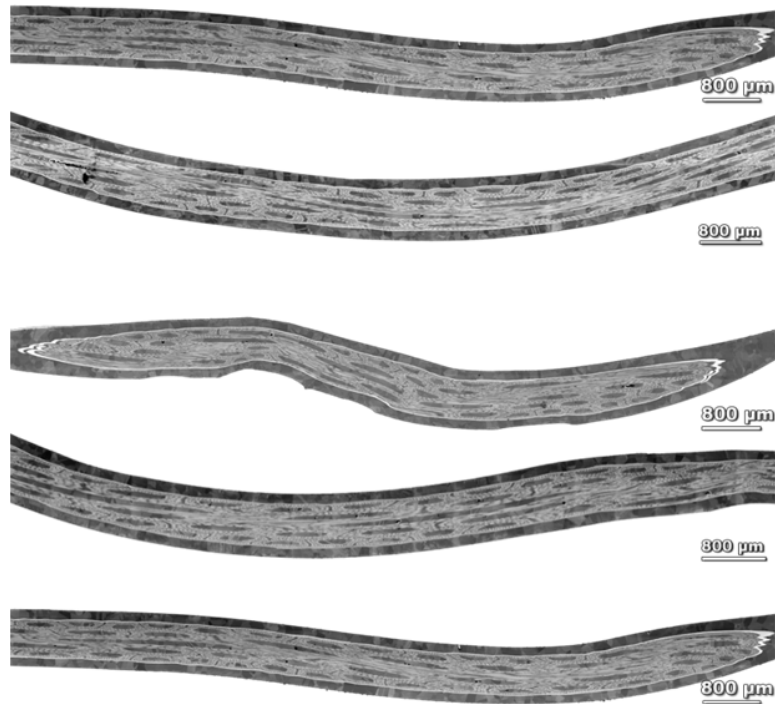


Figure 32. LSCM images of IT strands extracted from the high field zone of the short twist pitch leg of CSIO2 where no crack was observed (courtesy of C Sanabria, Florida State University).

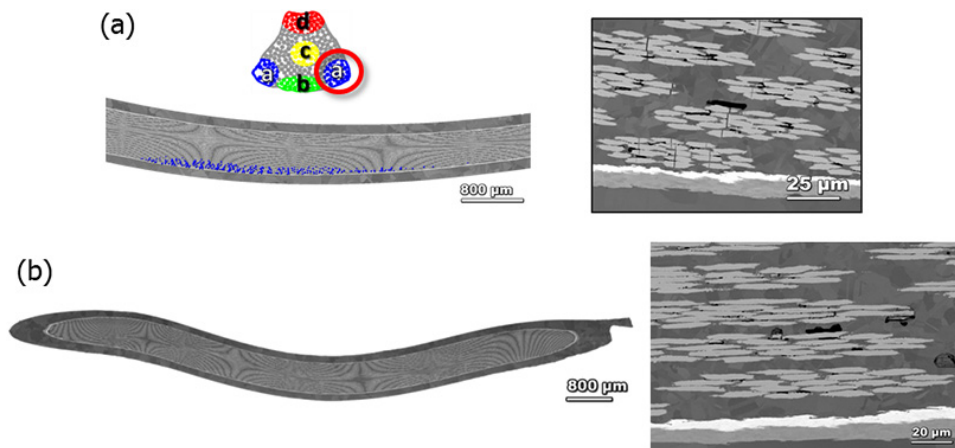


Figure 33. LSCM images of bronze strands extracted from the high field zones of CSJA samples: (a) CSJA2 (baseline twist pitches) and (b) CSJA3 (short twist pitches; courtesy of C Sanabria, Florida State University).

twist pitch sequence appears to have the same effect for both bronze and IT strands.

The fact that no filament fracture is observed on strands extracted from the high field zones of STP conductor samples is a confirmation that, as predicted by multifil, the short twist pitch sequence, where the strands are tightly entangled, offers better strand support against the Lorentz forces, thereby preventing the deleterious displacement and/or bending at the origin of strand degradation. These observations for both IT and bronze conductors provide a lot of confidence on the robustness of the STP design.

4.3.10. CS cabling degradation. The reliance on short twist pitches and tight compaction has resolved the issue of

performance degradation as a function of electromagnetic and thermal cycling, but has given rise to another problem. Destructive examinations (DE) of STP conductors carried out under the supervision of JAEA after cable insertion and compaction have revealed severe strand deformations at the strand crossovers in the cable [107]. As illustrated in figure 34, it appears that the copper strands ((a) and (c)) are more heavily deformed than the superconducting strands ((b) and (d)). It also appears that, in the case of internal tin strands (figure 34(b), top right), these transverse deformations may result in a collapse of the multifilament area, whereas in the case of bronze strands (figure 34(d), bottom right), the multifilament area stays more or less round. It should be pointed out that these deformations

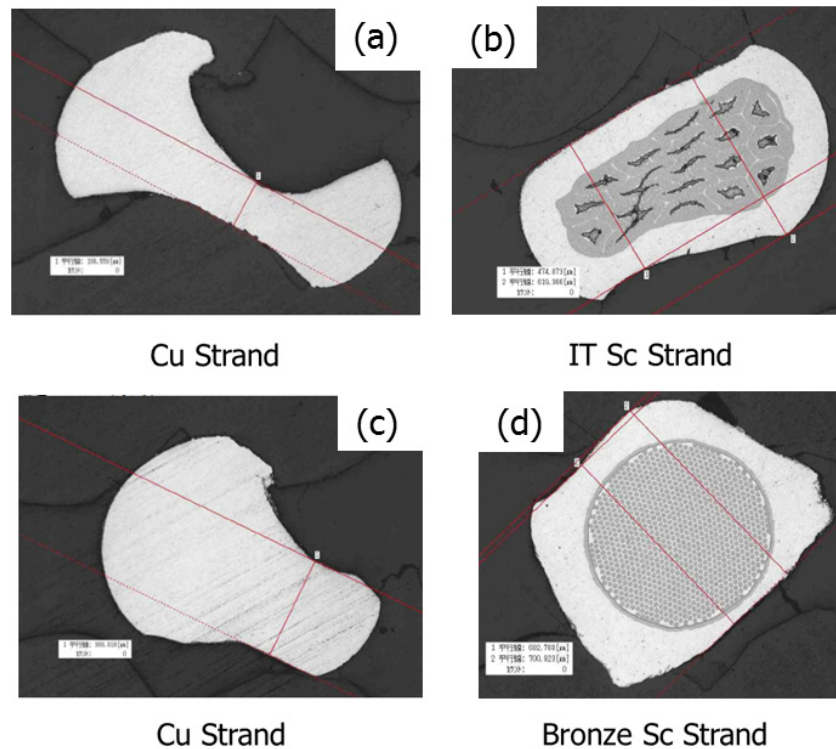


Figure 34. Destructive examinations of short twist pitch conductors showing evidences of strand deformation as a result of cabling: (a) and (b): copper and superconducting strands from a CSIO-type conductor with internal tin strands, (c) and (d) copper and superconducting strands from a CSJA-type conductor with bronze strands (courtesy of Y Takahashi, JAEA).

are applied during cabling, prior to heat treatment and brittle Nb_3Sn compound formation.

Deformations to that extent may have never been observed in CICCs but are reminiscent of those observed at the edges of Rutherford-type cables developed for high-field accelerator magnets [108]. In the case of accelerator magnets, it has been shown that with a proper selection of cabling parameters, the I_C degradation due to cabling can be minimized to about 5% [109].

To assess the effects of cabling degradation on ITER-type strands, JAEA has carried out a series of critical current measurements on dented strands [107]. Figure 35 summarizes the results which show that, for third generation bronze strands, the I_C degradation can be kept below 5% for dents smaller than 0.25 mm. This provides a practical criterion on how much cabling deformation is acceptable during production. Potential Japanese suppliers for CS cables have already demonstrated that they were able to produce long lengths of short twist pitch cables where the sc strand deformations are maintained below 0.2 mm. A similar study will have to be carried out for IT strands, but the fact that that the internal structure of the strand is more prone to collapse may render the cabling optimization more difficult.

Let us note that after years of divergence between most of the fusion and accelerator magnet communities on how to design Nb_3Sn conductors, there now seems to be an agreement that the most suitable way to prevent degradation is to block Nb_3Sn strand bending/displacement, even at the expense of cabling deformation.

5. Production status

5.1. TF conductor productions

5.1.1. Strands. As of today, about 450 t (95 000 km) of Nb_3Sn strands have been produced and registered into the ITER conductor database; this corresponds to about 95% of the total amount needed for the TF conductors. It is the largest Nb_3Sn strand production ever and has called for a significant worldwide production ramp up. Pre-ITER world production was estimated at ~ 15 t year⁻¹. As illustrated in figure 36, it has been steady for the last four years at ~ 100 t year⁻¹.

The eight strand suppliers involved in TF strand productions (four relying on the bronze process and four relying on the internal tin process) have been required to implement Statistical Process Control (SPC) on critical parameters, such as: critical current, I_C (4.2 K, 12 T), hysteresis loss, Q_h (4.2 K, ± 3 T), residual resistivity ratio (RRR), outer diameter and Cr plating thickness. Figures 37 and 38 present typical SPC plots over the whole production of one bronze and one IT supplier who rely on similar billet sizes (~ 60 kg). It appears that the I_C (4.2 K, 12 T) spread can be kept within $\pm 10\%$ for the bronze process (figure 37(a)), while it reaches $\pm 15\%$ for the IT process (figure 37(b)). Data from the EU bronze supplier show an even a smaller spread of $\pm 5\%$ [21]. Note that these variations cannot be explained by Cu-to-non-Cu ratio variations and are likely due to manufacturing tolerances and process variability. It appears also that the Q_h (4.2 K, ± 3 T) spread for the internal tin supplier is at least twice as large as for the bronze supplier

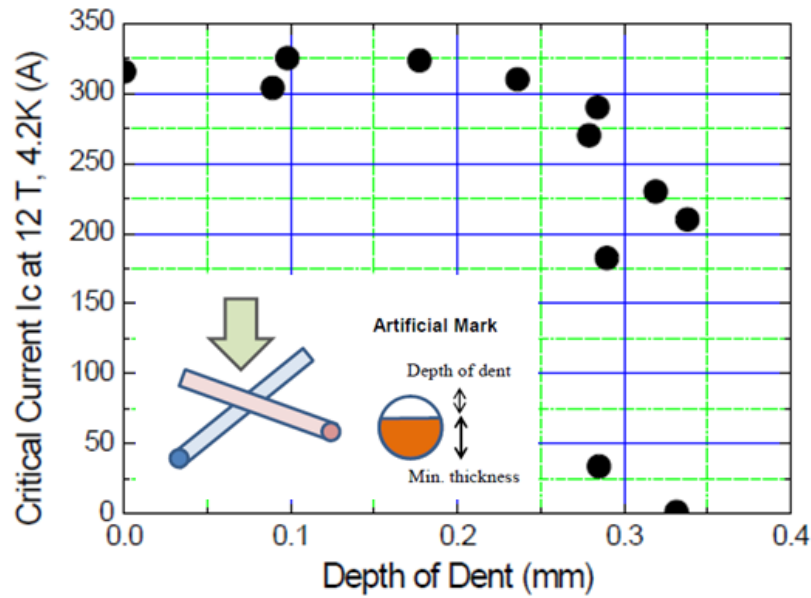


Figure 35. I_C degradation measured on a bronze-type ITER CS strand as a function of depth of indentation simulating strand cross-over in a STP cable (courtesy of Y Takahashi, JAEA).

TF Strand Production Dashboard

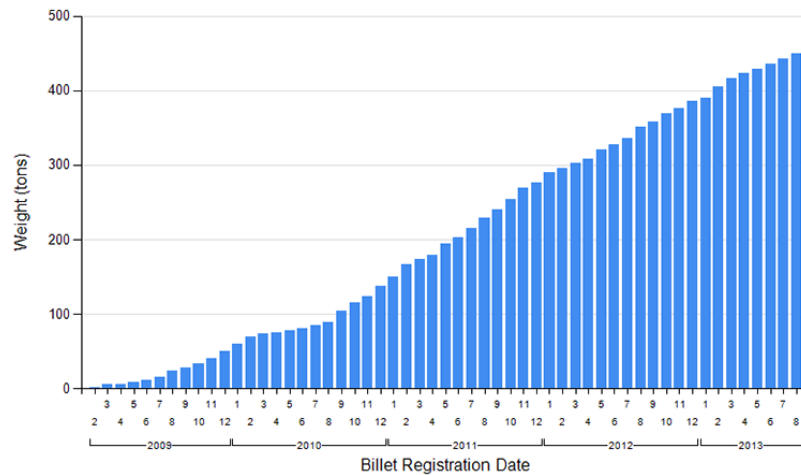


Figure 36. Dashboard of TF strand billet registration into the ITER-IO conductor database.

(compare figures 38(a) and (b)). As a general rule, the I_C and Q_h variations are more difficult to control for IT strands than for bronze strands.

The parameter under SPC that proved the most difficult to control for several strand suppliers turned out to be (rather unexpectedly) the residual resistivity ratio (RRR), which, according to technical requirements should be greater than 100 (as measured on Cr-plated wire after heat treatment) [18]. Considerable efforts were deployed in order to address this problem. At least three factors have been identified as having an influence on the RRR, in particular in the case of Cr-plated wires for which the high temperature plateau during heat treatment exceeds 100 h

- cleanness and quality of strand surface during production so as to prevent entrapment of impurities

underneath the chromium layer that may diffuse during heat treatment and pollute strand copper,

- cleanness of the heat treatment furnace (in particular, for vacuum furnace) and choice and purity of the inert gas in the case of furnaces with inert gas atmosphere. In particular, in the latter case, it is critical to avoid the presence of O_2 which can have deleterious effects on the results leading to significant overestimations [110],
- stability and reproducibility of sample temperature for measurements near 20 K. In particular, the sample holder must be designed to avoid temperature gradients and must be equipped with accurate temperature sensors that properly assess sample temperature.

As a result of these investigations, the heat treatment of three of the TF strand suppliers (two bronze and one internal

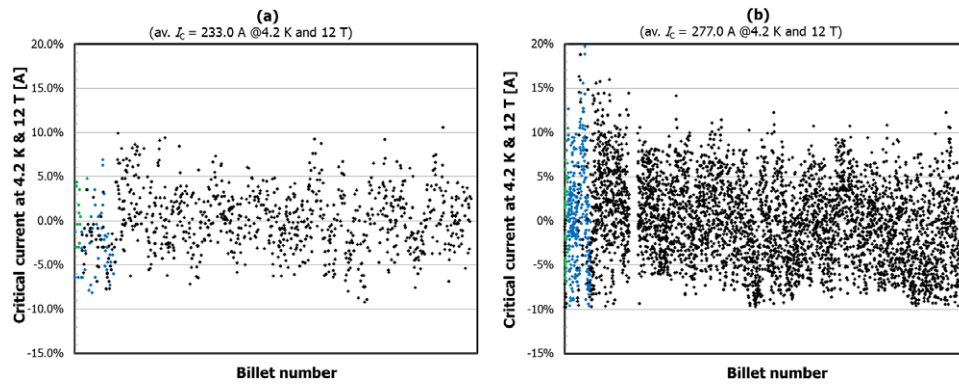


Figure 37. Summary plots of I_C normalized to I_C average (on ITER barrel at 4.2 K and 12 T) versus billet number for the whole production of two ITER TF Nb₃Sn strand suppliers: (a) bronze route supplier (left), (b) internal tin (IT) route supplier (right) (courtesy of M Jewell and N Sullivan, University of Wisconsin at Eau Claire).

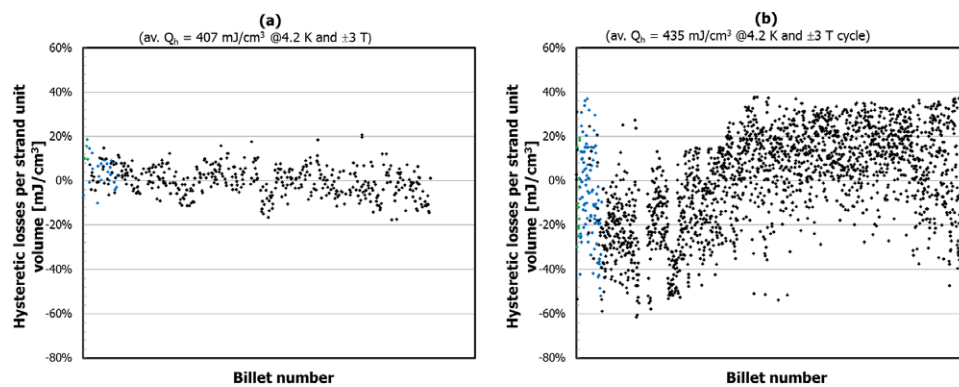


Figure 38. Summary plots of Q_h normalized to Q_h average (at 4.2 K and for a ± 3 T cycle) versus billet number for the whole production of two ITER TF Nb₃Sn strand suppliers: (a) bronze route supplier (left), (b) internal tin (IT) route supplier (right) (courtesy of M Jewell and N Sullivan, University of Wisconsin at Eau Claire).

tin), which called for a 200 h high temperature plateau, had to be modified. For two suppliers, the plateau duration was reduced to 100 h [111], whereas for the third supplier, the plateau temperature was lowered.

Another issue turned out to be the type of Cr used for electroplating. Seven strand suppliers chose hexavalent chromium, Cr⁺⁶, which is widely used in the industry because of its hardness and durability, while one strand supplier chose trivalent chromium, Cr⁺³, which poses less health and safety issues and is generally used for decorative purposes. Although there were concerns from the start [112], the latter supplier managed to develop a stable Cr⁺³ plating process, which passed all acceptance tests on strands, including the flaking test (after winding on a rod whose diameter is three times the strand diameter). However, a serious peeling problem occurred during the first cabling trials of Cr⁺³ coated strands, where millimeter long chips of Cr/Cu appeared to accumulate at the forming die during first and second stage cabling, resulting in a galling-like effect that further enhanced the peeling (see figure 39(a)). Such peeling was not observed during the cabling of Cr⁺⁶ coated strands on the same equipment with the same setting (see figure 39(b)). A comprehensive program was carried out at the cabling supplier to study the effect of die size, die material, and strand angle at die

entrance. Eventually, a practical solution was found where very little to no dust is observed at the forming die and minimal scrapes or damages are observed on the cabled strands. This solution will be implemented for the cabling of the trivalent chromium plated strands (which has yet to be done). This problem, which hopefully has been resolved, is a reminder that it is not advisable to deviate from validated processes as it may have unanticipated consequences on subsequent manufacturing steps which may not be easily recovered.

In spite of these difficulties, and although there are some differences among suppliers, the eight TF strand productions, which have been completed or are very near completion, can all be considered as successful, in particular, those of the three new suppliers who started operation for the purpose of ITER. Instrumental to this success were the systematic low temperature measurements that were required from the suppliers and the verification measurements carried out by independent parties, whose sampling rate was modulated, depending on the production phases and the quality of production and of supplier data. The verification measurements led to the identification of issues that otherwise would have gone unnoticed. These were all the more critical given that, for most suppliers, the ITER TF strand productions were their first large scale productions of Nb₃Sn strands for

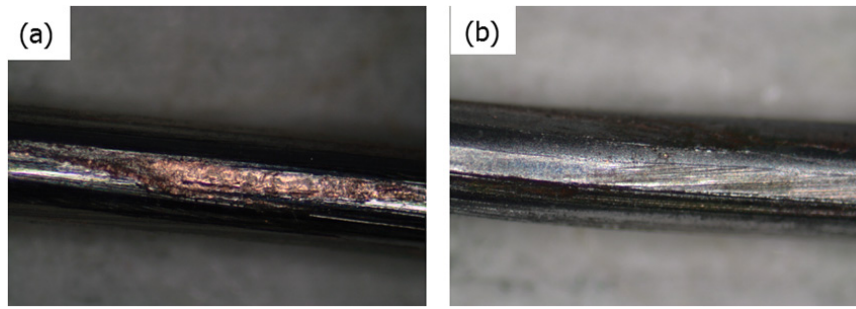


Figure 39. Examples of damages observed on the surface of Cr-plated IT Nb₃Sn strands as a result of cabling: (a) Cr⁺³ plated strand showing evidence of Cr/Cu peeling and (b) Cr⁺⁶ plated strand (courtesy of M Jewell and J Luhmann, University of Wisconsin at Eau Claire).

which much less experience was available than for Nb–Ti strands. Also critical was the organization by ITER-IO of several rounds of benchmarking of Nb₃Sn strand test facilities of all interested parties (suppliers and DA/ITER-IO reference laboratories) to ensure consistency of the measurements and of the corresponding acceptance criteria [32, 43].

In summary, the ITER project has enabled Nb₃Sn strand production to achieve a maturity comparable to that of Nb–Ti strand production and, hopefully, a higher cost efficiency that should spin off new markets.

5.1.2. Jacket sections. The jacket sections for the TF conductors are made up of modified 316LN (see table A.3) [18]. The mother heats are required to be subjected to an Electroslag Remelting (ESR) to limit the risk of macro-inclusions. The jacket sections are produced by hot extrusion followed by cold drawing and/or pilgering steps with some intermediate and a final solution annealing step. The final products are white-pickled or bright-annealed. Every jacket section is inspected by NDE techniques. Product analyses and detailed tests are also required on every jacket section lot, to check, among others, the grain size, ferrite content, and whether there are micro-inclusions and inter-granular corruptions. In particular, it is required to verify on the final product that the material is located in the austenite region above the 0% ferrite line in the Delong phase diagram [113] and that no ferrite traces are visible on micrographs at a magnification of 500×.

In addition, the PA defines requirements on the mechanical properties of the jacket sections at cryogenic temperatures. The measurements are carried out on samples of standardized geometry that have been prepared to be representative of the material state during coil operation. For TF, the standardization procedure to be applied to the jacket sections from which the mechanical samples are taken include: (1) compaction (by diameter reduction) to final dimensions, (2) stretching by 2.5% to mimic bending and straightening processes as experienced during coil winding and (3) heat treatment for 200 h at 650 °C in Argon or vacuum to mimic the reaction heat treatment of Nb₃Sn. The sub-size samples must be cut out of the jacket section by water jet or electrical discharge machining [114].

For TF jacket sections, the temperature/duration of the Nb₃Sn heat treatment are sufficient to produce some limited grain boundary sensitization. The latter, combined with the effect of cold work produced during compaction and

subsequent handling operations, can induce a loss of ductility at 4.2 K. Hence, it is critical to characterize the resulting level of embrittlement and to ensure that the material behavior is predominantly ductile in the stress range of interest. As the TF tube thickness (~2 mm) is too small to enable the preparation of suitable samples for fracture toughness (K_{IC}) and fracture crack growth rate (FCGR) measurements, it was decided to circumvent this difficulty by implementing a specification on the maximum elongation of at least 20% below 7 K. A micrographic examination of the fracture surfaces is also required so as to assess the extent of the dimple pattern zone, resulting from ductile fracture, and of the inter-granular surfaces, resulting from brittle fracture caused by grain boundary sensitization [115]. This is illustrated in figure 40 which shows examples of tensile test specimens cut out from TF jacket sections after compaction, stretching and ageing. Figure 40(a) illustrates a successful specimen, which features a shear fracture at a slant of approximately 45° and for which the broken surfaces exhibit a clear dimple shape that is consistent with a ductile fracture. The maximum elongation of this sample was above 20% and met PA requirements. Figure 40(b) illustrates an unsuccessful specimen, which broke with a flat fracture and for which the broken surfaces exhibit a clear pattern of intergranular fracture that reveals embrittlement. The maximum elongation of this sample was below 15% and did not meet PA requirements.

The qualification of TF jacket suppliers turned out to be a bigger challenge than anticipated, in particular due to the requirements on maximum elongation after compaction, stretching and ageing. At first, only three companies in the world were qualified: KSST in Japan [116, 117], POSCOSS in Korea [23, 118] and Jiuli in China [19, 119]. A European supplier, SMST, is now in the process of being qualified. The parameters influencing the maximum elongation have not yet been clearly identified, therefore, as for the superconducting strands, once a supplier has been qualified, the PA calls for a tight control of chemical composition and manufacturing processes. During production, maximum elongation measurements must be carried out on sub-size samples from every cast heat. Figure 41 presents a summary plot of these measurements for all the heats that have been used up to date across all six DAs. The data appear to meet the 20% specification. As for the strands, IO has organized a benchmarking of the various mechanical test facilities used by the DAs with KIT in Germany acting as the ITER-IO reference

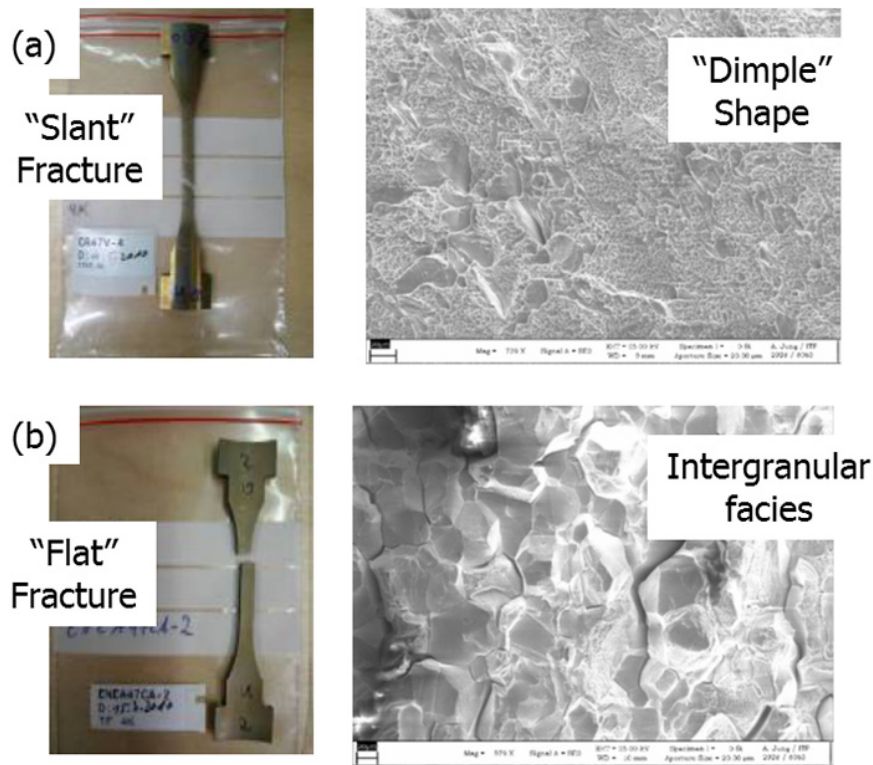


Figure 40. Examples of fracture features of the tensile test specimen cut from ITER TF tubes (after compaction, stretching and ageing): (a) sample with fully ductile fracture and maximum elongation above 20% and (b) sample exhibiting embrittlement and maximum elongation lower than 15% (courtesy of K Weiss, KIT).

laboratory [114]. The data of figure 41 show a reasonable agreement between KIT and DA measurements. The ITER-IO also funded a contract with the Kurchatov Institute in Moscow, Russia, to compare the results of mechanical tests on sub-size samples and full-size jackets, but more work would be needed to assess the reliability of the measurements on full-size jackets [120].

5.1.3. Conductors. As of November 2013, and in addition to 12 copper and superconducting qualification unit lengths, a total of 60×760 m regular Double Pancake unit lengths and of 24×415 m side Double Pancake unit lengths have been manufactured by JA, KO, RF, EU and CN (see figure 42). This corresponds to ~ 11 toroidal field Coils and more than half of the 133 TF conductor unit lengths that are required.

Two unexpected issues were encountered in the early stages of PA execution.

- (1) According to the conductor PA requirements, the orbital welding of the jacket sections must be carried out in accordance with the rules of ASME's Boiler and Pressure Vessel Code, sections VIII and IX (www.asme.org). This calls for welder certification and third party inspection of the welding process qualification.
- (2) According to EU regulations, for the conductor spools to be delivered to the EU, the lifting fixtures of the transportation jigs must be CE marked.

This caused long delays (up to one year) for two of the DAs who were lacking experience with these procedures.

As of today, three major incidents have been recorded during jacketing operations. At one supplier, the steel leader rope that is used to pull the superconducting cable inside the jacket assembly broke in the area of the grip between leader rope and sc cable after 680 m (out of 760 m) had been inserted. A cumbersome but clever rescue plan was developed. To avoid damaging the cable by de-inserting it from the tail end in a direction opposite to that of insertion (see figure 11), it is the whole jacket assembly that was pulled from the tail end. As a result, the friction forces generated between cable and jacket were in the same direction as during insertion. The operation was successful and after thorough inspection of the cable surface and outer dimension, it was agreed that the cable unit length could be reused for a subsequent insertion.

The other two incidents were more dramatic. In one case, a cleaning rag was left on the conductor jacket as it entered the compaction machine. This rag produced a large dent on the conductor surface. Fortunately, this conductor unit length was 760 m long (to be used for the winding of a regular double pancake or rDP) and the dent location enabled the supplier to salvage 415 m of good conductor (that could be used for the winding of a side double pancake or sDP). Hence, this rDP UL was converted into an sDP UL. In another case, a sudden increase of pulling force was observed during the insertion of an rDP cable into a jacket assembly after about 40 m had been inserted. The decision was taken to stop insertion and to de-insert the cable by pulling it in the opposite direction. The reason for this blockage was found to be a local waviness in the cable (whose diameter was otherwise within specifications). Attempts were made to correct this waviness (by re-taping

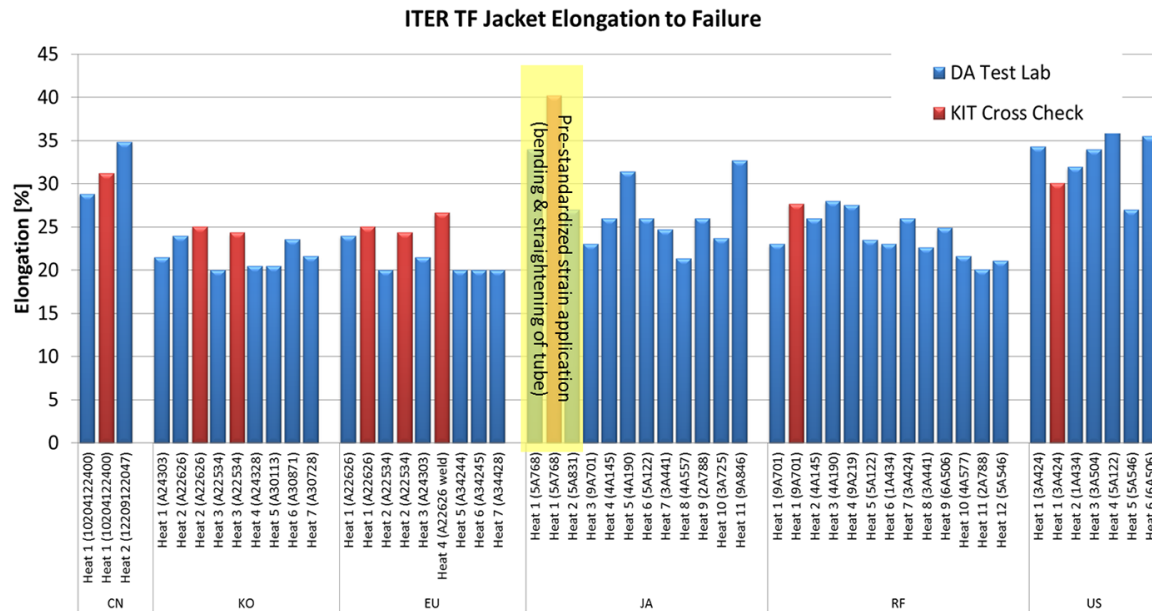


Figure 41. Summary plot of maximum elongation measured on tensile specimens issued from TF jacket samples at cryogenic temperature for the productions of all six DAs. The blue bars correspond to data from DA reference laboratory, while the red bars correspond to data from ITER-IO reference laboratory.

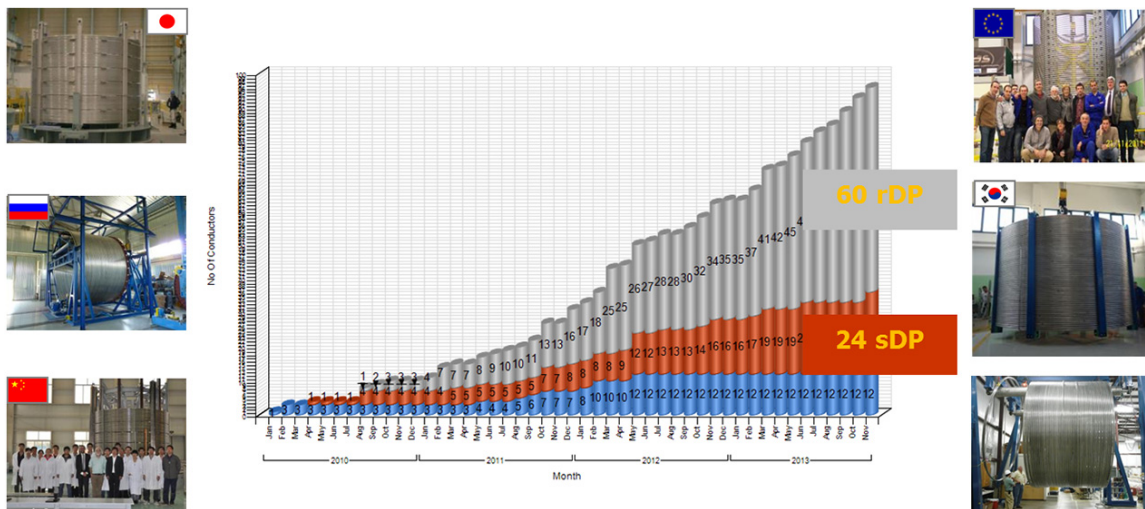


Figure 42. Dashboard of TF conductor registration into the ITER-IO conductor database, including 760 m long regular double pancake (rDP) and 415 m long side double pancake (sDP) unit lengths.

the stainless steel outer wrap), but they were unsuccessful and the cable UL had to be discarded. It should be noted that PA specification calls for the use of a go-no-go gauge of length 60 cm, oversized by 0.1 mm on the maximum allowable cable diameter to be applied prior to cable spooling so as to check for this kind of waviness, but the cabling company and the DA objected to the use of such go-no-go gauge and filed a deviation request, which, after long discussions, was eventually agreed by the ITER-IO. This is a reminder that technical requirements that have been developed over many years based on practical experience should not be neglected or tampered with.

Another recurrent issue has been that of cleanliness of conductor spools. Having full jacket assemblies laying for days or even weeks in the jacketing lines can result

in an accumulation of dust, insects and even droppings on the conductor surface. All conductor suppliers have now implemented several cleaning stations, usually before and after the compaction machine, to clean the conductor jacket. In addition, all delivery packages include sealing bags and a large amount of desiccant to protect the conductor spools during transportation and storage.

5.1.4. Conductor delivery and storage. ITER-IO acknowledged very early that conductor delivery packages were a critical interface between conductor supplier and coil manufacturer and organized, starting in August 2008, a series of meetings involving the six conductor DAs, the two TF coil DAs and, subsequently, their suppliers to discuss conductor

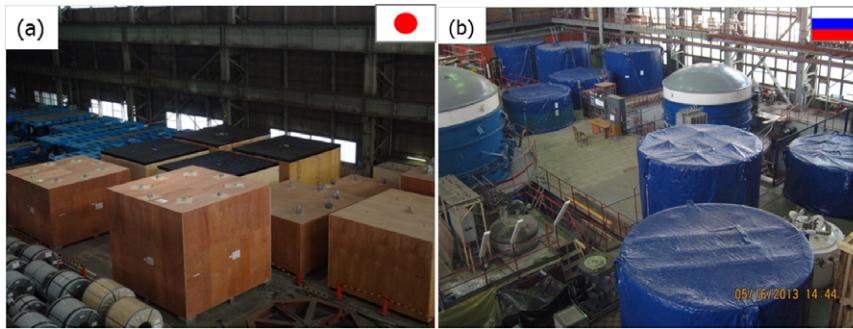


Figure 43. Storage of TF conductor ULs: (a) CN, KO and TF ULs in a warehouse rented by JAEA in Wakamatsu, Japan (left, courtesy of Y Nunoya, JAEA), (b) RF ULs at the Kurchatov Institute in Moscow, Russia (right, courtesy of V Tronza, RF-DA).

spooling and transportation. It was decided that each of the conductor DAs would generate a standard set of documents, including a design report for the transportation jig and package (with a stress analysis), 2D drawings, and an unpacking procedure to be reviewed by the relevant TF coil DA and approved by ITER-IO. The discussions went on until the spring of 2012, when the first delivery packages from CN, KO and RF were finally agreed with JAEA and Fusion for Energy (F4E, acronym for the European Domestic Agency). One of the reasons why discussions amongst all of the stakeholders took so long is that the conductor DAs, with suppliers in full production and clear requirements, were well ahead of the TF coil DAs, whose contracts with TF coil suppliers were barely in place and constraints at that end still needed to be agreed.

The ITER-IO efforts on defining and standardizing requirements for conductor delivery packages did not prevent an interface issue from arising during the early stage of deliveries from one of the TF conductor suppliers to one of the TF coil manufacturers. The unspooler installed at this TF coil manufacturer was designed with the assumption of a cylindricity tolerance on the conductor spool of ± 3 mm, which is much tighter than the alignment specified to the conductor suppliers (inner spool diameter of $4 \text{ m} \pm 30 \text{ mm}$). The unspooler jammed in early trials. A review by an independent tooling expert confirmed the risks of conductor jamming and offered several options to cope with this problem at a minimum cost. This issue became the object of several months of discussion between all parties involved (the DAs responsible for TF conductor deliveries and their suppliers, the DA responsible for TF coil manufacture and its supplier as well as the ITER-IO) and provides a good example of the management challenges faced at ITER due to its governance structure and unique in-kind procurement system. It is now being resolved, with improvements being implemented to the unspooler and better alignment being achieved by the conductor suppliers (down to ± 6 mm on the radius).

Outside of this issue, deliveries of TF conductor ULs to TF coil suppliers are now taking place on a regular basis but still remain a logistical challenge. This is particularly true for CN, who is required to deliver TF conductor ULs to both F4E and JA, and for KO, whose cables and jacket sections are manufactured in KO before being shipped to EU for jacketing, then, the jacketed conductor spools are shipped back from EU to KO before final delivery to JA.

Overall, TF conductors, for which all industrial contracts have been placed and are running at full speed, are produced at a faster pace than they can be used for winding. The need for storage space was identified very early by JAEA who has been renting a warehouse in Wakamatsu (near the NSSE jacketing line) since May 2010. This warehouse, depicted in figure 43(a), is used to store conductor unit lengths delivered from CN, JA and KO and destined to coil winding in Japan. Figure 43(b) shows the RF conductor unit lengths which are kept at the Kurchatov Institute in Moscow awaiting shipment to the coil manufacturer.

5.2. CS conductor production

5.2.1. Strands. As already mentioned, JAEA has placed contracts for the manufacture of cables for four modules of the CS coil stack. Each module requires one 613 m quadri-pancake (qP) and six 918 m hexa-pancake (hP) unit lengths. Contracts for the remaining modules will be placed in the next Japanese fiscal year, starting in April 2014.

Contracts for the first two modules were awarded to Jastec in Japan (in consortium with Mitsubishi Cable), who has developed third generation Nb_3Sn bronze strands with I_C in excess of 260 A, comparable and even higher than the I_C of IT Nb_3Sn strands for ITER [77]. As illustrated in figure 44, about 17 t of Jastec CS strands have already been registered into the ITER conductor database. The strand production for the first module will be completed in December 2013 and cabling of these strands will be completed in March 2014. As discussed in section 4.3.10, there were some initial issues with cabling deformation, but the process is now under control.

A contract for the third module was awarded to Furukawa Electric in Japan, who has also developed third generation Nb_3Sn bronze strands with properties similar to that of the Jastec strands and who has already carried out cabling optimization to limit strand deformation. A contract for the fourth module was awarded to KAT in Korea (in consortium with Nexans Korea). KAT will rely on internal tin strands. The selected strand design is the one that was used in the leg of the CSKO1 SULTAN sample that achieved the highest T_{CS} (see section 4.3.5). However, as already explained in section 4.3.10, KAT and Nexans Korea have yet to carry out cabling and strand deformation optimization.

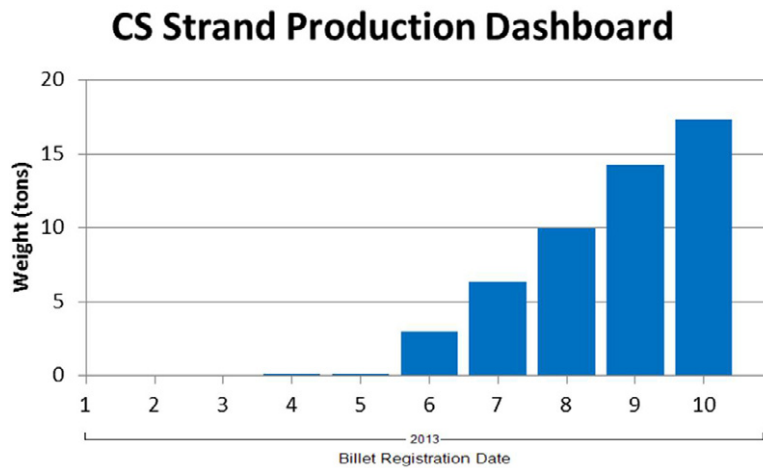


Figure 44. Dashboard of CS Nb₃Sn strand billet registration into the ITER-IO conductor database: (in metric tons).

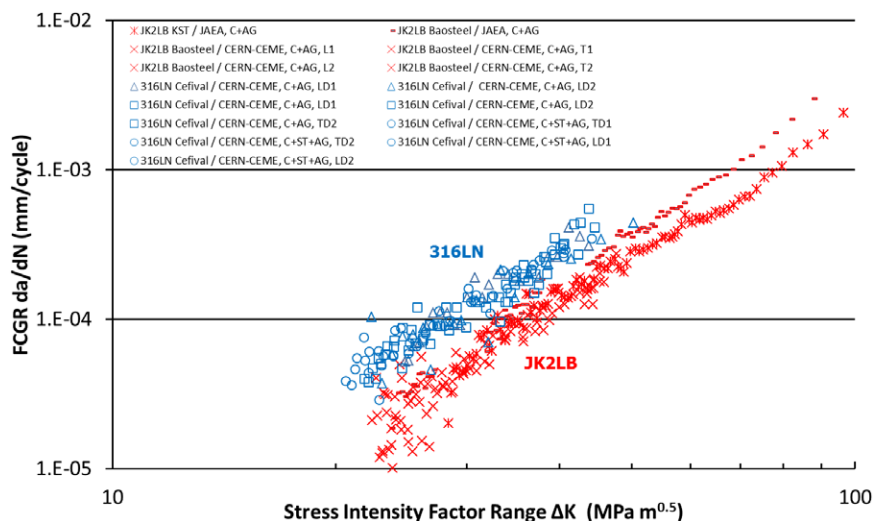


Figure 45. Summary plot of FCGR measurements on specimens cut from compacted and aged 316LN and JK2LB jacket sections produced for ITER CS (courtesy of I Pong, LBNL).

5.2.2. Jacket material. The CS conductors rely on a circle-in-square jacket. In the 2000s, JAEA, together with Kobe Steel, LTD, developed a special grade of austenitic steel with high manganese and low carbon contents and boron addition, referred to as JK2LB (see table A.3 of the appendix). JK2LB has a lower integrated thermal shrinkage coefficient between room temperature and 4.2 K than that of conventional 316LN [121, 122]. Utilizing the thermal shrinkage differential between the conductor jacket, made up of JK2LB, and the so-called tie plates, made up of forged NITRONIC® 50 (F XM-19), featuring an integral thermal contraction between room temperature and 4.2 K similar to the one of 316LN [123], enables the application of a suitable axial pre-compression to the CS coil stack at the end of cooldown without overstressing the tie plates at room temperature [124].

Nevertheless, in 2008–2009, at the time of CS conductor PA signature, there were concerns that the production costs of JK2LB might be prohibitive. Therefore, ITER-IO decided to revisit the issue of modified 316LN versus JK2LB and

launched an R&D program with Baosteel in China and Cefival in France to compare manufacturing costs and mechanical properties at cryogenics temperature [125]. The low temperature mechanical measurements included fatigue crack growth rate (FCGR) on standardized specimens cut from compacted and aged jacket sections. Figure 45 presents a compilation of available and relevant FCGR data for both 316LN and JK2LB jacket specimens [126–129]. The data of figure 45 clearly show that JK2LB has a slower FCGR than modified 316LN and confirm that it is a more suitable candidate for CS jacket material. A side benefit of the ITER-IO program is that it also helped to demonstrate that the production costs of JK2LB were not significantly higher than those of 316LN and the decision was made by ITER-IO in December 2011 to select JK2LB for the CS jacket. The manufacture of the CS conductors will require about 500 t and more than 5000 JK2LB jacket sections.

Let us note that in the early stages of JK2LB development there were some speculations about possible precipitation of

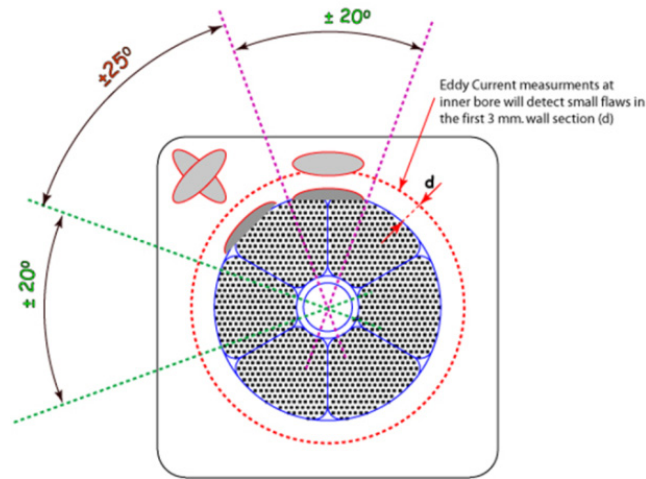


Figure 46. Location of defects considered in LEFM computations for circle-in-square jackets.

intermediate phases such a σ phase as a result of the long heat treatment (required for Nb_3Sn reaction) that could cause embrittlement. However, in its final version, the chemical composition of JK2LB features relatively low Cr and Mo, ESR is systematically applied to minimize the risks of segregations and the grade does not present observable presence of δ -ferrite in the solution annealed state, which, together, concur in mitigating the risk of precipitation of intermediate phases. It was also established that σ phase was not a major factor of fracture toughness degradation and that the main causes of embrittlement remained precipitation of carbides (M_{23}C_6) and nitrides. Hence, nitrogen and carbon contents were optimized allowing fracture toughness to be improved. There were also some fears that the process was not scalable to industrial production, but two suppliers have demonstrated it could be done.

One manufacturing issue is that JK2LB has a tendency to form Mn oxides during high temperature processing (if carried out in air) including final annealing that are thicker and more difficult to remove than oxide layers formed on standard AISI 300 series stainless steel grades. This calls for a more severe pickling that can induce a coarser roughness on the jacket section's inner and outer surfaces and a reduction in wall thickness. The annealing heat treatment temperature and duration are optimized to limit the amount of oxidation while achieving the desired grain size. Moreover, upon completion of the final solution annealing and pickling, a skin pass drawing is applied to achieve the desired tolerance on cross-sectional dimensions and to aim at the specified surface roughness.

5.2.3. Maximum flaw sizes and jacket section NDE. As for the superconducting cables, the CS jacket sections and welds will have to sustain a large number of stress cycles. A very thorny issue has been the assessment of the maximum allowable defect sizes. This assessment is carried out by relying on linear elastic fracture mechanics (LEFM) analyses. It requires distinguishing between sub-surface and embedded defects and it depends on the defect location (thin wall or corner area

Table 2. Maximum allowable defect sizes computed by LEFM for the conductor jacket assemblies in the various CS modules as a function of defect location. 'd' represents the depth to the edge of the flaw with respect to either the cable-side or jacket outer surface; any surface flaw has $d = 0$. CS3L pancakes are numbered from the bottom of the module (courtesy of C Jong, ITER-IO, and K Freudenberg, L Myatt, K Cochran, US-IPO).

Module (pancake)	Surface or sub-surface ($d < 3$) (mm^2)	Embedded ($d > 3$ mm) (mm^2)
(a) Max defect area, thin-wall region $\pm 20^\circ$		
CS1/CS2/CS3U	2	5
CS3L (P7–P40)	7	12
CS3L (P1–P6)	17	20
(b) Max defect area, corner region $\pm 25^\circ$		
CS1/CS2/CS3U	3	7
CS3L (P7–P40)	10	16
CS3L (P1–P6)	20	30

of the circle-in-square jacket). In the assessment, the effect of important assumptions about the stress state, like residual stresses and mean stress corrections (Walker coefficient), have been investigated and determined [130–132]. Figure 46 and table 2 summarize the maximum allowable defect sizes computed by LEFM analyses as a function of defect position in the jacket section for the different modules of the CS coil stack [133]. Defects are assumed to be planar (no volume) and are perpendicular to the hoop stress (winding direction). The data reported here include a safety factor of 2 on the number of cycles and on the defect size and a safety factor of 1.5 on K_{IC} . The results are similar for base material and welds.

Of course, the CS jacket sections and CS welds must be subjected to a non-destructive examination (NDE) which, ideally, should have a good enough resolution to detect defects of the size listed in table 2. This is relatively easy for the welds, where conventional x-ray methods are good enough to achieve

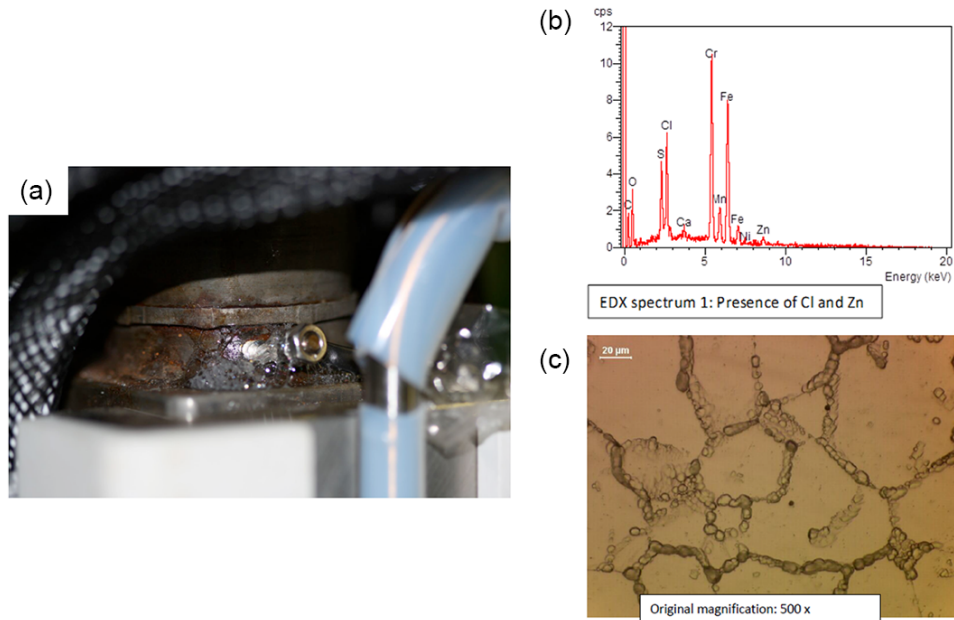


Figure 47. (a) Evidence of an He leak near the crimping rings of one leg of CSJA2 (left, courtesy of P Bruzzone, CRPP), (b) evidence of Cl and Zn contamination in the rust residues removed from the leaking area of the test sample. Moreover, microstructural observations confirmed that the material of the conduit is in a slightly sensitized state, with evidence of ditch structure (c) revealed by the oxalic acid etch test (courtesy of S Gobba, CERN).

the required resolution, but it is far more difficult for the base material, in particular, in the corner areas.

At present, the NDE inspection of the CS jacket sections for the CS3L module includes a combination of phase array ultrasonic testing (PAUT) for the material bulk [126, 134] and of eddy current testing (ET) for the first 2–3 mm from the inner bore of the jacket section. The PAUT inspection is well suited for the detection of the most critical defects which, in pipes of relatively large cross-sectional area and thickness, are expected to arise from internal longitudinal stresses provoking delamination [135], with a main component parallel to the maximum flow of the material, i.e., in the extrusion and drawing direction. This was confirmed by the experience developed from the CS circle-in-square jacket productions to date, where the most relevant extrusion defects have been generally identified in the bulk of the pipes with a main component parallel to the extrusion direction [136]. The ET inspection is well suited for the detection of surface defects in the extrusion process which may arise from different origins, such as improper surface quality of the billet, imperfect lubrication and excessive extrusion temperature and/or extrusion speed. However, the combined PAUT/ET inspection does not provide a full proof inspection against embedded transverse defects in the corner areas, but the likelihood of such defects in high purity austenitic steel having been subjected to an ESR is deemed to be very small as such flaws are more likely to develop from the interaction with the die on the surface of the material. Moreover, they are generally not single and isolated but occur in a portion of the extrusion where critical conditions have been met: hence, the probability that they are detected is higher than for a single isolated defect. The optimization of the NDE procedures was

quite cumbersome and was carried out with the support of CERN and ISQ in Portugal.

For jacket sections to be used in other modules beyond CS3L, investigations are underway to develop an EC system to inspect the outer surfaces of the jacket section and several methods are under consideration to inspect the corner areas, such as dual sensor UT (relying on a sender and a receiver probe on different surfaces) or conventional x-ray (but the latter could only be applied on a statistical sample, e.g., one jacket section per ESR).

5.2.4. Corrosion effects. It should be noted that JK2LB has one disadvantage: due to its low Cr, Ni and Mo content, it has limited alloying elements conferring corrosion resistance. As a result, exposures to halogen elements (such as HCl for Cr plating removal or ZnCl based soldering flux) should be prevented at all times during conductor/coil manufacture.

The sensitivity to corrosion was demonstrated by the first two CS conductor samples (CSJA1, prepared in Japan, and CSJA2 prepared at CRPP), which rely on conductors with JK2LB jacket, and which developed a leak during cold testing. In both cases, the leak happened 6 months to one year after sample manufacture, in an area of stress concentration in the JK2LB material which is likely to have been exposed to halogen fumes prior to Nb₃Sn heat treatment. As illustrated in figure 47, the combination of high stress, corrosive contamination and high temperature heat treatment is believed to have resulted in the initiation of a crack that slowly propagated by stress corrosion cracking along the grain boundaries of JK2LB and, after many months, resulted in a helium leak.

After these two incidents, great care was taken during subsequent sample preparations at CRPP to avoid any kind

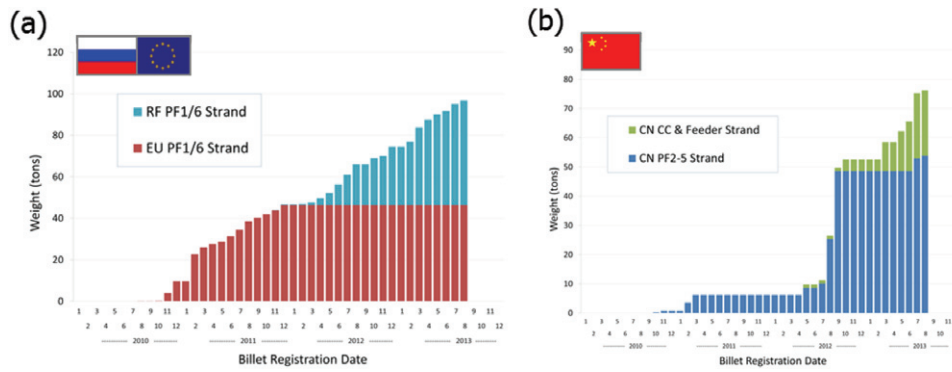


Figure 48. Dashboard of Nb–Ti strand billet registration into the ITER-IO conductor database: (a) strand type 1 for PF1 and 6, (b) strand type 2 for PF2-5, CC, MB and CB (in metric tons).

of corrosion and none of the subsequent samples developed a leak. This critical issue should be kept in mind during the manufacture of the CS coil modules at the supplier and during the on-site assembly and installation of the CS coil stack in the tokamak.

5.2.5. Conductors. NSSE has presently completed the manufacture of the process qualification unit lengths and is now proceeding with the welding and jacketing of the first ~600 m quadri-pancake unit length.

5.3. PF conductor production

Nb–Ti strand types 1 and 2 have been qualified for use in PF conductors through the successful testing of SULTAN samples [137, 138]. For these samples, which were prepared by a consortium made up of ENEA Frascati, in Italy, and CEA Cadarache, in France, the bottom joint was replaced by a hairpin to limit the risk of non-uniform current distributions that may arise from the joint [139], and that were believed to be at the origin of the premature quenching observed on previous high current, Nb–Ti SULTAN samples [140].

As illustrated in figure 48(a), RF and F4E have registered ~95 t of Nb–Ti strand type 1 (out of the required 110 t) into the conductor database. RF is in full cable production and F4E is in the process qualification phase for PF1 and PF6 conductor jacketing.

In the meantime and as illustrated in figure 48(b), CN has registered nearly ~78 t of Nb–Ti strand type 2 into the conductor database, including 55 t out of the required 155 t for PF2-5. In addition, CN has completed the manufacture of all process qualification unit lengths and is proceeding with the production of PF5 and PF2-4 conductors. Figure 49 shows pictures of the 740 m PF5 copper dummy UL and of the 910 m PF2-4 Cu dummy UL. The PF5 copper dummy was delivered (in three sections) to the ITER site on 3 June 2013; this was the very first delivery of a component to ITER.

The PF jacket sections are circle-in-square and are made up of modified 316L (see table A.3 of the appendix). They are produced by two suppliers: SMST in EU and Jiuli in CN. Similarly to the CS coil stack, the PF coils are pulsed and the PF conductor jackets and welds must be able to sustain a large number of stress cycles. LEFM analyses have been carried

Table 3. Maximum allowable defect sizes computed by LEFM for the PF conductor jackets and welds as a function of defect location. ‘d’ represents the depth to the edge of the flaw with respect to either the cable-side or jacket outer surface; any surface flaw has d = 0. The angular location refers to figure 46.

	Surface or sub-surface (d < 3) (mm ²)	Embedded (d > 3 mm) (mm ²)
(a) Max defect area, thin-wall region ±20°		
Base metal	10	11
Weld metal	7	7
(b) Max defect area, corner region ±25°		
Base metal	15	20
Weld metal	13	15

out to determine the maximum flaw sizes that are acceptable. The results are summarized in table 3. As for CS, defects are assumed to be planar (no volume) and perpendicular to the hoop stress (winding direction); the values in table 3 include a safety factor of 2 on the number of cycles and on the defect size and a safety factor of 1.5 on K_{IC}. The values are different for base material and welds (due to differences in the measured mechanical properties of weld samples) and, for the base material, are similar to those of the CS3L module (compare tables 2 and 3).

The PF jacket sections are subjected systematic to non-destructive examination. As for the CS jackets, the present NDE procedure is based on PAUT and discussions are underway to add an EC inspection of the jacket section inner surface. Figure 50 shows the three probes used in CN to carry out the PAUT of the PF2-5 jacket sections. As for all suppliers, the PAUT inspection is carried out in water immersion. Let us note that both PF jacket suppliers rely on creeping waves to inspect the jacket outer surface, thereby eliminating the need for an additional EC inspection as in the case of the CS jacket supplier.

The acceptance of PF jacket sections also call for mechanical tests at cryogenic temperatures similar to those required for the CS jacket sections. For PF, the standardization procedure to be applied to the jacket section prior to cutting specimens is: (1) compaction to final dimensions and (2)



Figure 49. Views of first PF conductor ULs manufactured in China: (a) 740 m long Cu dummy UL and (b) 910 m long Cu dummy UL (courtesy of Y Wu, ASIPP).



Figure 50. PAUT probes used at ASIPP for the NDE inspection of the PF2-5 jackets in water immersion (courtesy of J Qin, ASIPP).

bending on a radius of 2 m and straightening to simulate unspooling and coil winding operation. Mechanical test results are summarized in [114, 141, 142].

The PF conductor production in CN and EU relies on the same jacketing facilities as the TF conductors, with dedicated welding stations and sturdier compaction machines.

5.4. Other Nb–Ti conductors

Strand type 2 has also been qualified for use in CC and CB conductors by means of SULTAN samples relying on the same hairpin configuration as for PF conductors (see section 5.3) [138]. Some difficulties were encountered with MB conductor qualification. After several unsuccessful trials, an additional SULTAN sample was assembled at CRPP using a configuration similar to that of the TF samples (two legs connected by solder-filled bottom joint and upper terminations). This new MB sample was tested in December

2013 and exceeded the T_{CS} requirement of 6.7 K at 45.5 kA in a SULTAN background field of 3.22 T by nearly 0.3 K. In addition, the sample was stable as a function of EM cycling (as expected for a Nb–Ti sample) and its performance conform to expectations from scaling of the strand performance. This successfully completes feeder conductor qualification.

CN has completed the production of the ~23 t of Nb–Ti strand type 2 required for CC (see figure 48(b)) and is now proceeding with the production of CC and feeder conductors, relying on the same jacketing line as for TF and PF conductors at ASIPP.

6. Conclusion

The ITER project offers many technical and management challenges but is an incredible human adventure and will become a milestone in the history of science. In spite of a

difficult environment and tough constraints, but thanks to a good collaborative spirit and mutual trust and understanding at the technical level, the ITER conductor production is moving forward in all six ITER members involved (CN, EU, JA, KO, RF and US).

TF conductors are well into production, with ~95% of the required Nb₃Sn strands and more than half of the conductor unit lengths already completed. PF strand and conductor productions have been launched in RF/EU and CN; the first PF5 copper dummy conductor has been delivered from China to the ITER site in June 2013 and the first PF1 pre-dummy conductor has been delivered from EU to RF. CC, CB and MB conductors are also in the production phase. A technical solution has been found for the challenging CS conductors and the production for the bottom module of the CS coil stack module (CS3L) is underway.

As ITER conductor production is reaching its peak, the focus of the activities will naturally shift to coil manufacture. Let us hope that the ITER partners involved in this work will be animated by the same desire to transcend their domestic constraints and cultural habits so as to pursue the noble goal of bringing together the people of the world to build the ITER machine and, beyond, develop a safe, clean and sustainable energy source.

Acknowledgments

The authors wish to warmly thank their collaborators around the world who make this work possible, including: L Delong, E Niu, H Li, S Liu and M Wang (CN-DA), C Li, Qin and Y Wu (ASIPP), T Boutboul, P Readman and E Viladiu (F4E), A della Corte, A di Zenobio, L Muzzi and S Turtu (ICAS), K Hamada (now at ITER IO), T Isono, Y Nabara, Y Nunoya, K Okuno, H Ozeki and Y Takahashi (JAEA), K Jung, K Kim, S P Kwon and S H Park (NFRI), A Krasilnikov, D Kravtsov, S Lelekhov, V Pantsyrny and V Tronza (RF-DA),

L Potanina and V Vysotsky (VNIIEP), K Chan, N Martovetsky and W Reiersen (US-IPO), T Painter (HPM) and J Parrel (OST). The authors are indebted to S Sgobba (CERN) for his reactivity, dedication and in depth knowledge of the properties, manufacturing processes and inspection techniques of steel products and to P Bruzzone, B Stepanov and the technical crew at CRPP for SULTAN sample preparation and tests. The authors also wish to thank the design reconciliation dream team: D Ciazynski and A Torre (CEA), H Bajas (CERN), C Calzolaio (CRPP), V Aubin and D Durville (ECP), D Larbalestier, P Lee and C Sanabria (Florida State University), A Nijhuis, G Rolando and C Zhou (Twente University), M Breschi (University of Bologna) and M Jewell (University of Wisconsin at Eau Claire) for their continuous and innovative contributions. Special thanks to D Leroy (formerly from CERN), who was instrumental in developing and reviewing technical requirements, and to A Ghosh (BNL), B Turck (formerly from CEA), B Strauss (US-DOE) and A Yamamoto (KEK), eminent members of the External Conductor Procurement Review Committee, who helped drafting procurement arrangements and defining QA/QC requirements. Finally, this work would not have been possible without the active management support of G Johnson (2007–2010) and R Haange (2011–2013) and the mothering of C Foucher de Brandois, C Gregory and M O’loughlin.

Disclaimer. The views and opinions expressed herein do not necessarily reflect those of the ITER Organization.

Appendix. ITER conductor parameters

The enclosed tables summarize the most salient and up to date (December 2013) ITER conductor parameters.

For CS, there are two slightly different conductor designs. The IT conductors rely on the CSIO design that was qualified by the CSIO2 STP and CSK01 SULTAN samples, while the bronze conductors rely on the CSJA design that was

Table A.1. Salient parameters of ITER strands.

	TF	CSIO	CSJA	S1	S2
SC type	Nb ₃ Sn	Nb ₃ Sn	Nb ₃ Sn	Nb–Ti	Nb–Ti
Plating type	Cr	Cr	Cr	Ni	Ni
Outer diameter ^a (mm)	0.820	0.820	0.830	0.730	0.730
Plating thickness (μm)	2	2	2	2	2
Twist pitch (mm)	15	15	15	15	15
Cu-to-non-Cu ratio ^a	1.0	1.0	1.0	1.64	2.33
Residual resistivity ratio ^a	>100 ^b	>100 ^b	>100 ^b	>100	>100
Reference field, B_{ref} (T)	12	12	12	6.4	5.0
Min. critical current ^{a,c} (A)	190–250 ^d	260	260	306	339
Resistive transition index ^{a,c}	>20	>20	>20	>20	>20
Reference field cycle (T)	±3	±3	±3	±1.5	±1.5
Max. hysteresis loss ^e (mJ cm ⁻³)	500	500	500	55	45

^a Plated strands.

^b After heat treatment.

^c On ITER barrel at 4.22 K and B_{ref} .

^d Depending upon supplier.

^e Per strand unit volume at 4.22 K and for reference cycle.

Table A.2. Salient parameters of ITER cables.

Parameter	TF	CSIO	CSJA	PF					CC	MB	CB
				L1 (1 and 6)	L2 (2-4)	L3 (5)					
SC stand type	TF	CSIO	CSJA	S1	S2	S2	S2	S2	S2	S2	
Segregated copper				N/a				N/a			
Strand (Cu)	0.820 mm (3 × 4 Cu)	0.820 mm	0.830 mm	—	0.730 mm	N/a	N/a	0.730 mm (3 × 4Cu)	0.730 mm	0.730 mm	
Core 1 (C1)	N/a	N/a	N/a	—	1.200 mm	N/a	N/a	2.0 mm	N/a	N/a	
Core 2 (C2)	N/a	N/a	N/a	—	2.700 mm	N/a	N/a	1 + 6 + 12 + 18 + 24 rope with C2	N/a	N/a	
Core 3 (C3)	N/a	N/a	N/a	—	N/a	2.850 mm	—	—	—	—	
Petal wrap (mm)											
Thick. × width	0.1 × (12-15) ^a	0.10 × (12-15) ^a	0.08 × (15-20) ^a	0.05 × 20	0.05 × 20	0.05 × 20	—	N/a	N/a	N/a	
Coverage (%)	50	70	70	50	50	50	—	—	—	—	
Cable wrap (mm)											
Thick. × width	0.1 × 40	0.08 × 32	0.08 × 32	0.1 × 40	0.1 × 40	0.1 × 40	0.1 × 40	0.1 × 40	0.1 × 40	0.1 × 20	
Overlap (%)	40	40	40	40	40	40	40	40	40	40	
Central spiral (mm)											
Thick. × width	1 × 6	1 × 6	1 × 6	1 × 6	1 × 6	1 × 6	1 × 6	—	—	0.5 × 6	
Out. dia. × pitch	10 × 9.0	10 × 9.0	9 × 8.85	12 × 8.85	12 × 8.85	12 × 8.85	12 × 8.85	—	—	6 × 9.9	
Petal layout	(2 SC + 1 Cu) × 3 × 5 × 5 + 1 C1	(2 SC + 1 Cu) × 3 × 4 × 4	(2 SC + 1 Cu) × 3 × 4 × 4	3 SC × 4 × 4 × 5	[(2 SC + 1 Cu) × 3 × 4 + 1 C1] × 5 + 1 C2	(3 SC × 4 × 4 × 4) + 1 C3	3 SC × 4 × 5	(2 SC + 1 Cu) × 3 × 5 × (5 + 1 C1)	(2 SC + 1 Cu) × 3 × 3 × 3	(2 SC + 1 Cu) × 3 × 3 × 3	
Final cable layout	6 petals around spiral	6 petals around spiral	6 petals around spiral	6 petals around spiral	6 petals around spiral	6 petals around spiral	5 petals twisted	6 petals around C3	4 petals around spiral	4 petals around spiral	
Twist pitches (mm)											
First stage	80	20	20	45	45	45	45	45	45	42	
Second stage	140	45	45	85	85	85	85	85	85	70	
Third stage	190	80	80	145	145	145	145	145	145	122	
Fourth stage	300	150	150	250	250	250	250	250	250	182	
Final stage	420	450	450	450	450	450	450	450	450	250	

^a Depending upon supplier.

Table A.3. Chemical compositions of base materials for ITER jacket sections (wt%).

	TF	CS	PF	CC, MB and CB
Type	Mod. 316LN	JK2LB	Mod. 316L	AISI 316L or (316LN)
C	<0.02 target: <0.015	≤0.030 target: <0.025	≤0.030	≤0.030
Si	<0.75	≤0.50 target: <0.28	≤0.75	≤0.75
Mn	<2.0	20.50–22.50	≤2.00	≤2.00
P	<0.04	≤0.015 target: <0.008	≤0.03	≤0.045
S	<0.03	≤0.015 target: <0.008	≤0.01	≤0.030
Cr	16.0–18.0	12.00–14.00	16.00–18.50	16.0–18.0
Ni	11.0–14.0	8.0–10.0	11.0–14.0	10.0–14.0
Mo	2.0–3.0	0.5–1.5	2.00–2.50	2.00–3.00
N	0.14–0.18	0.09–0.15	—	(0.10–0.16) ^a
B	—	0.0010–0.0040	—	—
Co	<0.1	<0.1	≤0.10	—

^a N content specification only applies to 316LN.

Table A.4. Salient parameters of ITER conductors.

Coil	Shape	Main outer dimension (mm)	Target jacket inner diameter ^a (mm)	Target central spiral inner diameter ^a (mm)
TF	Circular	43.7	39.7	7.9–8.1
CSJA	Circle-in square	49.0 × 49.0	32.6	6.8–7.2
CSIO	Circle-in square	49.0 × 49.0	32.6	7.9–8.1
PF1&6	Circle-in square	53.8 × 53.8	37.7	9.8–10.2
PF2-5	Circle-in square	51.9 × 51.9	35.3	9.8–10.2
CC	Square	19.2 × 19.2	14.8 × 14.8	N/a
MB	Circular	44.5	40.5	N/a ^b
CB	Circular	22.0	18.0	5.0

^a After compaction.

^b Target copper core C3 outer diameter: 18.5 mm.

qualified by the CSJA3 and CSJA5 SULTAN samples. The main differences are: (1) the strand diameter (0.82 mm versus 0.83 mm) and (2) the spiral diameter (9 mm versus 10 mm). This may result in different thermal-hydraulic impedances between modules that will have to be corrected during operation.

For Nb–Ti, strand S1 is used for PF1 and six conductors, while strand S2 is used for PF2-5, CC, MB and CB conductors. L1 refers to the cable layout for PF1 and six conductors, L2 to that for PF2-4 conductors and L3 to that for PF5 conductors.

References

- [1] Ikeda K 2010 ITER on the road to fusion energy *Nucl. Fusion* **50** 014002
- [2] Clery D 2013 *A Piece of the Sun: the Quest for Fusion Energy* (London, NY: Overlook Press)
- [3] Holtkamp N 2009 The status of the ITER design *Fusion Eng. Des.* **84** 98–105
- [4] Mitchell N et al 2008 The ITER magnet system *IEEE Trans. Appl. Supercond.* **18** 435–40
- [5] Bonito Oliva A et al 2014 Progress in the F4E procurement of the EU ITER TF coils *IEEE Trans. Appl. Supercond.* **24** 4202306
- [6] Koizumi N et al 2012 Development of ITER TF coil in Japan *IEEE Trans. Appl. Supercond.* **22** 4200404
- [7] Libeyre P et al 2014 Moving towards manufacture of the ITER central solenoid *IEEE Trans. Appl. Supercond.* **24** 4200605
- [8] Lim B S et al 2012 Development of the ITER PF coils *IEEE Trans. Appl. Supercond.* **22** 4201404
- [9] Wei J et al 2014 Progress of the ITER correction coils in China *IEEE Trans. Appl. Supercond.* **24** 4202005
- [10] Lu K et al 2014 Progress of the ITER feeder in China *IEEE Trans. Appl. Supercond.* **24** 4801504
- [11] Heller R et al 2004 Design and fabrication of a 68 kA current lead using Ag/Au stabilized Bi-2223 tapes as a demonstrator for the ITER TF-coil system *IEEE Trans. Appl. Supercond.* **14** 1774–7
- [12] Heller R et al 2005 Experimental results of a 68 kA high temperature superconductor current lead demonstrator for the ITER magnet system *IEEE Trans. Appl. Supercond.* **15** 1496–9
- [13] Ballarino A et al 2012 Design of the HTS current leads for ITER *IEEE Trans. Appl. Supercond.* **22** 4800304
- [14] Ballarino A 2008 Large-capacity current leads *Physica C* **468** 2143–8
- [15] Denz R et al 2014 Upgrade of the protection system for the superconducting elements of the LHC during LS1 *IEEE Trans. Appl. Supercond.* **24** 4000604

- [16] Coetana M *et al* 2010 Quench detection in the ITER magnet system LS1 *IEEE Trans. Appl. Supercond.* **20** 427–30
- [17] Hoenig M O and Montgomery D B 1975 Dense supercritical-helium cooled superconductors for large high field stabilized magnets *IEEE Trans. Magn.* **11** 569–72
- [18] Devred A *et al* 2012 Status of ITER conductor development and production *IEEE Trans. Appl. Supercond.* **22** 4804909
- [19] Wu Y *et al* 2013 Manufacturing of the ITER conductors in China *IEEE Trans. Appl. Supercond.* **23** 4802004
- [20] Liu S *et al* 2014 Progress on TF and PF conductor for ITER in China *IEEE Trans. Appl. Supercond.* **24** 4802904
- [21] Boutboul T *et al* 2014 Status of the procurement of the European superconductors for the ITER magnets *IEEE Trans. Appl. Supercond.* **24** 6001004
- [22] Takahashi Y *et al* 2011 Technology development and mass production of Nb₃Sn conductors for ITER toroidal field coils in Japan *Nucl. Fusion* **51** 11 113015
- [23] Park S H *et al* 2014 Overview of conductor production for ITER toroidal field magnet in Korea *IEEE Trans. Appl. Supercond.* **24** 4800905
- [24] Vysotsky V S *et al* 2012 Status and achievements in production of ITER TF conductors and PF cables in Russian cable institute production *IEEE Trans. Appl. Supercond.* **22** 4200505
- [25] Devred A *et al* 2013 Conductor qualification program for the ITER central solenoid *IEEE Trans. Appl. Supercond.* **23** 6001208
- [26] Li H *et al* 2014 Qualification of the ITER correction coils and their conductor *IEEE Trans. Appl. Supercond.* **24** 4201904
- [27] Qin J *et al* 2013 Manufacture of ITER feeder sample conductors *Fusion Eng. Des.* **88** 1461–4
- [28] Pantisyrny V *et al* 2008 Nb₃Sn material development in Russia *Cryogenics* **48** 354–70
- [29] Park P and Kim K 2008 Status of Nb₃Sn strand development in Korea *Cryogenics* **48** 347–53
- [30] Li C G 2010 Investigation of superconducting properties of Nb₃Sn strands by internal tin process for ITER *IEEE Trans. Appl. Supercond.* **20** 1484–7
- [31] Liu W T *et al* 2010 Development of fine filament NbTi superconducting strands for ITER *IEEE Trans. Appl. Supercond.* **20** 1504–6
- [32] Jewell M C *et al* 2010 World-wide benchmarking of ITER Nb₃Sn strand test facilities *IEEE Trans. Appl. Supercond.* **20** 1500–3
- [33] Kikuchi K *et al* 1997 Development and manufacturing of bronze-processed Ta-added Nb₃Sn wires for the ITER *J. Cryog. Soc. Japan* **32** 167–72 (in Japanese)
- [34] Miyazaki T *et al* 2004 Development of Nb₃Sn superconducting wires for high-field magnets *J. Cryog. Soc. Japan* **39** 415–21 (in Japanese)
- [35] Nabara Y *et al* 2010 Procurement of Nb₃Sn superconducting conductors in ITER *J. Plasma Fusion Res. SERIES* **9** 270–5
- [36] Kanithi H *et al* 2012 Results of ITER-TF stand production at Luvata 2012 *Proc. ICEC 24-ICMC 2012* ed K Funaki, A Nishimura, Y Kamioka, T Haruyama and H Kumakura pp 791–4
- [37] Parrell J A *et al* 2009 Internal tin Nb₃Sn conductors engineered for fusion and particle accelerator applications *IEEE Trans. Appl. Supercond.* **19** 2573–9
- [38] Field M B *et al* 2014 Optimizing Nb₃Sn conductors for high field applications *IEEE Trans. Appl. Supercond.* **24** 6001105
- [39] Sytnikov V *et al* 1997 Development and manufacturing of superconducting cable-in-conduit conductors for ITER *IEEE Trans. Appl. Supercond.* **7** 1364–7
- [40] Hamada K *et al* 2011 First qualification of ITER toroidal field coil conductor jacketing *Fusion Eng. Des.* **86** 1506–10
- [41] della Corte A *et al* 2013 ITER and JT-60SA conductor production at ICAS *IEEE Trans. Appl. Supercond.* **23** 4200904
- [42] Dixon I R *et al* 2012 Nb₃Sn CICC fabrication for the SCH magnets *IEEE Trans. Appl. Supercond.* **22** 4301004
- [43] Pong I *et al* 2012 Worldwide benchmarking of ITER internal tin Nb₃Sn and Nb–Ti strands test facilities *IEEE Trans. Appl. Supercond.* **22** 4802606
- [44] Bottura L and Bordini B 2009 $J_C(B, T, \varepsilon)$ parameterization for the ITER Nb₃Sn production *IEEE Trans. Appl. Supercond.* **19** 1521–4
- [45] Bordini B *et al* 2011 Magnetization and inter-filament contact in HEP and ITER bronze-route Nb₃Sn wires *IEEE Trans. Appl. Supercond.* **21** 3373–6
- [46] Seo K *et al* 2010 Implementation of the ITER conductor database *IEEE Trans. Appl. Supercond.* **20** 499–502
- [47] Bruzzone P *et al* 2002 Upgrade of operating range for SULTAN test facility *IEEE Trans. Appl. Supercond.* **12** 520–3
- [48] Bruzzone P *et al* 2014 Commissioning of the main coil of the EDIPO test facility *IEEE Appl. Supercond.* **24** 9500205
- [49] Painter T 2012 private communication
- [50] Takahashi Y *et al* 2013 Cable twist pitch variation in Nb₃Sn conductors for ITER toroidal field coils in Japan *IEEE Trans. Appl. Supercond.* **23** 4801504
- [51] Bruzzone P *et al* 2010 Results of thermal strain and conductor elongation upon heat treatment for Nb₃Sn cable-in-conduit conductors *IEEE Trans. Appl. Supercond.* **20** 470–3
- [52] Mitchell N 2005 Finite element simulations of elasto-plastic processes in Nb₃Sn strands *Cryogenics* **45** 501–15
- [53] van Lanen E P A and Nijhuis A 2009 JackPot: a novel model to study the influence of current non-uniformity and cabling patterns in cable-in-conduit conductors *Cryogenics* **50** 139–48
- [54] Breschi M *et al* 2012 Results of the TF conductor performance qualification samples for the ITER project *Supercond. Sci. Technol.* **25** 095004
- [55] Marsh S A *et al* 2013 Results of the TFEU6 sample tested in SULTAN conductors *IEEE Trans. Appl. Supercond.* **23** 4200204
- [56] Bellina F *et al* 2010 Analysis of the ITER Nb₃Sn SULTAN sample test conditions with different joint technologies *IEEE Trans. Appl. Supercond.* **20** 482–6
- [57] van Lanen E P A and Nijhuis A 2011 Numerical analysis of the DC performance of ITER TF samples with different cabling pattern based on resistance measurements on terminations *Supercond. Sci. Technol.* **24** 085010
- [58] Gung C-Y *et al* 2009 Fabrication of the first US ITER TF conductor sample for qualification in SULTAN facility *IEEE Trans. Appl. Supercond.* **19** 1474–7
- [59] Breschi M *et al* 2009 Electromagnetic analysis of the voltage–temperature characteristics of the ITER TF conductor samples *IEEE Trans. Appl. Supercond.* **19** 1512–5
- [60] Ciazynski D 2007 Review of Nb₃Sn conductors for ITER *Fusion Eng. Des.* **82** 488–97

- [61] Bruzzone P *et al* 2012 Test results of ITER conductors in the SULTAN facility *Proc. 24th IAEA Fusion Energy Conf. IAEA CN-197*: p 536
- [62] Stepanov B *et al* 2013 SULTAN test facility: summary of recent results *Fusion Eng. Des.* **88** 282–5
- [63] Oh D K *et al* 2010 Performance test of TFKO2 qualification sample of ITER TF conductor *IEEE Trans. Appl. Supercond.* **20** 458–61
- [64] Kwon S P *et al* 2013 Preliminary performance test results of first CICC from Korea destined for an ITER TF magnet *IEEE Trans. Appl. Supercond.* **23** 4201705
- [65] Tronza V I *et al* 2013 Testing of RF 100 m TF qualification conductor in the SULTAN test facility *IEEE Trans. Appl. Supercond.* **23** 9500805
- [66] Tronza V I *et al* 2014 Test results of RF ITER TF conductors in the SULTAN test facility *IEEE Trans. Appl. Supercond.* **24** 4801905
- [67] Nunoya Y *et al* 2011 Test result of a full-size conductor developed for the ITER TF coils *IEEE Trans. Appl. Supercond.* **21** 1982–6
- [68] Nabara Y *et al* 2012 Examination of mass-produced Nb₃Sn conductors for ITER toroidal field coils in Japan *IEEE Trans. Appl. Supercond.* **22** 4804804
- [69] Bruzzone P *et al* 1996 Benchmark testing of Nb₃Sn strands for the ITER model coil *Adv. Cryog. Eng. (Mat)* **42B** 1351
- [70] Nijhuis A *et al* 2013 The effect of axial and transverse loading on the transport properties of ITER Nb₃Sn strands *Supercond. Sci. Technol.* **26** 084004
- [71] Devred A *et al* 2012 Strain redistribution effects on current-sharing measurements on straight samples of large Nb₃Sn cable in conduit conductors *Supercond. Sci. Technol.* **25** 054009
- [72] Kajitani *et al* 2013 Analytical study of degradation of CIC conductor performance due to strand bending and buckling *IEEE Trans. Appl. Supercond.* **23** 6001505
- [73] Tsuji *et al* 2001 ITER R&D: magnets: central solenoid model coil *Fusion Eng. Des.* **55** 153–70
- [74] Khodak A *et al* 2013 Optimization of ITER central solenoid insert design *Fusion Eng. Des.* **88** 1523–7
- [75] Martovetsky N *et al* 2002 Test of the ITER central solenoid model coil and CS insert *IEEE Trans. Appl. Supercond.* **12** 600–5
- [76] Mitchell N 2007 Assessment of conductor degradation in the ITER CS insert coil and implications for the ITER conductors *Supercond. Sci. Technol.* **20** 25–34
- [77] Miyatake T *et al* 2012 Influence of wire parameters on critical current versus strain characteristics of bronze processed Nb₃Sn superconducting wires *IEEE Trans. Appl. Supercond.* **22** 4805005
- [78] Hemmi T *et al* 2012 Test results and investigation of T_{CS} degradation in Japanese ITER CS conductor samples *IEEE Trans. Appl. Supercond.* **22** 4803305
- [79] Ulbricht A *et al* 2005 The ITER toroidal field model coil project *Fusion Eng. Des.* **73** 189
- [80] Zanino R *et al* 2009 EU contribution to the test and analysis of the ITER poloidal field conductor insert and the central solenoid model coil *Supercond. Sci. Technol.* **22** 085006
- [81] Vostner A *et al* 2005 The FBI facility—a test rig for critical current measurements on CICC as a function of strain *IEEE Trans. Appl. Supercond.* **15** 1387–90
- [82] Weiss K P *et al* 2007 Systematic approach to examine the strain effect on the critical current of Nb₃Sn cable-in-conduit-conductors *IEEE Trans. Appl. Supercond.* **17** 1469–72
- [83] Vostner A *et al* 2008 Development of the EFDA dipole high field conductor *IEEE Trans. Appl. Supercond.* **18** 544–7
- [84] Bruzzone P *et al* 2009 Test results of a Nb₃Sn cable-in-conduit conductor with variable pitch sequence *IEEE Trans. Appl. Supercond.* **19** 1448–51
- [85] Bruzzone P *et al* 1996 Conductor fabrication for the ITER model coils *IEEE Trans. Magn.* **32** 2300–3
- [86] Mitchell N *et al* 1998 Conductor development for the ITER magnets *Proc. 15th Int. Conf. on Magnet Technology* ed L Liangzhen, S Guoliao and Y Luguang (Beijing: Science Press) pp 347–52
- [87] Bessette D *et al* 1993 Fabrication and test results of the 40 kA CEA conductor for NET/ITER *Proc. 17th Symp. on Fusion Technology* ed C Ferro, M Gasparotto and H Knoepfel (Amsterdam: North-Holland) pp 788–92
- [88] Bessette D 2014 Design of a Nb₃Sn cable-in-conduit conductor to withstand the 60 000 electromagnetic cycles of the ITER central solenoid *IEEE Trans. Appl. Supercond.* **24** 4200505
- [89] Nijhuis A *et al* 2012 Optimisation of ITER Nb₃Sn CICC for coupling loss, transverse electromagnetic load and axial thermal contraction *Supercond. Sci. Technol.* **25** 015007
- [90] Nabara Y *et al* 2014 Impact of cable twist pitch on T_{CS} degradation and AC loss in Nb₃Sn conductors for ITER central solenoids *IEEE Trans. Appl. Supercond.* **24** 4200705
- [91] Calzolaio C *et al* 2012 *In situ* measurements of cable in conduit conductors via an inductive method *IEEE Trans. Appl. Supercond.* **22** 9002604
- [92] Calzolaio C *et al* 2013 Monitoring of the thermal strain distribution in CICC during the cyclic loading tests in SULTAN method *IEEE Trans. Appl. Supercond.* **23** 4200404
- [93] Hemmi T *et al* 2013 Neutron diffraction measurement of internal strain in the first Japanese ITER CS conductor sample *Supercond. Sci. Technol.* **26** 084002
- [94] Calzolaio C and Bruzzone P 2014 Analysis of the CICC performance through the measurement of the thermal strain distribution of the Nb₃Sn filaments in the cable cross section *IEEE Trans. Appl. Supercond.* **24** 4802204
- [95] Boso D P 2005 Multiscale analysis of the influence of the triplet helicoidal geometry on the strain state of a Nb₃Sn based strand for ITER coils *Cryogenics* **45** 589–605
- [96] Mitchell N 2008 Comparison between predictions and measurements of the superconducting performance of Nb₃Sn cable in conduit conductors with transverse load degradation *Supercond. Sci. Technol.* **21** 054005
- [97] Nijhuis A 2008 A solution for transverse load degradation in ITER Nb₃Sn CICC: verification of cabling effect on Lorentz force response *Supercond. Sci. Technol.* **21** 054005
- [98] Zhai Y and Bird M D 2008 Florida electro-mechanical cable model of Nb₃Sn CICC for high-field magnet design *Supercond. Sci. Technol.* **21** 115010
- [99] Nemov A S *et al* 2010 Generalized stiffness coefficients for ITER superconducting cables, direct FE modeling and initial configuration *Cryogenics* **50** 304–13
- [100] Bajas H *et al* 2010 Numerical simulation of the mechanical behaviour of ITER cable-in-conduit conductors *IEEE Trans. Appl. Supercond.* **20** 1467–70

- [101] Bajas H *et al* 2012 A. Approach to heterogeneous strain distribution in cable-in-conduit conductors through finite element simulation *IEEE Trans. Appl. Supercond.* **22** 4803104
- [102] Bajas H *et al* 2012 Finite element modeling of cable in conduit conductors *Supercond. Sci. Technol.* **25** 054019
- [103] Jewell M *et al* 2003 The influence of Nb₃Sn strand geometry on filament breakage under bend strain as revealed by metallography *Supercond. Sci. Technol.* **16** 1005–11
- [104] Sheth M K *et al* 2012 Procedures for evaluating filament cracking during fatigue testing of Nb₃Sn strands *AIP Conf. Proc.* **1435** 201
- [105] Sanabria C *et al* 2012 Evidence that filament fracture occurs in an ITER toroidal field conductor after cyclic Lorentz force loading in SULTAN *Supercond. Sci. Technol.* **25** 075007
- [106] Mitchell N *et al* 2013 Reversible and irreversible mechanical effects in real cable-in-conduit conductors *Supercond. Sci. Technol.* **26** 114004
- [107] Takahashi Y *et al* 2014 Cabling technology of Nb₃Sn conductor for ITER central solenoid *IEEE Trans. Appl. Supercond.* **24** 4802404
- [108] Farinon S *et al* 2008 Nb₃Sn wire layout optimization to reduce cabling degradation *IEEE Trans. Appl. Supercond.* **18** 984–8
- [109] Bottura L and Devred A 2013 Cable design optimization for LTS applications, private communication
- [110] Sumption M D and Collings E W 1995 Chromium diffusion into plated Nb₃Sn strands deduced from electrical resistivity measurement *IEEE Trans. Appl. Supercond.* **5** 1925–8
- [111] Fetisov S S *et al* 2013 Residual resistance ratio in Nb₃Sn strands during ITER TF conductor manufacture and after SULTAN tests *IEEE Trans. Appl. Supercond.* **99** 1
- [112] Horsthemke H 2008 Chromium deposition by trivalent and hexavalent processes for functional and decorative applications, private communication
- [113] DeLong W T 1960 A modified phase diagram for stainless steel weld metals *Met. Prog.* **77** 98
- [114] Vostner A *et al* 2013 Benchmarking of mechanical test facilities related to ITER CICC steel jackets *IEEE Trans. Appl. Supercond.* **23** 9500705
- [115] Weiss K P *et al* 2010 Tensile test results on compacted and annealed 316LN material *AIP Conf. Proc.* **1219** 3–8
- [116] Hamada K *et al* 2008 Development of jacketing technologies for ITER CS and TF conductor *AIP Conf. Proc.* **986** 76
- [117] Hamada K *et al* 2012 Effect of specimen shape on the elongation of 316LN jacket used in the ITER toroidal field coil *Adv. Cryog. Eng. AIP Conf. Proc.* **1435** 55–62
- [118] Park S H *et al* 2012 The effect of plastic deformation on low temperature mechanical and magnetic properties of Austenite 316LN tube for ITER TF conductor *IEEE Trans. Appl. Supercond.* **22** 7800204
- [119] Qin J *et al* 2012 Mechanical test on the ITER TF jacket *Cryogenics* **52** 336–9
- [120] Anashkin O P *et al* 2012 Tensile tests of ITER TF conductors jacket materials *AIP Conf. Proc.* **1435** 117
- [121] Nakajima H *et al* 2004 Development of low Carbon and Boron added 22Mn–13Cr–9Ni–1Mo–0.24N steel (JK2LB) for jacket which undergoes Nb₃Sn heat treatment *IEEE Trans. Appl. Supercond.* **14** 1145–8
- [122] Hamada K *et al* 2007 Optimization of JK2LB chemical composition for ITER central solenoid conduit material *Cryogenics* **47** 174–82
- [123] Arnaud J P and Eveilleau M 2011 M Nitronic 50 Base Material Heat # A11371 Thermal Expansion CERN *NOTE SBT/CT/11-68*
- [124] Libeyre P *et al* 2012 Addressing the technical challenges for the construction of the ITER central solenoid *IEEE Trans. Appl. Supercond.* **22** 4201104
- [125] Libeyre P *et al* 2011 Conductor jacket development to meet the mechanical requirements of the ITER central solenoid coils *Fusion Eng. Des.* **86** 1553–7
- [126] Sgobba S *et al* 2012 Progress in production and qualification of stainless steel jacket material for the conductor of the ITER central solenoid *IEEE Trans. Appl. Supercond.* **22** 7800104
- [127] Nyilas A *et al* 2012 Fatigue crack growth rate and fracture toughness of ITER central solenoid jacket materials at 7 K *AIP Conf. Proc.* **1435** 47
- [128] Hamada K *et al* 2012 Preparation for the ITER central solenoid conductor manufacturing *IEEE Trans. Appl. Supercond.* **22** 4203404
- [129] Sgobba S *et al* 2013 A comparative assessment of metallurgical and mechanical properties of two austenitic stainless steels for the conductor jacket of the ITER central solenoid *Fusion Eng. Des.* **88** 2484–7
- [130] Tsuchiya Y *et al* 1998 Residual stress for a jacket material for ITER superconducting coils *Physica B* **241–243** 1264–6
- [131] Wong F M G *et al* 1997 Residual stresses in superconducting jackets after compaction *Proc. 16th Int. Cryo. Eng. Conf. and Int. Cryo. Mat. Conf.* **3** 1903
- [132] Walker K 1970 The effect of stress ratio during crack propagation and fatigue for 2024-T3 7005-T6 Aluminum ASTM STP 462 1–14
- [133] Jong C, Freudenberg K, Myatt L and Cochran K 2013 Maximum allowable defect size for CS conduit unit length (7m) and butt-welds, private communication
- [134] Ozeki H *et al* 2014 Establishment of production process of JK2LB jacket section for ITER CS tests *IEEE Trans. Applied Supercond.* **24** 4800604
- [135] Bauser M, Sauer G and Siegert K (ed) 2006 *Extrusion* 2nd edn (Materials Park: ASM International)
- [136] Sgobba S 2013 personal communication
- [137] Stepanov B *et al* 2012 Test results of three poloidal field superconducting samples in SULTAN *IEEE Trans. Appl. Supercond.* **22** 4803504
- [138] Pong I *et al* 2012 Current sharing temperature of NbTi SULTAN samples compared to prediction using a single pinning mechanism parameterization for NbTi strand *Supercond. Sci. Technol.* **25** 054011
- [139] Reccia L *et al* 2011 Preparation of PF1/6 and PF2 conductor performance qualification sample *IEEE Trans. Appl. Supercond.* **21** 1930–3
- [140] Bruzzone P *et al* 2005 Test results of the ITER PF insert conductor short sample in SULTAN *IEEE Trans. Appl. Supercond.* **15** 1351–4
- [141] Liu H J *et al* 2011 Mechanical tests on the ITER PF 316L jacket after compaction *Cryogenics* **51** 234–6
- [142] Qin J *et al* 2012 Fatigue tests on the ITER PF jacket *Cryogenics* **52** 486–90